THE KINEMATICS OF THE UPPER EXTREMITY AND SUBSEQUENT EFFECTS ON JOINT LOADING AND SURGICAL TREATMENT

A Dissertation

Presented to the Faculty of the Graduate School

of Cornell University

In Partial Fulfillment of the Requirements for the Degree of

Doctor of Philosophy

by

Garry T. Hayeck

August 2009

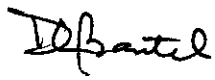

THE KINEMATICS OF THE UPPER EXTREMITY AND SUBSEQUENT EFFECTS ON JOINT LOADING AND SURGICAL TREATMENT

Garry T. Hayeck, Ph. D.

Cornell University 2009

The kinematic variability of the upper extremity presents challenges when developing or analyzing surgical treatments of the shoulder and elbow. The wide range of possible activities places diverse loading conditions on these joints. To improve surgical outcomes at these joints the relationships between joint loading and kinematics must be established. In the shoulder, an optimally-based *in vitro* simulator of glenohumeral motion was developed. It was validated using simple humeral abduction activities and a mechanical surrogate shoulder. Our approach demonstrated the viability of our technique and showed how the use of the simulator could be expanded to cadaveric shoulders. In the elbow, computational models were coupled with motion analysis studies to determine the response of a contemporary total elbow replacement to loading induced by typical activities of daily living. Activities of daily living were determined from normal subjects and total elbow replacement patients. Differences between the kinematics and loading of the groups were statistically significant, although numerically small. A biomechanical model demonstrated that the contact force at the replaced elbow joint increased significantly as the humeral component of the elbow was internally rotated. It showed that these increased forces would occur in locations likely to cause additional further internal rotation of the component. Structural finite element analyses of both the humeral and ulnar bone-implant systems illustrated the sensitivity of load transfer and cement stresses to the

interface conditions between the implant and the cement layer. As implant-cement bonding decreased, load transfer away from the joint increased in both the humerus and ulna. The mode of humeral load transfer was dependent upon the extent of contact between the implant and the distal humeral bone. Relaxing the bonding between the implant and the cement was shown to have a greater detrimental effect on the ulnar cement stresses than those of the humerus. These analyses all serve to illustrate the complex interplay between joint motion and kinetic and structural response that must be considered when investigating the behavior of the upper extremity.

BIOGRAPHICAL SKETCH

Garry Thomas Hayeck was born in Lancaster, Pennsylvania on May 20, 1975. Spending his formative years in Pennsylvania and New Hampshire, he then enrolled in Cornell University in the autumn of 1993. In May of 1999, he left Cornell with both a Bachelors of Science and a Masters of Engineering in Mechanical Engineering under his arm and his beloved, Kari, by his side. At this point already fascinated by orthopaedics, he sought employment at Synthes, U.S.A developing fracture fixation implants and instruments. In 2001, he and Kari were wed and began their lives together in earnest. Two years later, the opportunity to refine and expand his orthopaedic knowledge arose and Garry returned to Cornell to pursue his doctorate in Biomedical Engineering. In 2004, Kari also returned to Cornell to seek her doctorate in veterinary medicine. Not being sufficiently challenged by this situation, in 2006 Garry and Kari decided to have children. From one came two, and in January 2007, Gillian Taylor and Mackenzie Jean were born. This work is the culmination of Garry's doctoral research and allows him to exit Cornell, as before, alongside Kari. This time, however, they exit with minds, arms, and hearts substantially more full than when they came.

To my parents,

without whom I never

would have started

and to

Kari, Gillie, and Kenzie

without whom I never

could have finished.

ACKNOWLEDGMENTS

This work would not have been possible without the contributions of many individuals. My advisor, Professor Don Bartel, has provided endless insight and support that has helped to shape not only this dissertation but also my thinking both as a person and researcher. It is an honor to be among the graduate students with which he has shared his knowledge and it is a special honor to be the last. If the number of potential graduate students inquiring about openings in his lab is an indication, as an advisor he will surely be missed. My remaining committee members, Professor Larry Bonassar and Dr. Cornelia Farnum, have also been invaluable to this work. They have examined it from angles I would not have considered and in doing so have made it stronger as a whole. I am also thankful for the opportunities and guidance offered by Dr. Tim Wright at the Hospital for Special Surgery and the clinical insights of Dr. Mark Figgie and Dr. Robert Hotchkiss.

In addition, I would like to thank all those who aided this work in such a material fashion. The cadaveric shoulder simulator would not have been completed without the efforts of both Dr. William Robertson and Daniel Choi. Kirk Gunsallus developed the ulnar finite element model and, along with Jason Long, has helped to refine much of the thinking that comprises this dissertation. I thank them both tremendously. I would also like to thank all of the other members, both past and present, of the Cornell Biomechanics Group. They have provided insight and friendship and have made these years as enjoyable as they were educational. Finally, I would like to thank my family. Nothing would be possible without them.

This work was supported through funds provided by the National Institutes of Health, the Clark and Kirby Foundations, and Zimmer, Inc. for projects of mutual interest.

TABLE OF CONTENTS

LIST OF FIGURES

LIST OF TABLES

Chapter 1

Introduction

1.1 Overview of the Human Upper Extremity

While the lower extremity of a human being remains bound to repetitive tasks such as gait, stair-climb, and running, the development of bipedal gait has freed the upper extremity from the necessity to specialize towards these pure locomotion activities. Thus, the upper extremity is used to perform a wide variety of tasks that may be geared to diverse objectives. Where the legs may walk, run, or climb, the arms may wave, pitch, or push. The greater variability in the functions that the upper extremity is asked to perform is reflected in the anatomy of the limb. Homologues between the joints of the upper and lower extremity exist, but in each case the constraints at each joint present in the anatomy of the lower extremity are relaxed in the upper extremity allowing for increased range of motion at each of the joints. Thus the upper extremity is generalized rather than specialized and is able to perform diverse motions which may be functionally unrelated.

Each of these diverse motions engenders a unique biomechanical environment around the joints of the upper limb. The more diverse the motions, the more varied the accompanying loads and moments that are transmitted across the joints will be. The varied loading that can occur at each joint creates challenges when designing surgical techniques or joint replacement devices to repair or replace injured or degenerated structures in a joint of the upper extremity. To address these challenges, one must have sufficient knowledge of how changes in joint loading are related to changes in joint kinematics for motions of the upper extremity. It is also necessary to understand how the replaced or repaired joint relates to the natural anatomy.

With this in mind, the studies here consider two joints of the upper extremity, the shoulder and the elbow. In our studies of the shoulder, our goal is create a system that will allow exploration of the relationship between motion and joint forces over a wide range of humeral positions. Using this system we may then evaluate the effects of surgical treatments, including rotator cuff repair and joint arthroplasty, on these motion-joint force relationships. In the elbow we investigate the relationship between motion and joint force for a specified set of upper extremity activities of daily living. We then use this information to study to the structural response of an implanted total elbow replacement/bone/cement system. For both of these tasks, it is helpful to understand the shoulder and elbow joint in both their natural and their surgically repaired conditions.

1.2 The Shoulder

1.2.1 The Natural Joint

The shoulder joint of the upper extremity is homologous to the hip of the lower extremity. However, the conformity of the acetabular cup of the pelvis and the head

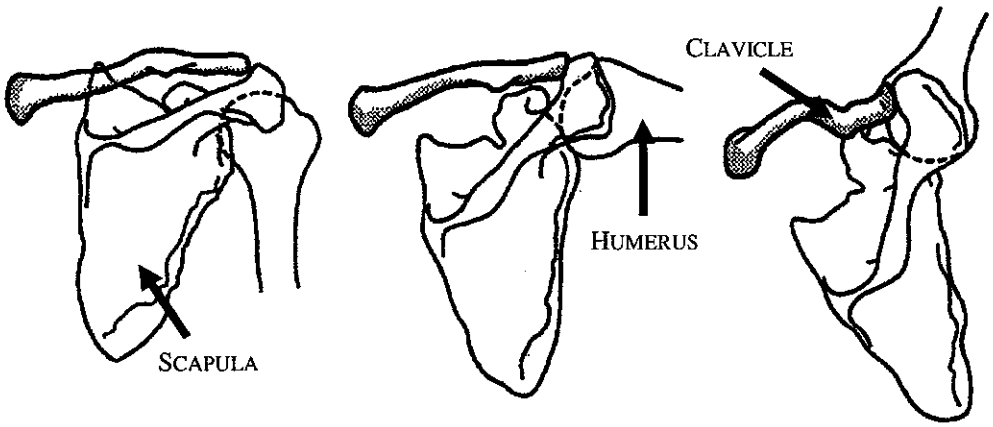

Figure 1.1: Anatomy of the three bones of the shoulder joint (scapula, humerus, and clavicle) during abduction of the humerus. Adapted from ([72])

of the femur largely limits the motion at the hip to rotation of the femur with respect to the pelvis. In other words, the anatomy of the hip is that of a constrained ball-and-socket joint. Anatomically, the glenoid of the scapula and the humeral head lack this degree of conformity (Figure 1.1). Because of the limited extent of the articular surface of the glenoid with respect to that of the humeral head, the glenohumeral joint might be better visualized as a ball moving across a plate than a ball in a socket. In reality however, the cavity of the glenoid is ellipsoidal with a smaller, more conforming radius in the superior-inferior direction than in the anterior-posterior direction [54]. Thus, unlike at the hip, the humeral head is able to translate with respect to the scapula as well as rotate. Because of the decreased conformity, anterior-posterior translation is less constrained by the existing bony geometry than is superior-inferior translation. To limit the humeral translations allowed by the bony anatomy and maintain stability of the shoulder joint, substantial soft-tissue support in required.

Since the surrounding soft-tissue structures of the shoulder are critical to the stability of the shoulder joint, disruption of or injury to these structures can cause substantial decreases in joint constraint, appreciable changes in the kinematics of standard tasks,

and variations in the relationships between motion and joint loading that are present in the uninjured joint [70]. These changes can then lead to acceleration of joint degeneration, loss of function, and an increase in joint pain [61].

For isolated injuries to the rotator cuff that do not respond to conservative, nonsurgical intervention, surgical repair of the injured tissue is the standard course of treatment [78]. For massive irreparable rotator cuff tears, standard treatment involves either joint debridement or tendon transfer. For conditions associated with degeneration of the articular surface of the joint due to arthritis, some form of joint arthroplasty is generally performed. Each of these treatments involves altering the biomechanical environment of the shoulder.

1.2.2 The Treated Shoulder

Rotator Cuff Repair

Repair of the rotator cuff may be performed in an arthroscopic, minimally-invasive, or fully open manner depending upon the nature of the damage to the cuff and the proposed surgical treatment. Partial thickness tears of the rotator cuff are generally repaired arthroscopically and may include debridement of the joint and subacromial decompression, in which the undersurface of the acromion is removed to reduce the risk of acromial impingement with the tendons of the cuff. In cases where decompression has failed, acromioplasty of the anterior portion of the acromion may be performed to remove any possibility of impingement.

Full thickness tears of the rotator cuff are tears whose extent passes entirely through the injured tissue. These tears may either be small holes through the injured cuff or complete bisections of the tendon or muscle. Avulsions of tendon from the periosteal

surface of the humeral head are also considered to be full thickness tears. Full thickness rotator cuff repairs are accomplished by surgically reattaching the disjoint ends of the injured tendons. In the case of avulsions, the tendon is sutured or anchored directly to the bone. A variety of suturing techniques for these procedures have been developed in an attempt in increase the strength of the tendon interface and facilitate tendon healing.

Massive rotator cuff tears that are accompanied by shoulder weakness generally require tendon transfers in order to achieve satisfactory outcomes. In most of these cases where certain muscles of the cuff are beyond surgical repair, the tendons of other muscles are rerouted to replicate the function of the injured tissues. Most commonly, it is the external rotators of the shoulder, the infraspinatus or the teres minor, that are deficient and the latissimus dorsi is usually rerouted to restore the lost function.

Each type of rotator cuff repair alters the biomechanics of the natural shoulder joint. In the case of partial-thickness tears, the debridement process may decrease the cross-sectional areas of muscle or tendon and may effectively limit the amount of force that can be transmitted across these structures. Subsequent acromioplasty will change the bony constraint around the humeral head, thereby changing joint kinematics. Full thickness repairs weaken the existing soft-tissue structures from their natural uninjured state. Different suturing techniques resist muscle tension and change tissue elongation differently. Massive cuff tears involving tendon transfer completely change joint biomechanics and their effect depends on the location of insertion chosen for the newly-routed muscle.

Shoulder Arthroplasty

Standard total shoulder replacements involve two primary components (Figure 1.2). The humeral component consists of a rounded metal articular surface connected to a metal stem. The corresponding glenoid component is typically an ultra-high molecular weight polyethylene (UHWMPE). Many variations exist within common glenoid component designs. Some designs incorporate a concave articular surface that is completely conforming to the radius of the humeral component. Other designs utilize nonconforming concave radii that attempt to more closely mimic the natural glenoid articular surface geometry. Different strategies also exist to fix the glenoid component within the trabecular bone of the glenoid cavity. Some designs incorporate a series of pegs for interlock of the components while other designs are keeled. Glenoid components also may be with or without metal backing.

For cases involving massive tears of the rotator cuff with associated arthritis, reverse total shoulder replacements have been developed. In these implants, the humeral

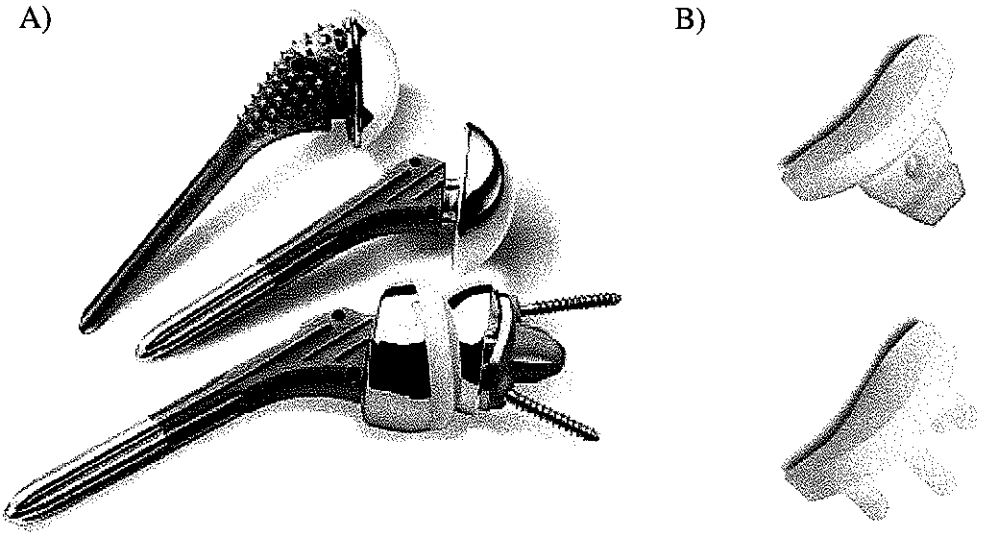

Figure 1.2: A) Fracture, standard, and reverse types (top to bottom) of shoulder replacements and B) keeled and pegged (top to bottom) standard glenoid components. Adapted from ([11])

component consists of an UHMWPE lined cup attached to a medullary stem. The glenoid component of these implants is a metal hemisphere. Thus, the articular surface geometry of the standard implant, and of the natural shoulder, has been reversed. The intent of these implants is for the humeral cup to provide some of the stability lost with the massive cuff tear. The lateral offset of the sphere of the glenoid component from the articular surface of the natural glenoid may be altered in these implants to increase the mechanical advantage of the remaining muscles of the shoulder, especially the deltoid [9].

1.2.3 Complications of Shoulder Treatment

Rotator Cuff Repair

The most common complication of rotator cuff surgery is the failure of the repaired tendon to heal and subsequent re-tearing of the cuff [53]. This occurs in approximately 6.2% of patients who have undergone surgical rotator cuff repair. Failure of the cuff to heal may be do to a variety of reasons. However, assuming that the viability of the tissue has been established at the time of surgery, it is likely that failure occurs in this manner because of insufficient strength of the suture-tendon or suture-bone interface. This might be remedied either through altered surgical techniques or altered rehabilitation protocols that allow tissue healing to occur before large forces are transmitted across these interfaces.

Shoulder Arthroplasty

Common complications for shoulder arthroplasty include the loosening of the glenoid component, loosening of the humeral component, instability of the shoulder, and associated rotator cuff tearing. Component loosening is partially attributable to the loading at the joint as the patient performs typical activities of daily living.

1.3 The Elbow

1.3.1 The Natural Joint

The elbow is primarily a hinge joint consisting of three bones: the humerus, the ulna, and the radius. The flexion axis of the elbow passes through the center of the trochlear sulcus medially on the distal humerus and the center of the capitellum laterally on the distal humerus. Both the ulna and the radius articulate about the axis through these two points.

Because of the mobility of the shoulder, the elbow must also operate under a wide range of functional loads. The functional loads caused by normal upper extremity activities of daily living may cause large forces and moments to be transmitted across the elbow joint. In the natural elbow, these loads are transmitted from the radius and ulna of the forearm to the humerus of the upper arm at both the articulation of the greater sigmoid notch of the ulna and the trochlea of the humerus and at the articulation of the head of the radius and the capitellum of the humerus. These dual locations of load transfer provide both compressive and varus-valgus stability to the joint. The collateral ligaments of the elbow also serve to resist the applied moments about the joint.

1.3.2 The Replaced Elbow

There are two varieties of modern total elbow replacements. The first is referred to as a surface replacement of the elbow. In these implants the articular surfaces of the humerus and ulna (and occasionally the radius) are replaced with implant components that aim to mimic and provide similar degrees of constraint and stability to the natural joint (Figure 1.3). This approach requires the reconstruction and balancing of the collateral ligaments on the medial and lateral aspects of the elbow joint.

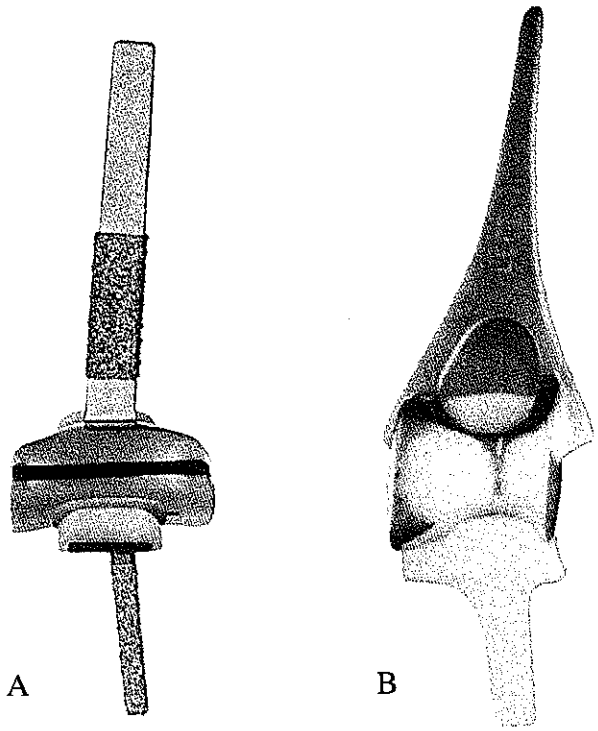

Figure 1.3: A) Kudo and B) Souter-Strathclyde (long-stemmed) surface replacements of the elbow. Adapted from ([49])

The second and more common form of the modern total elbow replacement is the semiconstrained implant. In this type of prosthesis, the ulnar component is prevented from disarticulating with the humeral component, generally through the use of a pin connecting the two. These devices are thought of as semiconstrained because the articulation between the humerus and ulna, while being prevented from disarticulation, is not a fixed hinge. In every semiconstrained implant design, there is considerable slop between the humeral and ulnar components of the implant, allowing limited translation and rotation in all directions. The most commonly used semiconstrained implant today is the Coonrad-Morrey [67] (Figure 1.4).

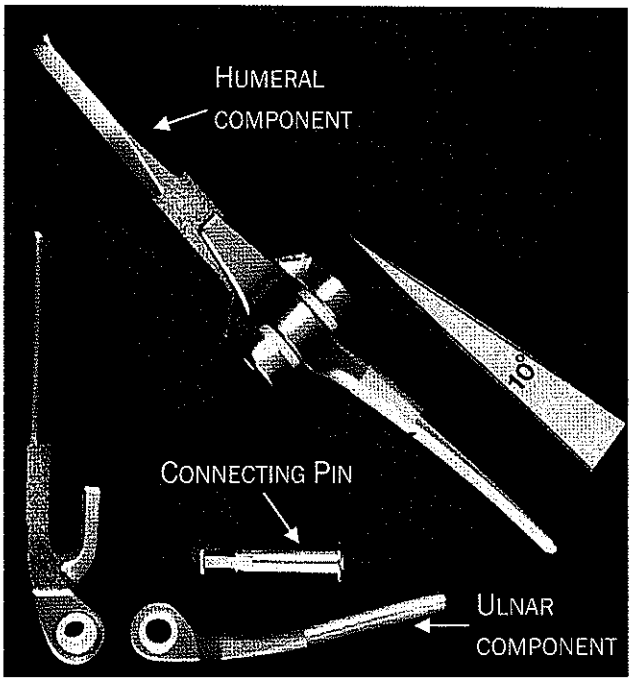

Figure 1.4: Coonrad-Morrey semiconstrained total elbow replacement, both assembled and disarticulated. There is approximately 10 degrees of varus-valgus laxity between the humeral and ulnar components. From ([58])

The semiconstrained implants considerably alter the natural biomechanical environment of the elbow. In many cases, the head of the radius is removed, eliminating the possibility of load sharing between the radius and the ulna at the elbow joint. The collateral ligaments of the elbow may also be removed. Thus all reaction forces and moments are transmitted across the elbow joint through the articulation of the humeral and ulnar components of these semiconstrained prostheses.

1.3.3 Complications of Elbow Replacement

Because of the large forces and moments across the elbow joint, one of the primary complications of semiconstrained total elbow replacement using the Coonrad-Morrey prosthesis is wear of the articular bushings. Upon retrieval, substantial wear of the bushing may be observed. Bushing wear may be so severe that the metal regions of the humeral and ulnar implant components begin to impinge and abrade [24].

Aseptic loosening of the Coonrad-Morrey is also a common complication. Some evidence implicates the presence of particulate wear debris in the surrounding bone as a reason for the loosening [24]. Cement breakdown due to mechanical stresses may also be a factor in this failure mechanism.

1.4 Research Objectives

Many of the complications of the previously described repair procedures of the shoulder and the elbow are the result of the forces and the moments transferred across each of the joints. The difficulty with the upper extremity is that these forces and moments vary considerably even among what could be considered to be typical motions for the limb. The unifying goal of this research is to increase our understanding both of the biomechanical environments under which the joints of the upper extremity operate during typical motions and of how surgical treatments may affect those environments. Surgically treated joints will experience altered kinematics and loading and it is uncertain how these states may affect the viability of the treatment performed.

Since the glenohumeral joint is the most unconstrained diarthrodal joint in the human body, the variability in the movements performed is substantial. Since there is no motion that can be said to be typical of the shoulder, if one wishes to determine the effect of surgical treatments on the kinematics and the loading at the glenohumeral joint, it is necessary to have the ability to evaluate these treatments over a wide range of activities and associated shoulder movements. The goal of Chapter 2 of this research is to develop an apparatus that makes this type of testing possible. Here we develop a cadaveric simulator of shoulder motion that allows determination of the

biomechanical environment around the glenohumeral joint as the humerus is moved through a prescribed activity. Furthermore, we improve upon the existing generation of simulators by automating the force application process and reducing the number of the assumptions made by the researcher when investigating these phenomena.

We then consider the biomechanical environment of the elbow. Given the commonality of bushing wear reported in the clinical follow-up studies of total elbow replacement, the magnitudes of the contact forces acting on the articular surfaces of the replaced elbow are of interest. Taking two sets of kinematic data that represent typical activities of daily living for a healthy subject from the literature, Chapter 3 examines the effect of altering the position of the implanted humeral component on the contact forces that are applied to the articular bushings of a contemporary semiconstrained total elbow replacement, the Coonrad-Morrey. We examine translational and rotational movements of the implant's axis of rotation with respect to the natural flexion axis of the elbow to determine the sensitivity of the contact forces across the implant to these surgical parameters.

While the use of kinematic data from healthy patients is useful to elucidate the changes in contact forces as humeral implant position is varied, these kinematics may not directly represent the kinematics of a total elbow patient. If the kinematics do not directly represent those of total elbow patients, then the force magnitudes may not be indicative of those found in total elbow patients either. Thus, Chapter 3 raises the question as to whether the kinematics of a healthy person performing a task are similar enough to the kinematics of a total elbow patient to use them as a surrogate for those of the total elbow patient and, by extension, whether the forces predicted using normal subject kinematics are similar to those predicted using the kinematics of total elbow

patients. In addition, we also wanted to determine whether the two activities we investigated in Chapter 3 adequately covered the space of possible activities that an individual might perform. Using motion analysis of both normal subjects and total elbow patients, Chapter 4 sought to answer these questions. Our objective in this study was both to determine whether the force and moment curves that arose on the elbow during a motion performed by a total elbow patient could be explained by the distributions of curves determined for normal subjects and to determine whether the coverage of the motions we were examining was appropriate.

By examining the forces on the elbow it is only possible to gain insight into whether wear of the articular contact surfaces may increase or decrease. However, wear is not the only phenomena that can promote loosening of a total elbow replacement. It is also necessary to examine the structural response of the bone-cement-implant system to the loads applied. Furthermore, while contact forces across the joint may be worsened by one particular implant position, the most detrimental structural response of the system may occur at other implant positions. Component fixation will also affect the structural response. The goal of Chapter 5 was to investigate the structural response of the humeral bone-cement-implant system to changes in implant fixation, humeral component position, and the structural stiffness of the surrounding bone tissue.

Chapter 6 extends the structural analyses performed in Chapter 5 in an attempt to identify likely areas of failure between the ulnar and humeral aspects of the total elbow replacement. Again we seek to determine the structural response of the bone-implant system to changes in humeral position, which may affect implant loading, component fixation, and the structural stiffness of the surrounding ulnar bone.

The final chapter is a synthesis of the results of the previous chapters; it summarizes the work performed, highlights the most important conclusions, and makes overall recommendations considering the entirety of the analyses. Future extensions of our research are also considered.

Chapter 2

Development of an Optimally-Driven Cadaveric Simulator of Glenohumeral Motion

2.1 Introduction

Injury to the glenohumeral joint may lead to loss of joint stability necessitating surgical repair of surrounding soft-tissue and may result in the development of osteoarthritis culminating in joint arthroplasty. In order to understand the mechanical processes leading to joint degradation, to improve the outcome of current surgical repair techniques, and to evaluate the efficacy of new surgical treatments for the shoulder, it is necessary to understand how the anatomical structures of the joint contribute to the biomechanical environment and how disruption of these structures may alter shoulder stability and the process of articular degeneration. In this regard, it is necessary to understand how loads are distributed in the surrounding soft tissue structures of the shoulder and how these force distributions influence the contact force at the articular surface of the glenohumeral joint.

Many attempts have been made to quantify both the kinematics of the shoulder and the contact force across the joint during normal motions. Some of these attempts have taken the form of computational studies, in which mathematical models of the shoulder mechanism are created and examined [28, 36, 45, 72, 73]. These studies use experimental data to inform their models and are able to determine the contact force across the glenohumeral joint. However, depending on the accuracy of the model, it is possible that a physical shoulder may not move in the manner predicted by the model and therefore may be subject to different forces when performing the motion prescribed. It is also difficult using these models to study other physical phenomena, such as injury to the natural articular surface or wear of the replaced articular surface, as this would require additional parameters be added to the computational models and would substantially increase model complexity.

In other studies, *in vitro* shoulder simulators have been created to investigate the relationship between kinematics and force [17, 30, 35, 38, 42, 62, 71]. In these *in vitro* simulators, the scapula of the shoulder is often affixed to a rigid frame and a series of actuators are attached to the tendons of the muscles of interest to apply muscle forces across the shoulder joint. In most cases, however, the number of muscles included in the simulator exceeds the number of degrees of freedom at the joint. Thus for any motion, there are multiple sets of muscle forces that could serve to move the humerus in the specified manner. Investigators have then been forced to make assumptions in order to reduce the total number of independent muscles and solve this muscle redundancy problem. These assumptions have been shown to have an effect on the resulting kinematics of the shoulder [37] and have included muscle forces being apportioned equally to the muscles [17], based upon physiological cross-sectional areas (PCSA) [30], or based upon electromyographic (EMG) recording [71].

It is unlikely that any of these methods fully capture the *in vivo* distribution of the forces across the shoulder.

The goal of this work was to create an *in vitro* shoulder simulator that minimizes the drawbacks of existing simulators by incorporating strengths of the computational modeling approach. Thus, rather than requiring substantial input from the investigator as to the nature and distribution of the forces throughout the shoulder, our simulator will use an internal computational model to determine the muscle and joint force distributions for a specified position of the humerus. Input parameters in the model may then be refined through further experimentation to better replicate force distributions seen *in vivo*. By coupling the computational model to the physical simulator, it will then also be possible to investigate other phenomena such as articular surface damage and wear.

2.2 Methods

2.2.1 Overview

To investigate the effect of muscle loading on glenohumeral motion a shoulder simulator was developed that incorporates four rotator cuff muscles and the three heads of the deltoid. The four rotator cuff muscles were the infraspinatus, the supraspinatus, the teres minor, and the subscapularis. The subscapularis was considered to be two muscles, the superior subscapularis and the inferior subscapularis, to approximate its broad, fanlike nature and correctly model its line of action. These muscles were chosen because they have been shown to be active during humeral abduction in the scapular plane [3], with the supraspinatus, and anterior and middle heads of the deltoid being primarily responsible for abduction and the remaining muscles contributing to joint stability. The simulator was designed to explore a

variety of shoulder motions; initial testing of the machine was performed using one of the most basic motions, humeral abduction.

2.2.2 Physical Simulator

The objective of the physical design of the simulator was to hold fixed the scapula of the shoulder while allowing forces to be applied to identified muscle insertion points on the humerus. Since we were primarily interested in the force distributions around the glenohumeral joint, scapulothoracic motion was not included in our simulator. Furthermore, we desired to be able to vary the effective origins of the muscles being studied based upon specimen specific geometry and possible surgical alterations. The primary physical components of the cadaveric simulator are: a rigid mounting plate onto which the scapula is attached, three vertically-adjustable deltoid pulleys to serve as the effective origins for the anterior, middle, and posterior heads of the deltoid, an overhead positioning plate to control the horizontal position of the deltoid pulleys, a vertical positioning plate to serve as the effective origin of the remaining rotator cuff muscles, a bank of eight Industrial Devices Corporation electric cylinders and microstepping drives that apply force to the simulated muscles, nylon coated braided steel cable to transmit force from the electric cylinders to the effective muscle insertions, and a rigid frame on which the remaining components are mounted (Figure 2.1). To measure the force in each muscle, 100 lbs load cells were placed inline with each of the braided steel cables. Delrin bushings were inserted into the hole of the vertical positioning plate to minimize friction with the nylon coated cables. Microstepping drives are controlled and humeral positions and muscle forces are monitored using a custom-developed control system.

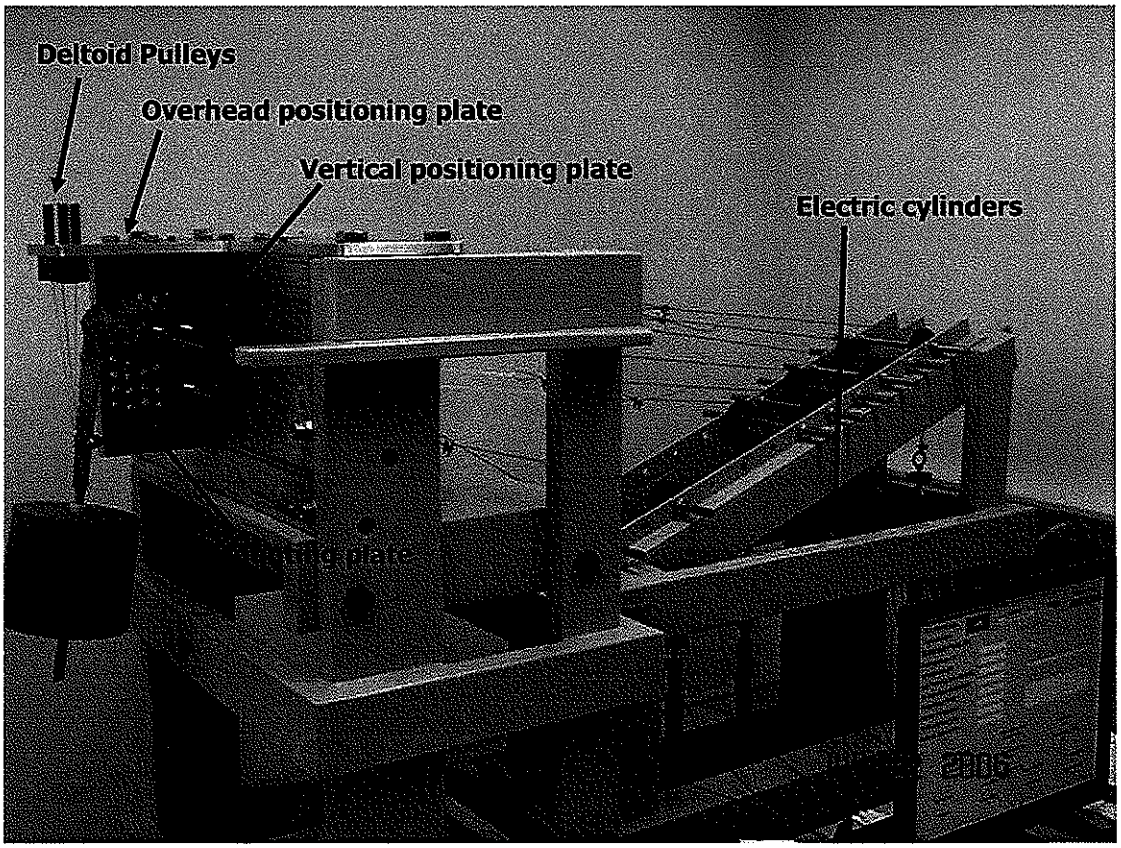

Figure 2.1: Configuration of shoulder simulator apparatus with mounted cadaveric shoulder and attached 3.5 kg weight

2.2.3 Simulator Control

The control system for the simulator has two primary functions. The first is to monitor the position and orientation of the humerus throughout the experiment. The second is to drive the humeral position as specified during the experiment by using a set of calculated optimal muscle forces.

Humeral positions and orientations are tracked using custom software developed for the Praxim surgical navigation system (Praxim, Grenoble, France). Optical tracking is accomplished through the placement of a reflective marker triad on the humerus and an additional triad fixed to the shoulder simulator frame. Calibration of the optical tracking system is performed according the manufacturer's instructions. Humeral and

scapular coordinate systems are constructed by digitizing three points on the scapula as recommended by the International Society of Biomechanics (ISB) [81]. The center of humeral rotation is calculated by circumducting the humerus while applying compressive force to the glenohumeral joint and fitting a sphere to the resulting point cloud. Humeral neutral position and orientation are established visually. According to ISB recommendation, humeral plane of elevation, humeral elevation angle, and humeral axial rotation are tracked along with the anterior, superior, and lateral translations of the humeral center of rotation.

Using a pointer, muscle insertions on the humerus are digitized along with the effective origin of the muscle on either the vertical positioning plate or the deltoid pulleys (Table 2.1). Additional anatomical landmarks on the humerus and glenoid are also digitized using the pointer. This information is used to accomplish the second function of the control system, the application of forces necessary to drive the humerus to a specific position.

The second function of the control system is accomplished in two phases. The purpose of the first phase is to move the humerus to a specified position. In this phase, given a desired orientation and information about the current humeral orientation, the transformation matrix between the desired and current orientations is computed and converted to axis-angle format. Using information about each muscle's attachment points as well as the current location of the humeral head center, each muscle's unit moment vector about the head center is calculated. The linear combination of muscle moment unit vectors that has the minimum included angle with the rotation axis is determined using least-squares linear optimization. The coefficients of the resulting linear combination of vectors are the ratio of forces necessary to rotate the humerus

Table 2.1: Digitized Landmarks for the Simulator Control System

Purpose of Digitization	*Points Digitized*	*Frame of Reference*
Calculate the humeral circumduction sphere	Distal humeral shaft	Camera
Position the surface of the glenoid and glenoid ligament origins	Points on the glenoid surface: most superior point most inferior point most anterior point most posterior point	Scapula
Establish the scapular coordinate system	Points on the scapula: Angulus Acromialis Trigonum Spinae Scapula Angulus Inferior	Camera
Record the muscle origins	Teres Minor Infraspinatus Supraspinatus Superior Subscapularis Inferior Subscapularis Posterior Deltoid Middle Deltoid Anterior Deltoid	Scapula
Record the muscle insertions	Teres Minor Infraspinatus Supraspinatus Superior Subscapularis Inferior Subscapularis Posterior Deltoid Middle Deltoid Anterior Deltoid Glenoid –	Humerus
Establish the global laboratory coordinate system	Points on the overhead plate: Lateral posterior Lateral anterior Medial posterior	Camera

about the intended rotation axis. This ratio is then scaled based upon the angular difference between the current humeral location and the desired humeral location. This resulting vector of muscle forces is then applied. The electric cylinders retract or extend as needed changing the tension in the steel cables until the output from the in-line load cells indicates that the force in each muscle is within a specified force

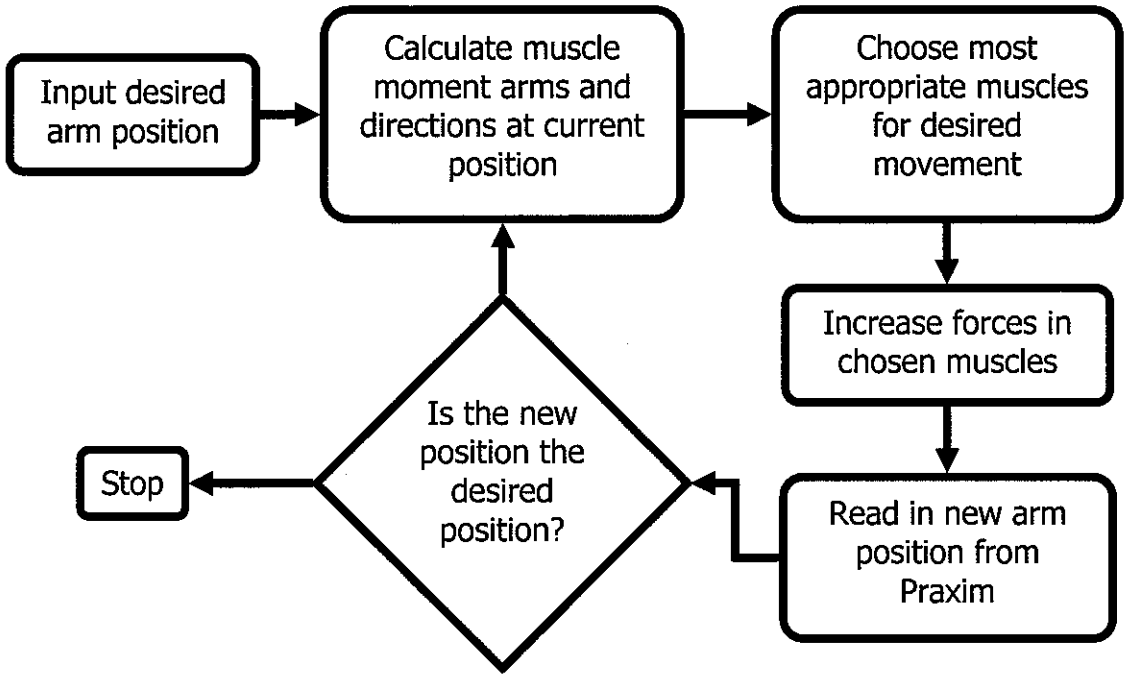

Figure 2.2: Function of first phase of shoulder simulator control system

tolerance of the level applied. This process is repeated until the difference in location is less than a specified positional tolerance (Figure 2.2).

The second phase of the control algorithm determines an optimal set of muscle forces at the desired position and applies that muscle force set. To accomplish this task, the control system relies on an internal mathematical model of the physical simulator. Inputs to this model consist of both digitized point data taken using Praxim and investigator-prescribed parameters. As in the first phase the control algorithm, muscle lines of action are calculated from attachment data and knowledge of current humeral position. To determine contact between the humerus and the glenoid, the surface of the humeral head is modeled by fitting a sphere, whose center lies at the center of rotation as determined by humeral circumduction, to digitized bony landmarks on the anterior, posterior, superior, and inferior aspects of the humeral head. The glenoid surface is similarly modeled as either an inclined plane, or a sphere or an ellipsoid of

prescribed radii fit to digitized landmarks on the anterior, posterior, superior, and inferior aspects of the glenoid surface (Table 2.2). Contact location is then determined analytically using knowledge of each surface's geometry and the location of the humeral head center as measured by Praxim. Contact between the humeral and glenoid surfaces is modeled as frictionless, so the resulting force vector is always normal to both surfaces at their point of contact. Linear springs of prescribed stiffness may be added between the digitized landmarks on the humeral head and those of the glenoid to account for capsular contributions to stability.

Table 2.2: Investigator Prescribed Anatomic Parameters

Parameter	*Description*
Glenoid radius (Sphere)	Radius of sphere to be fit to glenoid surface points to model contact
Glenoid radii (Ellipsoid)	Superior-inferior and anterior-posterior radii of ellipsoid to be fit to glenoid surface point to model contact
Ligament stiffness	Linear stiffness of springs used to model shoulder soft-tissue envelope

Using this internal mathematical model, a nonlinear optimization is performed to determine the set of optimal muscle forces that minimize the sum of the muscle stresses cubed [15]. The objective function examined may be readily changed. This objective function was chosen because it has been shown to produce the least error among objective functions that do not require *a priori* assumptions about the anatomy of individual muscles [10]. Muscle stresses are calculated by dividing the measured muscle force in each muscle by a published value of that muscles physiological cross-sectional area (PCSA) [43]. Constraints are added to insure that muscles act only in tension and that no muscle can apply a force greater than the product of that muscle's PCSA and a specific tension of $140N/mm^2$ [43]. Additional constraints on muscle

forces, humeral rotations, and humeral head center translations may also be specified by the investigator.

2.2.4 Simulator Testing

A mechanical surrogate of a cadaveric shoulder was designed and created to test the simulator (Figure 2.3). To make the motion of the surrogate shoulder as simple as possible for the initial testing of both the physical simulator and the control system, translational degrees of freedom were removed from the glenohumeral articulation. A pure ball and socket joint was created using a custom-machined ultra high molecular weight polyethylene (UHMWPE) cup and a 22 mm diameter cobalt-chrome femoral ball. A 22 mm ball was selected to maximize the thickness of the glenoid cup and to eliminate impingement between the cup and the humeral muscle insertion posts. For this testing, the surface of the glenoid was modeled as a portion of a sphere. Muscle insertion posts were arranged to replicate the experimentally measured muscle insertion locations of a single individual [74, 75], thereby insuring a consistent and physiologically reasonable anatomy was being represented. The location of the deltoid insertion along the shaft of the surrogate humerus was taken from the same subject and data set. The glenoid cup was then inserted into a scapular plate that was rigidly affixed to the mounting plate of the shoulder simulator. To account for the weight of the of the full arm, the surrogate humerus was machined from aluminum and a 3.5 kg weight was positioned along the midshaft of the humerus at 318 mm from the center of rotation [64].

To assess whether the muscle effective origins that we had chosen were physiologically reasonable and whether the biomechanics of our shoulder replicated the *in vivo* condition, the moment arms of each muscle were calculated and compared

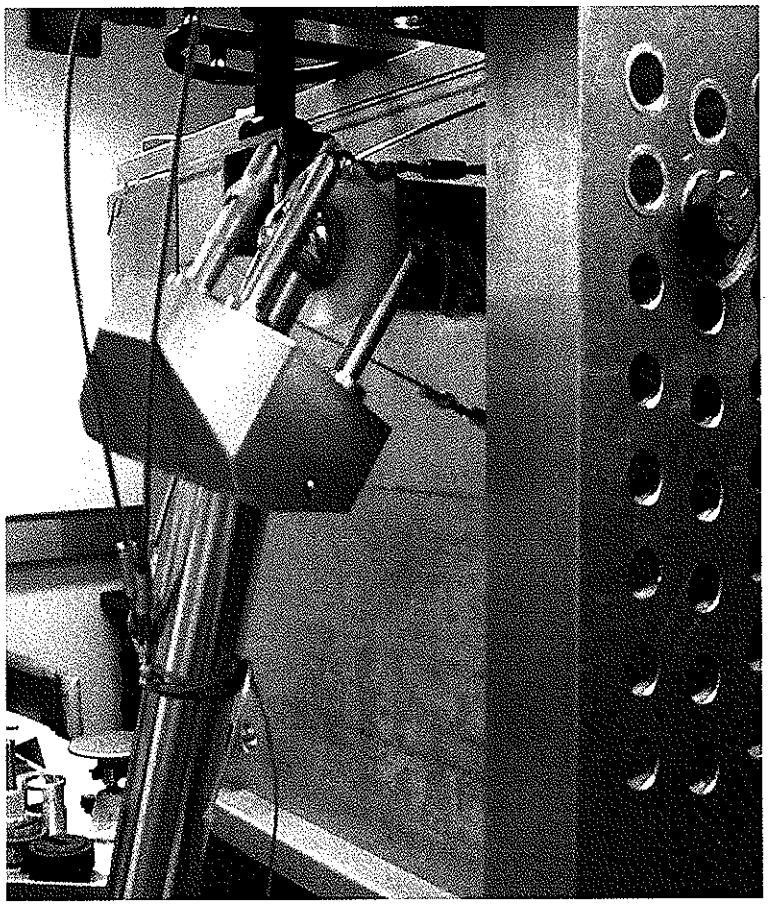

Figure 2.3: Surrogate shoulder attached to shoulder simulator mounting plate

to data from available literature. To determine the repeatability of the shoulder simulator control algorithm, three trials were performed in which the humerus was elevated from 0-80 degrees in 10 degree increments. At elevation angles greater than 80 degrees, there was visible impingement between the surrogate humerus and scapula, limiting our ability to test at higher elevation angles. To determine the effect of motion discretization on our results, an additional two trials were performed in which elevation occurred across the same 0-80 degree range in 5 degree increments. The error between the desired humeral position and the actual humeral position after optimal force application was calculated for each position.

2.3 Results

2.3.1 Simulated Moment Arms

The muscle moment arms created by our surrogate shoulder in general were able to replicate the basic function of each of the muscles being examined. The middle deltoid, anterior deltoid, and supraspinatus were positioned to always act as humeral abductors (Figure 2.4). The posterior deltoid acted as an adductor at low degrees of elevation and switched over to the role of abductor only as elevation increased. However, although the general characteristics of the abductors were replicated, their precise moment arms were not. This is most evident with the middle and anterior heads of the deltoid. The moment arm of the middle deltoid reached approximately 30 mm in anatomical studies [42, 62], while our middle deltoid moment arm approached 75 mm. The situation with the anterior deltoid was similar, although not as severe. Cadaveric studies have reported the moment arm of the anterior deltoid to be similar to that of the middle deltoid, approaching 30 mm. Our surrogate shoulder, however, exhibited anterior deltoid moment arms of nearly 50 mm.

Our surrogate shoulder was also able to replicate the general behavior of the rotator cuff muscles (Figure 2.5). As expected the subscapularis was the primary internal rotator of the humerus and the infraspinatus and teres minor were responsible for external rotation. Again however, although basic muscle function was correct, the magnitude of each muscle's moment arm was not necessarily so. Although the moment arms exhibited by the two sections of the subscapularis were similar to values obtained through cadaveric study [44, 62], the moment arms of both external rotators were less than what has been seen previously.

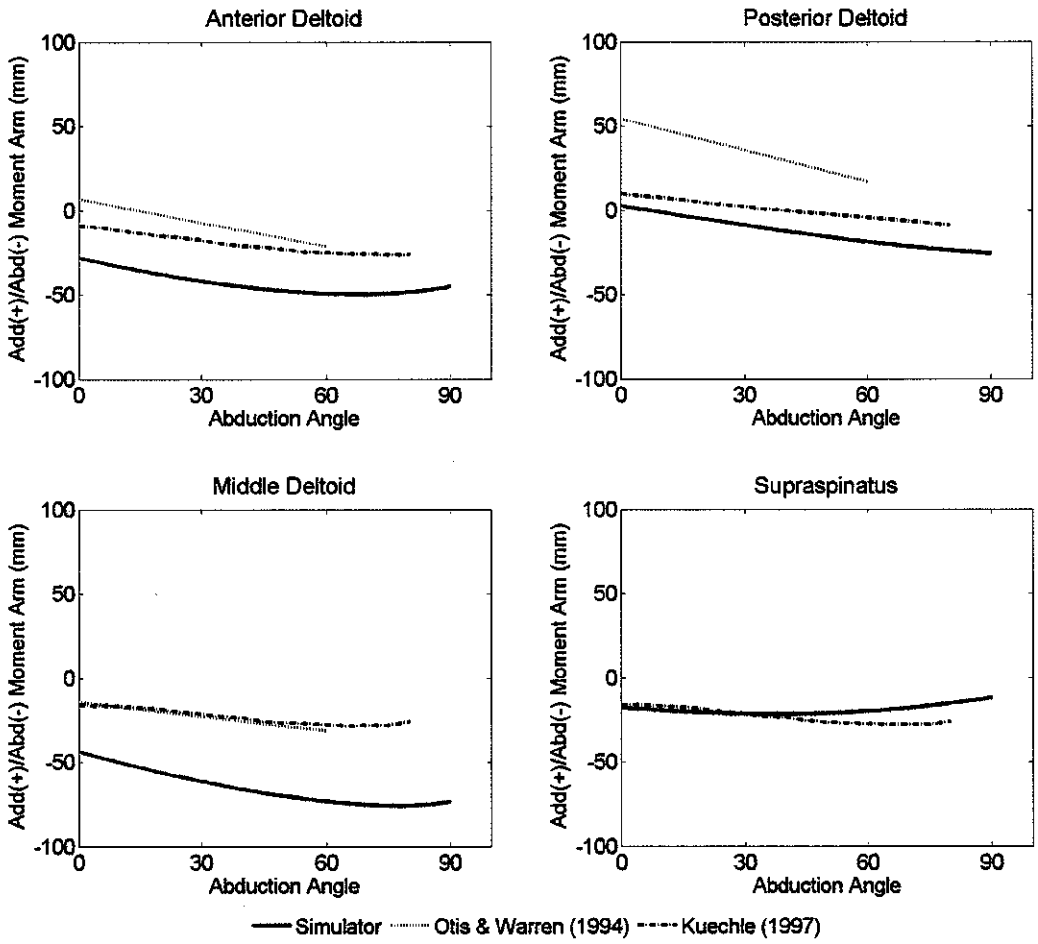

Figure 2.4: Abduction moment arms for the primary abductors of the shoulder for the surrogate shoulder shown alongside experimental values derived from anatomical studies

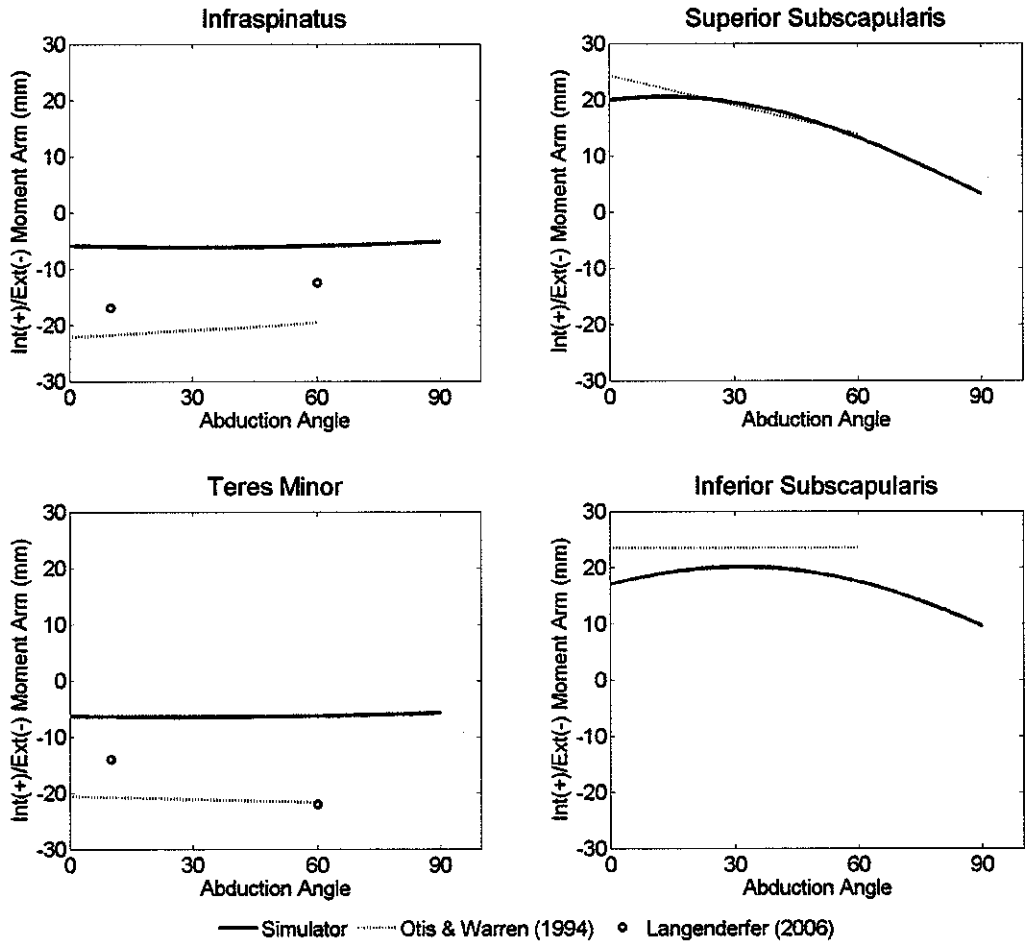

Figure 2.5: Rotation moment arms for the primary rotators of the shoulder for the surrogate shoulder shown alongside experimental values derived from anatomical studies

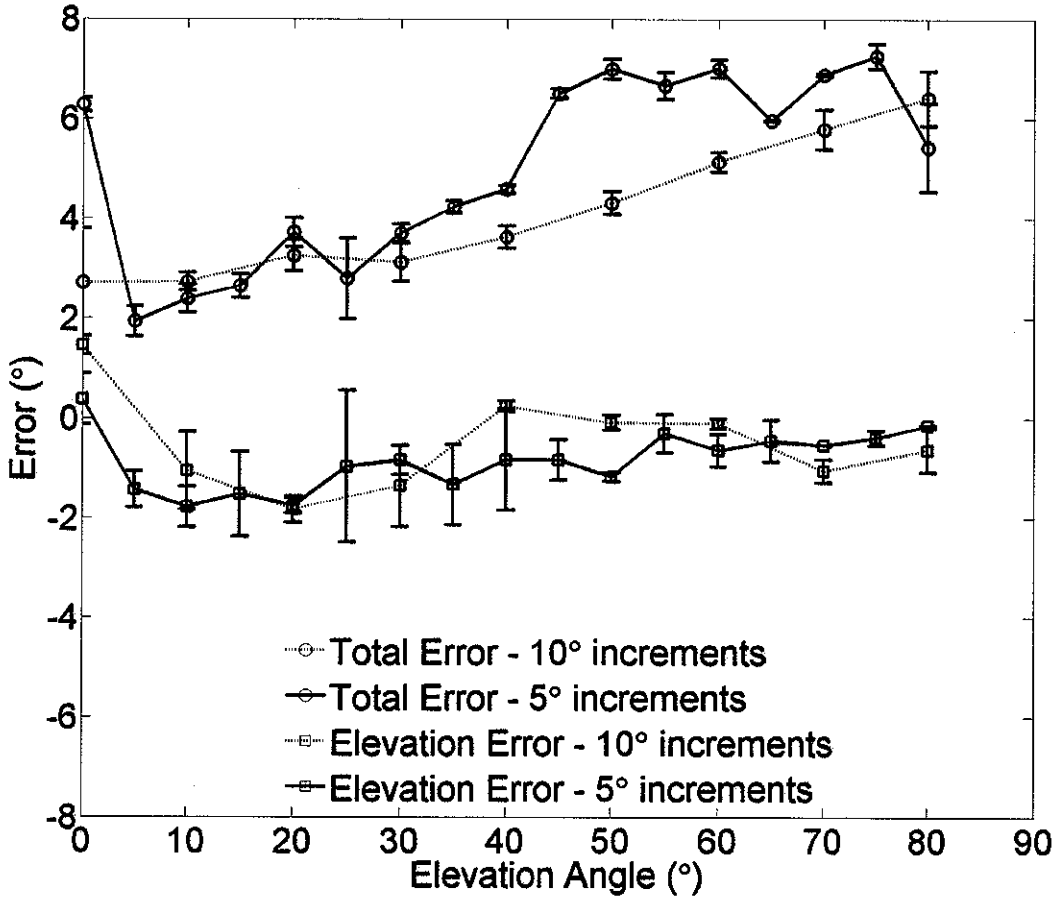

Figure 2.6: Total angular and elevation angle deviation between predicted humeral position and actual humeral position when applying optimal force distribution

2.3.2 Angular Error

The maximum total angular error for all trials never exceeded 8 degrees (Figure 2.6). Trials in which the desired elevation angle was increased in increments of 5 degrees rather than increments of 10 degrees demonstrated no reduction in the magnitude of the total angular error. Although the maximum total angular error was as high as 7.4 degrees, the maximum magnitude of error in the elevation angle when applying the calculated optimal force distribution to the simulator was only 2.1 degrees, indicating that the motion of the arm out of the plane of the scapula was the most sensitive to errors in the mathematical model used to determine the optimal muscle force

distribution and joint contact force.

2.3.3 Muscle Force Distributions

The muscle force distribution profiles were similar when elevating in both 5 and 10 degree increments (Figure 2.7). In both situations, the primary muscle acting over the entire range of glenohumeral elevation was the middle deltoid, carrying 117 N of force at 80 degrees of elevation. Among the muscles of the rotator cuff, the infraspinatus also exerted substantial force on the humerus in both the 5 and 10 degree increment trials, reaching its maximum value of 72 N when elevating in 5 degree increments and 86 N when elevating in 10 degree increments. The posterior deltoid also became more active as elevation angle increased.

2.3.4 Contact Forces

Predicted contact forces at the glenohumeral joint were found to be similar for both the five and ten degree increment trials (Fig 2.8). In all cases the contact force at the joint increased as the elevation of humerus increased. The maximum predicted contact force reached approximately 200 N at 80 degrees of elevation for all trials.

2.4 Discussion

Traditionally *in vitro* shoulder simulators have required the investigator make detailed assumptions as to how the resultant force at the glenohumeral joint is distributed among the soft tissues that cross the joint. We have successfully developed a method of shoulder motion control that limits the number of assumptions that must be made to solve the muscle redundancy problem across the joint. In our method, rather than having an investigator assign forces to each muscle, the forces are determined by finding an optimal solution to a mathematical model that represents the

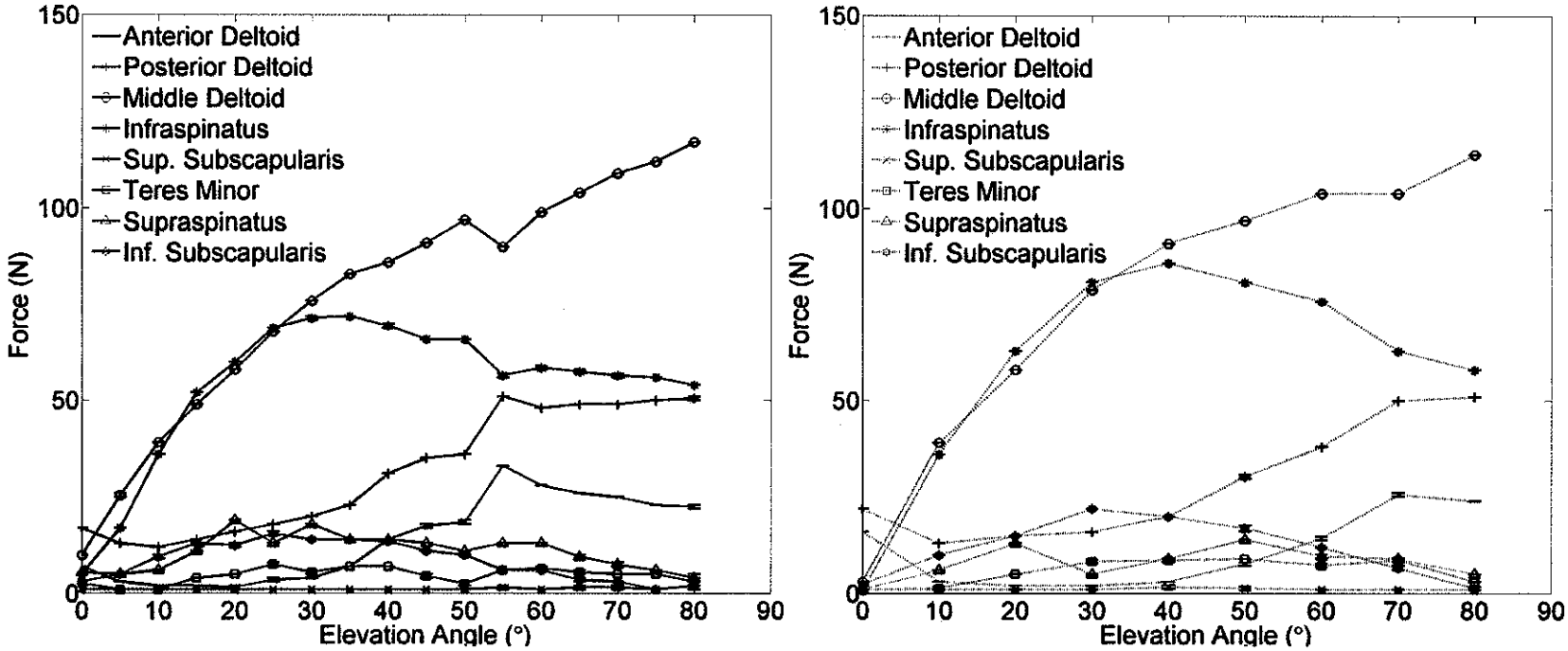

Figure 2.7: Predicted muscle force distributions when abducting the humerus in 5(-) or 10(··) degree increments

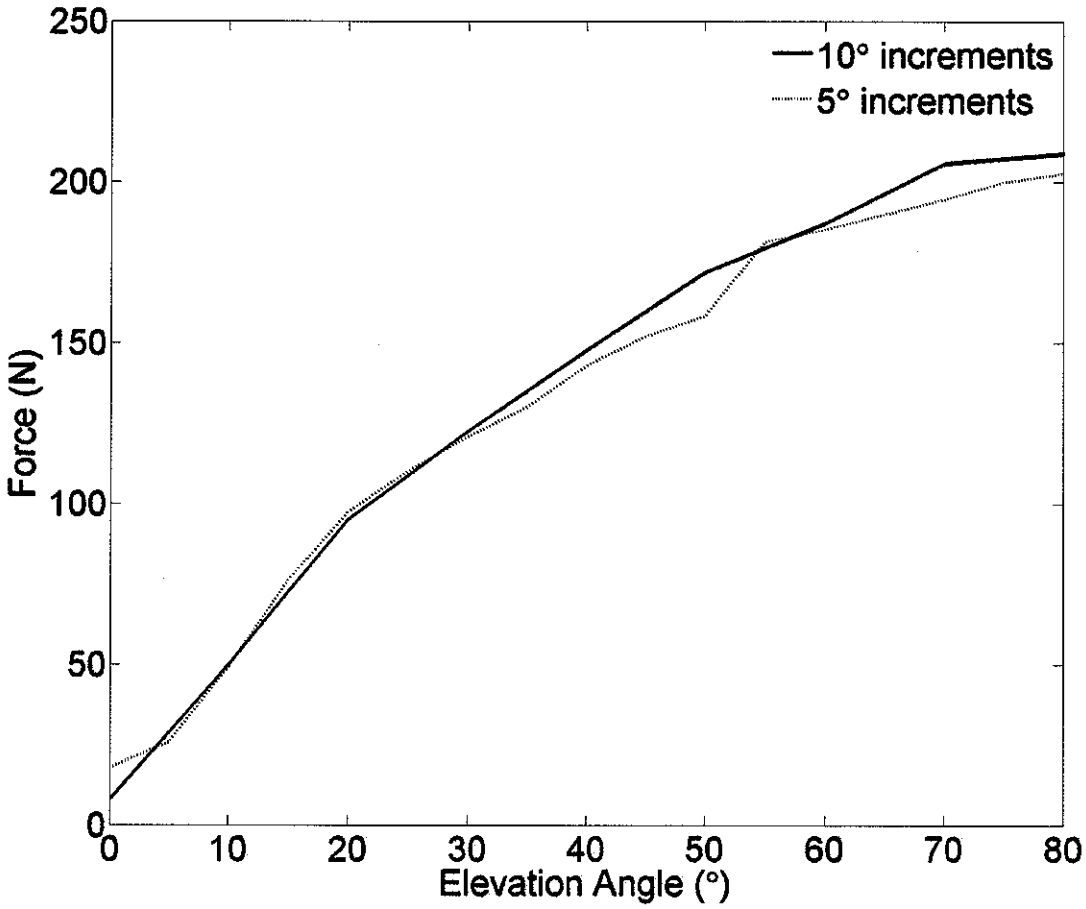

Figure 2.8: Predicted glenohumeral contact force when abducting the humerus in 5(-) or 10(··) degree increments

shoulder. Although this model also incorporates parameters that must be set by the investigator (Table 2.2), each of those parameters may be refined and verified through experimentation.

Even in the limited situation tested (0-80 degrees of scapular plane abduction), the simulator was not able to produce contact forces similar to those that had been observed previously. Existing models have estimated that the maximum contact force at the glenohumeral joint for unweighted straight arm abduction ranges from approximately 350 to 600 N [29, 64, 72]. Our shoulder simulator predicted maximum contact forces of approximately 200 N. However, this difference in predicted contact

forces is likely due to the difference in moment arms between the muscles in the study and those moment arms as determined anatomically and only serves to illustrate the necessity of having an accurate biomechanical model and an accurate method of distributing force when calculating contact force. Figures 2.4 and 2.5 demonstrate that the line of action assigned to the middle and anterior compartments of the deltoid in the surrogate shoulder provided the muscles with mechanical advantage greater that what is seen in anatomical study. Increasing the advantage of the heads of the deltoid causes less force to be required in these muscles to achieve humeral elevation. Since the muscles across the joint are carrying less force than they would if the moment arms were more in line with anatomical estimates, the contact force across the articular surface of the joint will also be lessened, explaining the discrepancy between our results and previously estimated contact forces. Thus, in future studies greater care must be taken to replicate the actual lines of muscle action if accurate predictions of glenohumeral contact force are sought.

Comparison of the predicted and actual humeral positions after applying the calculated optimal muscle force distribution indicates that, for the surrogate shoulder, as the humeral elevation increases the total error between the predicted and desired positions also increases. This is likely due to the increasing propensity of the muscle lines of action to contact and wrap around the surrogate humerus or glenoid as the arm is being elevated. This contact causes the direction of the actual force being exerted on the humerus to differ from the muscle line of action as calculated. As wrapping becomes more severe, the computational model used to determine the optimal force predictions becomes less faithful to the physical system. Thus, in order to simulate *in vivo* shoulder motions, it is necessary for both the physical system and the computational model to faithfully represent the shoulder anatomy.

While total deviations between the actual and predicted humeral positions remained small when testing our surrogate shoulder, it is likely that a cadaveric shoulder would experience substantially more disagreement between positions due to the increased parameter space of the computational model. The surrogate shoulder we used was well-behaved. Its articulation was designed to limit translational degrees of freedom and to act purely as a ball and socket joint. Actual cadaveric shoulders lack this degree of constraint and are much more likely to have a glenoid surface more similar to an ellipsoid rather than a sphere. An ellipsoidal fit to the points digitized on the glenoid surface requires that additional parameters be introduced into the model and thus offers increased opportunity for discrepancies to arise between the internal computational model and the physical shoulder. In addition, the cadaveric shoulder will retain various amounts of its joint capsule and glenohumeral ligaments after dissection. These structures act as stabilizers of the joint during motion *in vivo* and provide passive structures through which load may be transferred across the glenohumeral joint.

Future Work

To account for these issues and accurately simulate a cadaveric shoulder, additional protocols must be created to determine these newly introduced parameters. Each new cadaveric shoulder tested requires that each of these new parameters (glenoid radii, and net soft tissue properties) be determined. Going forward, we propose that reasonable ranges of each parameter be identified and each new cadaveric shoulder be tested using prospective sets of parameters drawn from those ranges of possible parameter combinations. For each shoulder, multiple draws will be made in order to most efficiently fill overall space created by the parameter ranges, and the new

cadaveric shoulder will be tested using the parameters from each draw. Over the space tested, a stochastically-based predictor function will be created that relates parameter values to the maximum positional error observed when performing a motion. The predictor function will then be used as an objective function in an optimization procedure to determine parameter values that minimize the maximum positional error. These optimal parameter sets will be used for all tests of that cadaveric shoulder and will be used as the starting point in determining optimal sets for new shoulders. As additional shoulders are tested, the distribution of each parameter across the population of shoulders can be determined. A mean value for each parameter can then be calculated and the set of these mean parameters can be used as the most likely parameter values to minimize positional error. Using this approach, the shoulder simulator that has been created and that has been demonstrated using a specially-designed mechanical surrogate shoulder will be extended to the testing of cadaveric shoulders.

Chapter 3

The Effect of Surgical Variations in Humeral Component Placement and Functional Loading on Total Elbow Contact Force

3.1 Introduction

Semiconstrained total elbow replacement (TER) is a common procedure for patients suffering from degeneration of the elbow joint due to rheumatoid arthritis or posttraumatic osteoarthritis and generally results in increased joint range of motion and decreased pain [50]. However, the long-term success rate of total elbow replacements remains less than that of other total joint replacements [40, 79]. The primary modes of failure of these implants are aseptic loosening and bushing wear [2, 80], both of which are related to the magnitudes of the joint contact forces that occur during activities of daily living. These force magnitudes are part of the mechanical environment around the implant and depend both on the activity being performed and

the position and orientation of the prosthetic components.

Forces during simple activities such as elbow flexion have been studied extensively [4, 6, 13], but the joint contact forces across the natural elbow during activities of daily living have been investigated only recently [12, 59] . Since the geometry of the contacting surfaces is altered in the replaced elbow, these studies do not offer direct insight into how joint contact forces across a total elbow change during motion. Furthermore, although the impact of implant placement on the kinematics of the elbow [69] and on observed clinical outcome [20] has been examined, no studies have been performed that link changes in joint contact force to implant position and orientation.

To understand how changes in implant position and orientation may contribute to loosening and bushing wear, three questions must be asked. First, are the contact forces across a total elbow replacement sensitive to specific variations in surgical placement or to specific types of motion? Second, do these relationships between contact forces and surgical placement remain true with increased functional loading or does increased loading have a nonlinear effect on contact forces across the joint and thus further complicate the behavior of the system? Lastly, are the magnitudes of the increased contact forces that result from these variations or motions large enough to increase wear of the polyethylene bushing and place the elbow replacement at an increased risk of failure?

3.2 Methods

3.2.1 Overview

To determine how muscle and joint forces varied with changes in the surgical placement of the humeral component, a computational model of the upper extremity

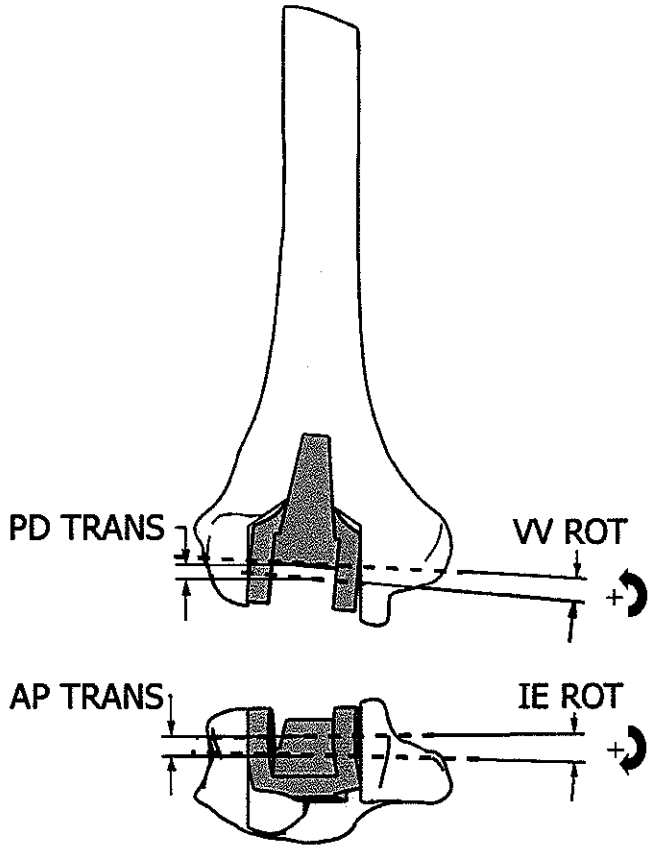

Figure 3.1: Translational (anterior-posterior and proximal-distal) and rotational (internal-external and varus-valgus) variations applied to the humeral component of the TEA

was employed in which the position and the orientation of the component axis were varied from those of the natural elbow axis (Figure 3.1). The effects of both translating the component +/- 5 mm in the proximal-distal (PD) and anterior-posterior (AP) directions and rotating the component +/- 5 degrees about the varus-valgus (VV) and internal-external (IE) axes were examined. The magnitudes of these variations fall within ranges observed following total elbow arthroplasty [20, 69].

3.2.2 Model Description

Original Model

Our computational model was created in Matlab 7 (Mathworks, Natick, MA) and

based on the anatomy of the upper extremity as described in a biomechanical model created by Holzbaur et al. [27] Briefly, the Holzbaur model includes 15 degrees of freedom to define the kinematics of the shoulder, elbow, wrist, index finger, and thumb. Three of these degrees of freedom are associated with the plane of elevation of the shoulder, the elevation angle of the shoulder, and the angle of shoulder rotation as all defined by the International Society of Biomechanics [81]. The articulation of the humerus with the scapula is modeled as a ball-and-socket joint and the movement of the shoulder girdle is constrained to follow the regression equations of de Groot and Brand [16]. The elbow is modeled as a revolute joint that articulates around an axis through the centers of the capitellum and the trochlear sulcus. Radioulnar articulation occurs about an axis passing from the center of the radial head through the center of the distal ulna. Wrist motion is represented using two degrees of freedom and motion of the index finger and thumb is represented using eight. Fifty muscles or muscle compartments are included in this description. The origins and insertions of these muscles were determined from digitized specimens and anatomical texts. The paths of the muscles and their associated tendons are defined by intermediate (or via) points and surfaces corresponding to anatomical constraints. The maximum muscle force possible in each muscle compartment is limited to the product of an experimentally determined physiological cross-sectional area (PCSA) and a maximum muscle stress of either 45 N/cm^2 for the muscles of the forearm and hand [31, 47, 48]. or 140 N/cm^2 for the muscles of the shoulder and elbow [5, 43, 60].

Model Modifications

To calculate the muscle and joint forces acting about the elbow and forearm, we further modified the Holzbaur model as described here. The masses of the body segments of the upper extremity and the locations of each body segment's center of

mass were added based on data reported by Veeger [76]. No attempt was made to add ligamentous or other soft-tissue structures to our model since ligaments at the elbow are often removed during total elbow arthroplasty and ligaments at the wrist have been shown to contribute little to the net moments about the joint during normal motions [18].

3.2.3 Computational Implementation

Any muscle present in the original Holzbaur model that crossed the humeroulnar, radioulnar, or radiocarpal joints was included in our computational model. Individual muscle compartments were able to act independently. Forces and moments across each of these joints were calculated. The line of action of each muscle was taken as the vector from distal to proximal between the two via points of the muscle that immediately spanned the joint of interest (Figure 3.2). The effects of wrapping surfaces on the lines of action were preserved in our model using custom wrapping algorithms. Intermediate muscle points resulting from wrapping around a surface were referenced in the same segmental coordinate system as the wrapping surface. Once normalized, these lines of action represented a unit force vector for each muscle. Moment arm vectors for each muscle were calculated as the cross product of the vector from the joint center to the spanning distal via point and the unit force vector for each muscle. The dot products of these moment arm vectors and the flexion axis of the elbow were calculated to determine the elbow flexion moment arms of each muscle. To insure the fidelity of our model to the Holzbaur model, the flexion moment arms calculated using our computational Matlab model were compared to moment arms calculated using the original model in SIMM (Musculographics, Inc., Santa Rosa, CA) (Figure3.3).

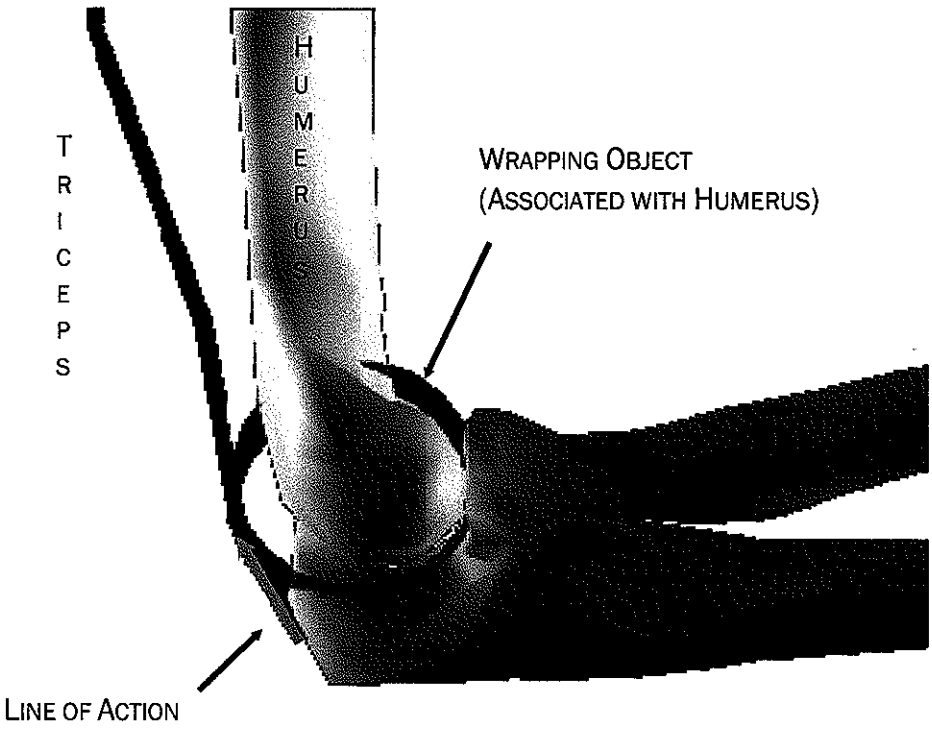

Figure 3.2: Change in the line of action of the triceps due to intersection with the wrapping object representing the distal humeral condyles. Additional via points are added to the muscle path where the path is tangent to wrapping surface.

After the unit force and moment arm vectors for each muscle had been calculated, resultant forces and moments at the joints were computed and nonlinear optimization was used to determine a muscle force distribution corresponding to a minimization of the sum of the muscle stresses cubed [15]. This optimization criterion was chosen because it has been shown [10] to produce the lowest error among a specific group of objective functions that do not require *a priori* assumptions concerning muscle fiber type. To ensure that physiologically relevant solutions were obtained, muscles were constrained to act only in tension and the force exerted by each muscle was constrained to be less than or equal to the maximum force established for that muscle as described previously. In addition, at the radiocarpal joint, the contact force was constrained to lie within 30 degrees of the axis of the forearm [12]. Since the axis of the forearm is always approximately normal to the articular surface of the distal radius,

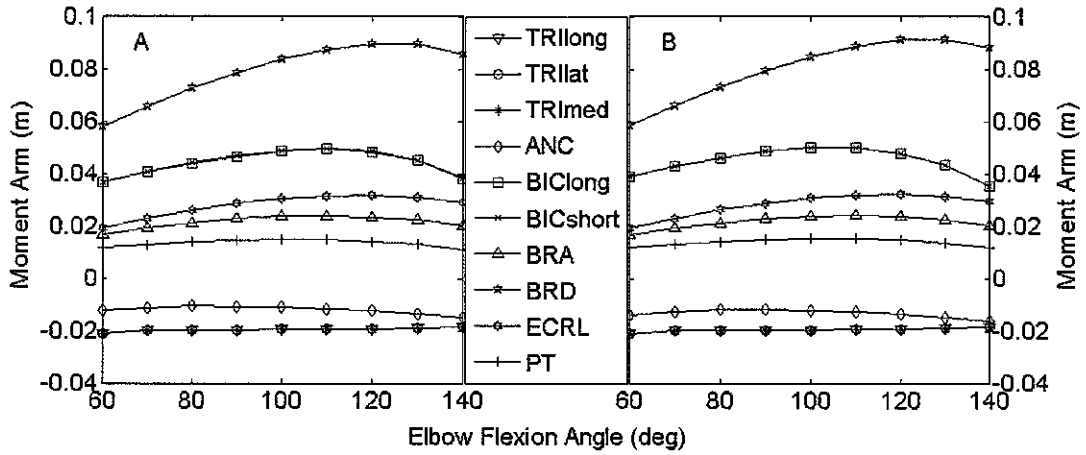

Figure 3.3: Elbow flexion moment arms of muscles crossing the elbow as calculated by A) our computational Matlab model and B) SIMM using the Holzbaur model.

this constraint insured joint stability throughout the simulations. The replaced elbow was able to transmit forces in three directions and to transmit moments about the two axes orthogonal to the rotational axis of the joint.

Joint forces and moments at the elbow center were decomposed into contact forces on the surfaces of the replaced elbow. To determine these contact forces, the total elbow replacement was modeled as a perfect hinge able to transmit axial force and radial forces along the implant axis at positions corresponding to the half-width (6 mm, as measured) of a standard Coonrad-Morrey elbow replacement (Figure 3.4). Using this model it was possible to determine the magnitudes of the forces on each edge of the ulnar component as well as the radial angles at which these forces were acting. A radial angle of zero degrees corresponded to a force directed anteriorly on the ulnar bushings while an angle of 90 degrees corresponded to a proximally directed force (Figure 3.4).

To determine the relationships between humeral component location and contact force across the joint, a 5N downward external functional load was placed in the hand. This

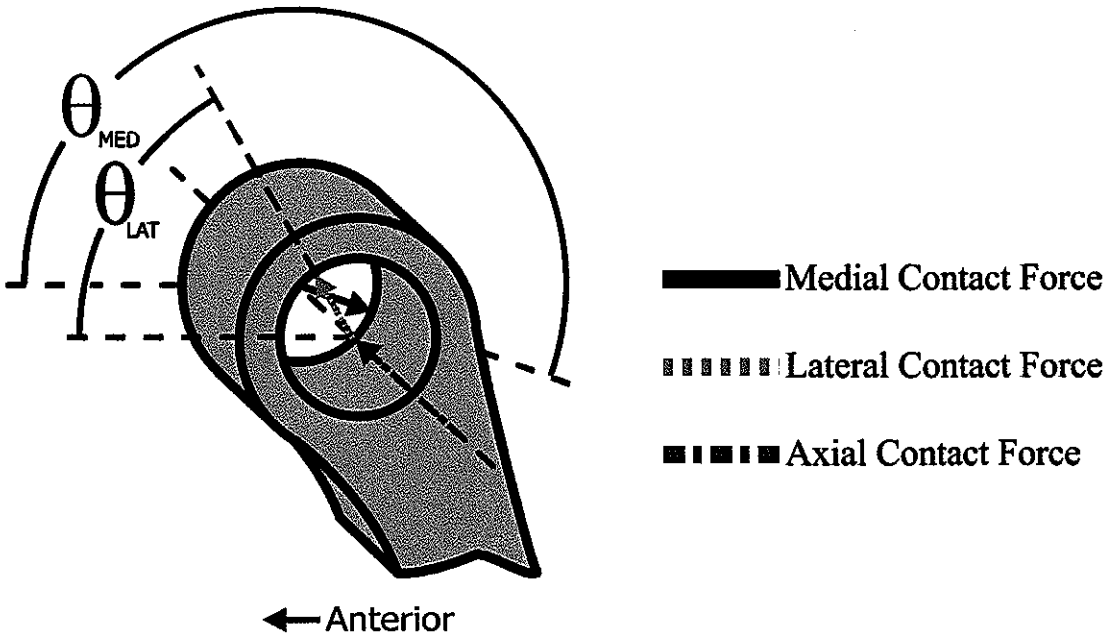

Figure 3.4: Equivalent system of contact forces on the ulnar component of the total elbow prosthesis. Radial forces occur at the medial and lateral faces of the ulnar component. Axial force direction is coincident with the axis of elbow flexion.

load was chosen in keeping with the activity restrictions typically placed on total elbow replacement patients. To investigate the effects of increasing the functional hand loading, additional load magnitudes of 10, 15, 20, and 25N were applied. When evaluating each functional load magnitude, kinematic data for two activities, eating with the hand [7, 68] and reaching to the side [7], were taken from the literature and applied to our model. In the original references, these motions are described as eating with the hand and reaching to the far right using a horizontal overhand cylindrical grip, respectively.

3.2.4 Statistical Analysis

To determine the first-order sensitivity of the maximum contact force to each of the translational or rotational parameters varied (Table 3.1), a linear regression was fit to each set of data. The slope of each regression is the sensitivity of the maximum

contact force to each of the parameters studied. The significance of each relationship was assessed by performing a one-way ANOVA on each of the distributions.

3.3 Results

For both the eating with the hand and reaching to the side motions with a 5N functional load, the maximum contact force was most sensitive to internal-external rotations of the humeral component axis with respect to the natural axis of the elbow (Figure 3.5D). Anterior-posterior translations (Figure 3.5A), proximal-distal translations (Figure 3.5B), and varus-valgus rotations (Figure 3.5C) of the component axis had little effect upon the magnitude of the maximum contact force.

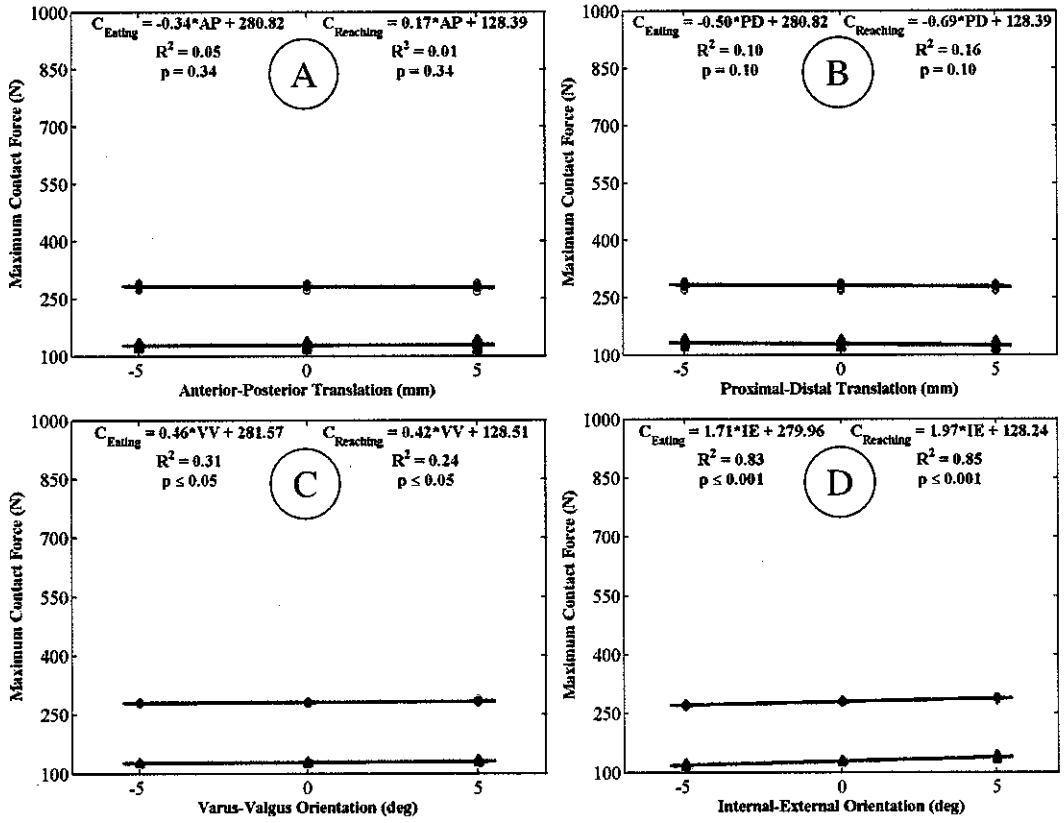

Figure 3.5: Variation of the maximum contact force on the ulnar bushing with changes in the position or orientation of the humeral component for (○) eating with the hand and (Δ) reaching to the side motions with a 5N applied hand load. Maximum contact force always occurs on the medial aspect of the component.

The variations observed in maximum contact force with a 5N functional load correlated most strongly with changes in the internal-external rotation of the implant. Changes in maximum contact force were much more weakly correlated with varus-valgus rotations, proximal-distal translations, and anterior-posterior translations of the humeral component. For both motions, internal-external and varus-valgus rotations caused variations in the maximum contact force that were significant ($p \leq 0.05$).

For all humeral positions described in Table 3.1, the maximum contact force magnitude when a 5N hand load was applied increased less than 12% from the contact force observed when the humeral component axis was coincident with the natural elbow axis (Table 3.1). The position of the contact force on the medial aspect of the ulnar component bushings varied little both throughout and between the motions and was always concentrated at the distal aspect of the ulnar component (-90.3° to -105.6°) (Figure 3.6). The position of the lateral contact force varied only slightly with changes in axis location and orientation for both motions, but did vary across the two motions. For the eating activity, the lateral contact force always occurred on the proximal aspect of the ulnar component (86.8° to 142.0°). When reaching to the side, the lateral contact force occurred instead on the posterior aspect of the ulnar component bushings (151.1° to -155.1°).

Analyses performed with increasing functional loads in the hand confirmed the results seen in the 5N applied load cases. For all cases of increased loading, the maximum contact force applied to the articular surface of the implant was most sensitive to internal-external rotations of the humeral component with respect to the natural axis of the bone (Figures 3.7-3.10). The maximum contact forces were not sensitive to displacements or to varus-valgus rotations for all cases of increasing functional load

Table 3.1: Maximum Contact force (N) across TER with Variations in Implant Alignment for ☐ Eating with the Hand and ▒ Reaching to the Side Activities with a 5N Applied Load

			Translation (mm) Proximal-Distal								
			5 Anterior-Posterior			0 Anterior-Posterior			-5 Anterior-Posterior		
			5	0	-5	5	0	-5	5	0	-5
Rotation (deg)	0		277	279	278	279	281	283	280	283	286
			125	124	124	130	129	128	132	131	131
	Int/Ext	5	285	286	281	289	290	288	290	292	293
			138	135	131	142	139	135	144	141	137
		-5	267	270	272	268	272	275	268	272	277
			113	114	116	117	119	121	120	122	124
	Var/Val	5	280	282	281	282	285	287	283	287	291
			128	126	125	133	131	130	136	134	133
		-5	277	279	278	279	280	281	280	281	283
			124	123	123	127	127	127	130	129	129

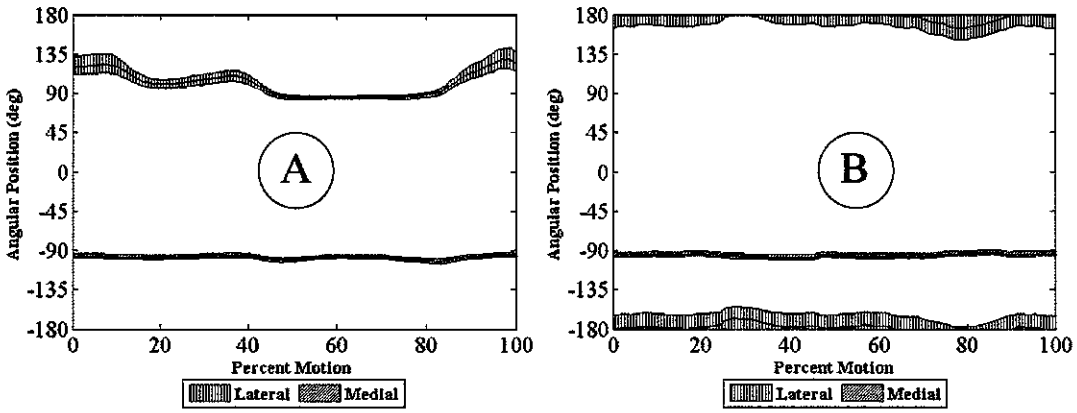

Figure 3.6: Radial position of the contact force while A) eating with the hand and B) reaching to the side. Interior lines show the position of the contact force when the humeral component is in the anatomic position. Shaded regions represent the entire range of contact force positions over all variations in humeral axis orientation.

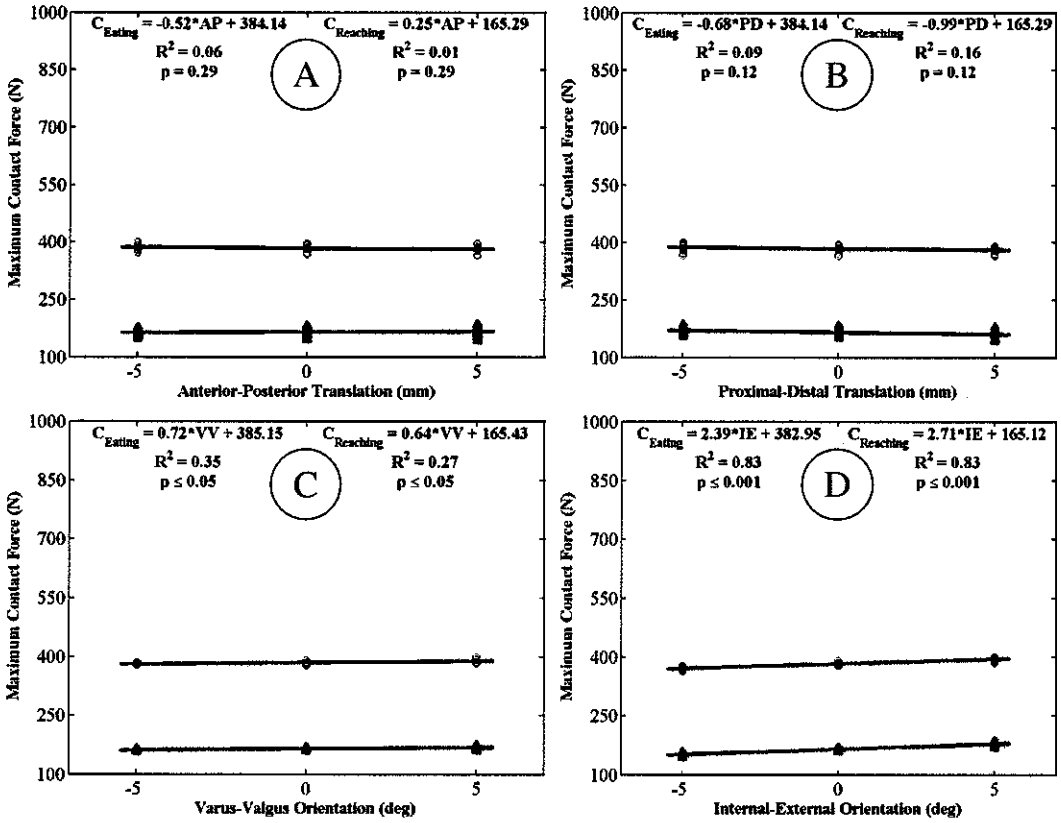

Figure 3.7: Variation of the maximum contact force on the ulnar bushing with changes in the position or orientation of the humeral component for (○) eating with the hand and (Δ) reaching to the side motions with a 10N applied hand load. Maximum contact force always occurs on the medial aspect of the component.

For all increases in applied functional load, maximum contact force across the implant correlated best with internal-external rotations of the implant. As with the 5N hand load case, internal-external rotations and varus-valgus rotations always caused changes in the maximum contact force that were significant ($p \leq 0.05$), while all translational variations in component position caused no change.

3.4 Discussion

Historically, few investigations have been made into the contact forces that arise on the articulating surfaces of a total elbow replacement during activities of daily living.

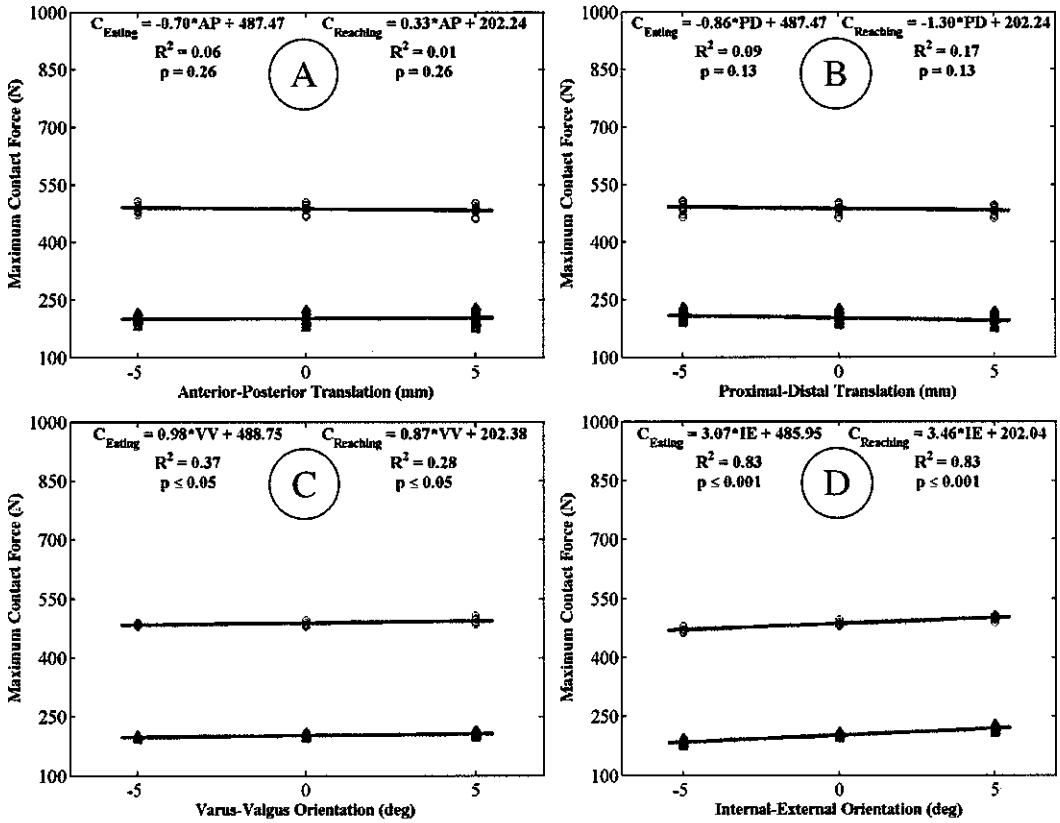

Figure 3.8: Variation of the maximum contact force on the ulnar bushing with changes in the position or orientation of the humeral component for (○) eating with the hand and (Δ) reaching to the side motions with a 15N applied hand load. Maximum contact force always occurs on the medial aspect of the component.

The objective of this study was to determine how contact forces across these implants varied throughout activities of daily living, with changes in the surgical position of the humeral component of the implant, and with increasing functional loads.

In our analysis, only rotation of the humeral component about the internal-external axis of the humerus produced a clear and significant effect on the magnitude of the maximum contact forces applied to the bearing surfaces of the implant for both motions. Even under internal rotation, however, the contact force increased only 4% over the value determined at the natural axis when eating with the hand and only 12% over the value determined when reaching to the side under a 5N functional load. Thus,

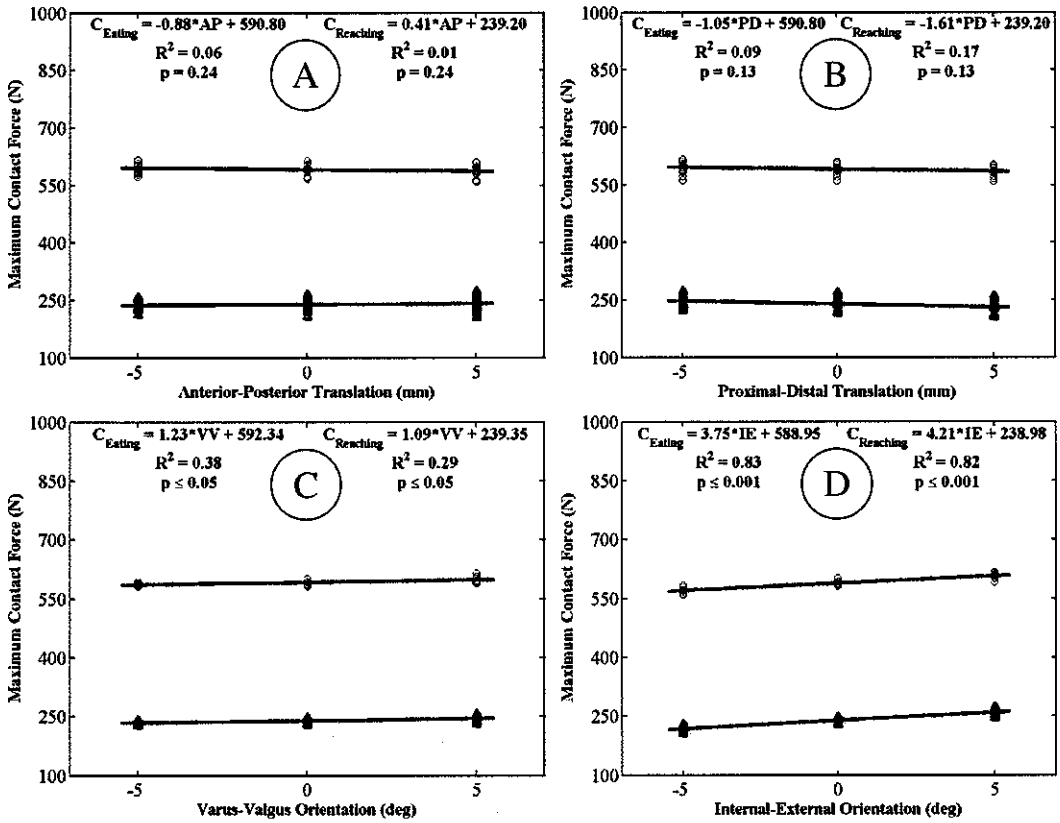

Figure 3.9: Variation of the maximum contact force on the ulnar bushing with changes in the position or orientation of the humeral component for (○) eating with the hand and (Δ) reaching to the side motions with a 20N applied hand load. Maximum contact force always occurs on the medial aspect of the component.

the variability inherent in the position of the humeral component after surgery seems to have little effect on the magnitudes of the contact forces across the implant, and therefore may have little overall effect on the longevity of the implant. Additionally, the effects of implant location on the maximum contact force across the total elbow replacement do not increase when the functional load in the hand is increased.

The locations of the contact forces throughout both motions, however, demonstrate that contact on the bushings of the ulnar component will always occur causing wear to either the proximal or posterior aspect of the ulnar bushings on the lateral face and to

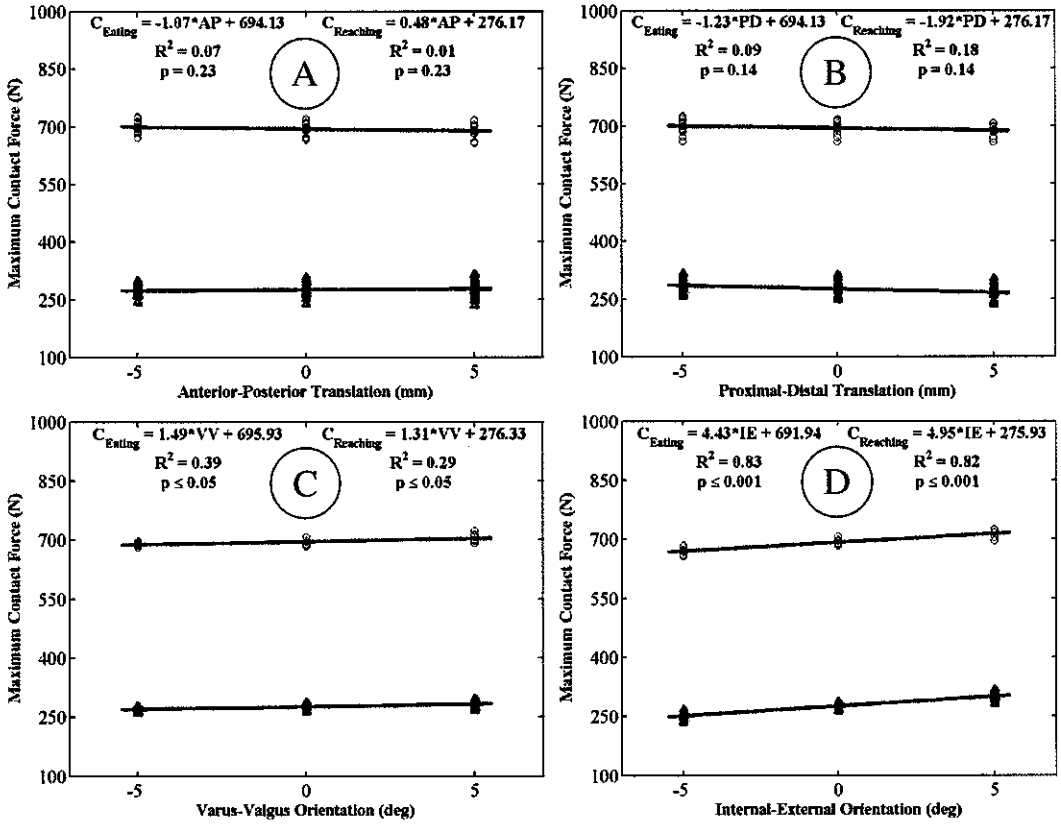

Figure 3.10: Variation of the maximum contact force on the ulnar bushing with changes in the position or orientation of the humeral component for (○) eating with the hand and (Δ) reaching to the side motions with a 25N applied hand load. Maximum contact force always occurs on the medial aspect of the component.

the most distal aspect of the bushings on the medial face. These wear patterns are consistent with clinical practice [57] in which bushing wear is assessed through an evaluation of increases in the amount of varus-valgus laxity of the replaced joint. Patterns such as these would be expected to lead to further deviations in the axis of rotation of the implant, causing additional varus and internal angulations, which would, from the results seen in this study, lead to additional increases in the contact force magnitudes across the components. These additional increases in contact force might contribute to a further increase in wear, which may lead to additional changes in the axis of rotation. The implant could thus enter into a cycle in which bushing wear and particle accumulation would continually accelerate. Therefore, although the results

shown do not directly indicate that internal rotations would adversely impact implant performance, it is possible that by internally rotating the humeral component during surgery, the cycle of degradation would begin earlier and overall implant life would be shortened.

The trends observed in this study are consistent with clinical observations. However, verifying our results by direct comparison with previous studies is difficult since most of these studies have been limited to simple motions of the elbow. Our computational model may be verified, however, by comparing the muscle force distribution predicted by our model during a simple motion to that predicted previously in literature [6] for the same motion. For these comparisons, the elbow was fixed at 90 degrees of flexion, a 10 N external load was placed in the hand, and the number of muscles active in our computational model was reduced to correspond to the set of muscles examined in the previous study. This set consisted of the biceps brachii (BIC), the brachialis (BRA), the brachioradialis (BRD), the flexor carpi radialis (FCR), the extensor carpi radialis longus (ECRL), the extensor carpi radialis brevis (ECRB), and the extensor carpi ulnaris (ECU). Muscle forces predicted by our computational model were in the range of those reported previously (Figure 3.11). However, the force in a specific muscle varied greatly depending on the optimization criteria used in the study. As expected, the muscle force distribution predicted when minimizing the sum of the muscle forces cubed in our study was most similar to the distribution predicted when minimizing the sum of the muscle forces squared in the previous study. Much of the difference between the forces predicted when using these two criteria can be explained by the different physiological cross-sectional areas (Figure 3.11) used in each study.

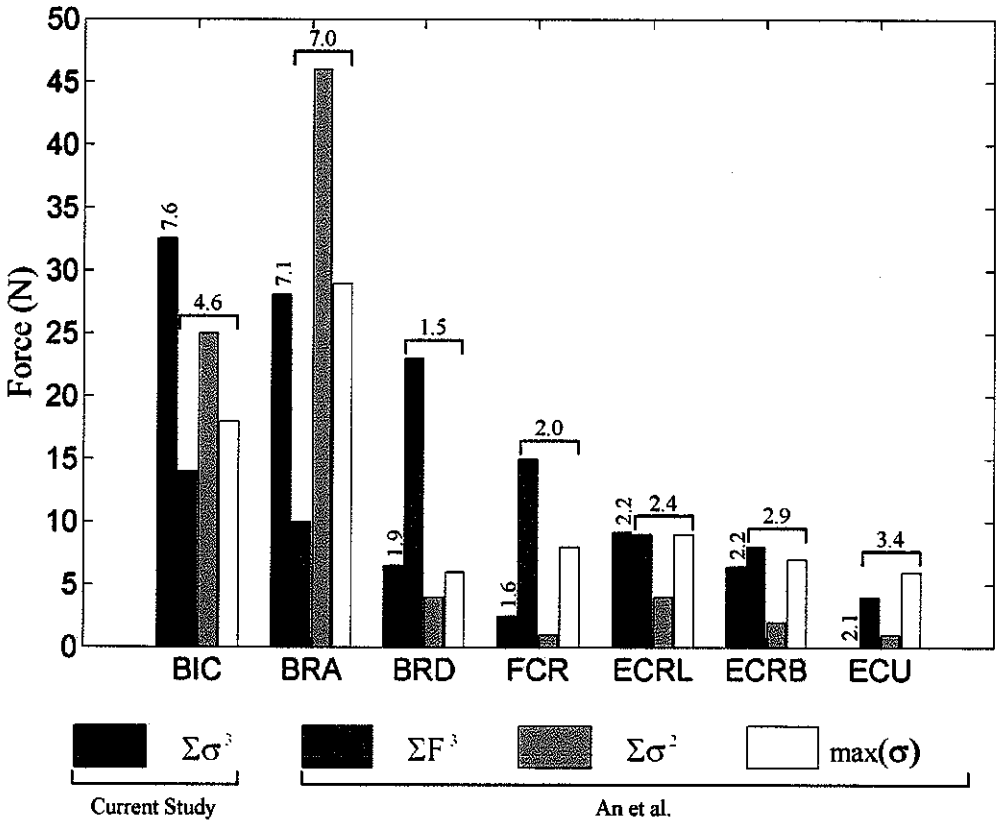

Figure 3.11: Distribution of muscle forces predicted by our model when minimizing the sum of muscle stress (σ) cubed and those predicted by An et al. [6] when minimizing the sum of muscle force (F) cubed, the sum of muscle stress squared, and the maximum muscle stress. Values above bars show the PCSA of the muscle assigned in each study.

The conclusions of this analysis should be interpreted taking into account that the model used is based upon small changes in the position and the orientation of the humeral component axis. This assumption was made to represent the situation that would normally be seen clinically, in which translations and rotations of the implant axis are within 5 mm and 5 degrees of the natural elbow axis. As such, the locations of intermediate muscle via points are assumed to remain constant with respect to the bone to which they are referenced. Extreme cases of translation or rotation, however, may cause more substantial changes in the muscle paths, which could lead to forces that do not follow the trends demonstrated in this study. Similarly, if the discrepancy

between the natural and replaced elbow axes is too great, the overall kinematics of a specific movement would likely change to preserve the functional objective of that movement. To confirm that our analyses did not affect the fundamental nature of the motions studied, the position of the wrist was tracked throughout each simulation and compared to the wrist position when the prosthesis axis was coincident with the natural elbow axis. The deviation of the wrist was less than 2.5 cm for all variations in the position or orientation of the implant axis, thereby demonstrating that the basic nature of the motions studied was not altered throughout our simulations.

Although only two motions, eating with the hand and reaching to the side, were examined in our analysis, they are qualitatively different and both represent large classes of activities, the first in which the elbow is flexed and the hand moves in the space anterior to the torso and the second in which the elbow is mostly extended and the hand moves in the space anterolateral of the torso. Both classes encompass common motions performed throughout daily life. In each class of activities the contact force positions and magnitudes are likely similar. Activities outside of these two general classes, however, could induce contact forces that vary differently with deviation of the implant axis and thus deserve further study.

In summary, although the results presented do not demonstrate large changes in maximum contact force as a function of changes in the position or orientation of the humeral component axis, the results indicate that wear in these implants may occur in a progressive manner leading to further increases in contact force. Therefore, it may advantageous to externally rotate the humeral component during surgery, thereby decreasing contact force as much as possible and perhaps slowing the overall wear rate.

Chapter 4

Upper Extremity Kinematics and Joint Loading in Total Elbow Replacement Patients and Normal Subjects During Activities of Daily Living

4.1 Introduction

The previous chapter demonstrated that the loads that contribute to the failure of a modern semiconstrained total elbow replacement will change based upon the surgical placement of the implant. Internally rotated implant positions were shown to have the potential of placing the implant at a higher risk of bushing wear and possible subsequent implant failure. One of the limitations of the previous study, however, was that it was based solely on kinematic data taken from existing literature that was obtained from a single subject performing two distinct tasks [7, 68]. It is unknown whether the kinematics of other subjects would resemble those of the subject originally tested. Also, although the two tasks we studied were substantially different

and offer a good idea as to levels of joint contact forces that might be experienced under typical activities, the question still remains whether there may be other activities, or variations of the previous activities, that could produce contact forces higher than those seen previously.

Furthermore, the kinematic data used to determine the forces across the implant were collected from a subject with no known degenerative changes at either the elbow or shoulder joints. There is certainly the possibility that total elbow arthroplasty (TEA) patients may have limited mobility, both at the elbow and the shoulder, that could influence the contact forces across the joint. Although many studies have been published examining different upper extremity tasks [8, 63, 68, 77], the kinematic data necessary to recreate the motions performed are rarely provided. Additionally, all of these studies have examined healthy subjects, so it impossible to determine from existing data whether degenerative changes in the upper extremity would influence kinematics or joint contact forces.

To address these issues, we recorded motion analysis data from both normal, unimpaired subjects and total elbow replacement patients while they performed the same tasks. The motion analysis data were then used to inform a computational model that predicted the forces across the elbow joint for both groups of study participants. With our analyses, we address three questions. First, does substantial variation exist among normal subjects as they perform an identical motion? Second, for the same tasks, do the kinematics of total replacement patients differ from the kinematics of the normal subjects? Lastly, do any changes in kinematics between the groups result in similar changes in the joint contact loads transmitted across the elbow?

4.2 Methods

4.2.1 Overview

This study was approved by the Institutional Review Board of the Hospital for Special Surgery and informed consent was received from each study participant. Motion analysis data were recorded from both normal subjects and total elbow recipients at the Motion Analysis Laboratory of the hospital. The kinematic data acquired through motion analysis were then input into a computational model to determine the joint reaction loads at the elbow. Differences in both kinematics and loads between normal subjects and total elbow replacement recipients were evaluated using statistical bootstrapping techniques.

4.2.2 Motion Analysis

Marker position data for sixteen total participants, eight normal subjects and eight total elbow recipients (Table 4.1), were collected at the Motion Analysis Laboratory at the Hospital for Special Surgery according to previously established protocols [66]. Using these protocols to determine upper extremity joint motion, eighteen reflective surface markers are placed on each study participant. Marker locations are used to establish 10 segments in a biomechanical model of the upper extremity. The segments

Table 4.1 Motion Analysis Participant Demographics

Normal Subjects				Total Elbow Patients		
Number	Sex	Age		Number	Sex	Age
1	Male	51		1	Female	51
2	Male	32		2	Female	44
3	Male	21		3	Female	52
4	Female	24		4	Male	78
5	Female	29		5	Female	48
6	Male	26		6	Female	71
7	Female	37		7	Female	79
8	Female	31		8	Female	50

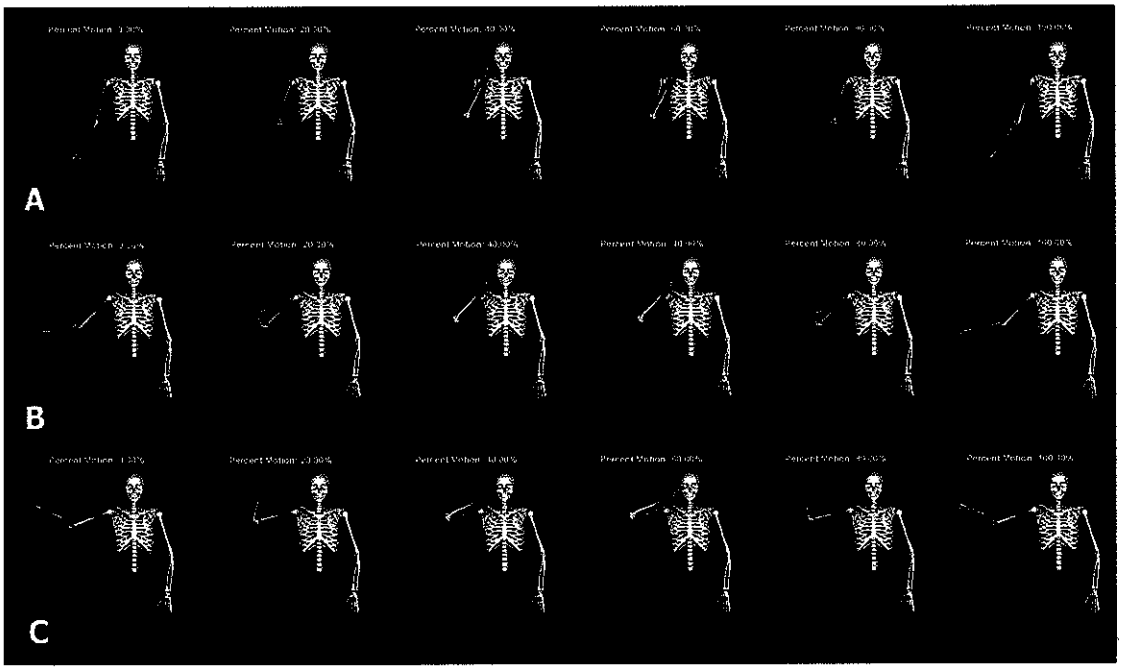

Figure 4.1: Feeding activities performed by study participants. Row: A) feeding with 0° humeral elevation, B) with 45° humeral elevation, C) with 90° elevation.

modeled are the head, neck, shoulder girdle, left upper arm, right upper arm, left forearm, right forearm, left hand, right hand, and pelvis. The articulations between the shoulder girdle and the upper arms are modeled as ball and socket joints with three rotational degrees of freedom. The elbows incorporate two degrees of freedom, elbow flexion and forearm rotation or pronation. The wrists are modeled as saddle joints with two rotational degrees of freedom, wrist flexion and wrist deviation.

Each study participant performed two activities of daily living (Table 4.2). First, a feeding activity was performed in which a 16 ounce bottle was placed on a shelf on the participant's affected or dominant side (Figure 4.1). Starting with the humerus lowered, elbow extended, and arm at the side, the participant was asked to lift the arm, grasp the bottle, raise the bottle to the mouth, and finally return the arm to the side. Variations of this motion were performed in which the participant attempted to hold humeral elevation constant at either 0, 45, or 90 degrees as the bottle was being lifted

to the mouth and returned to the shelf. Each participant performed each of these tasks six times.

In the second activity, the participant was asked to move a bottle from a shoulder-height shelf on the side of the participant's dominant or affected arm to a second shoulder-height shelf across the body (Figure 4.2). The participant then moved the bottle back to the original shelf. This was repeated three times by each participant.

Table 4.2: Motion Analysis Tasks Performed By Normal Subjects and TER Patients

General Motion	Specific Parameters	Number of Repetitions
Feeding	0° Humeral Elevation	6
	45° Humeral Elevation	6
	90° Humeral Elevation	6
Reaching to Shelf	Affected to Unaffected Side	3
	Unaffected to Affected Side	3

These two general tasks that we examined were chosen to more fully investigate the relationship between arm abduction and elbow reaction loads. The patterns of wear seen in retrieved semiconstrained total elbow replacements indicate that varus or internal moments are the largest contributors to the contact forces on the articular bushing in a replaced elbow [80]. Furthermore, the analyses we performed in Chapter 3 corroborate these findings. In our studies, when elbow flexion increases concurrently with arm abduction, the moment arm of the functional load about the axes of the elbow increases, increasing the reaction moment at the joint and the subsequent contact forces. Thus, as the elevation of the humerus with respect to the torso increases, with the tasks we have chosen, we expect to see an increase in the elbow loading.

To include the effects of functional loading on upper extremity kinematics, the

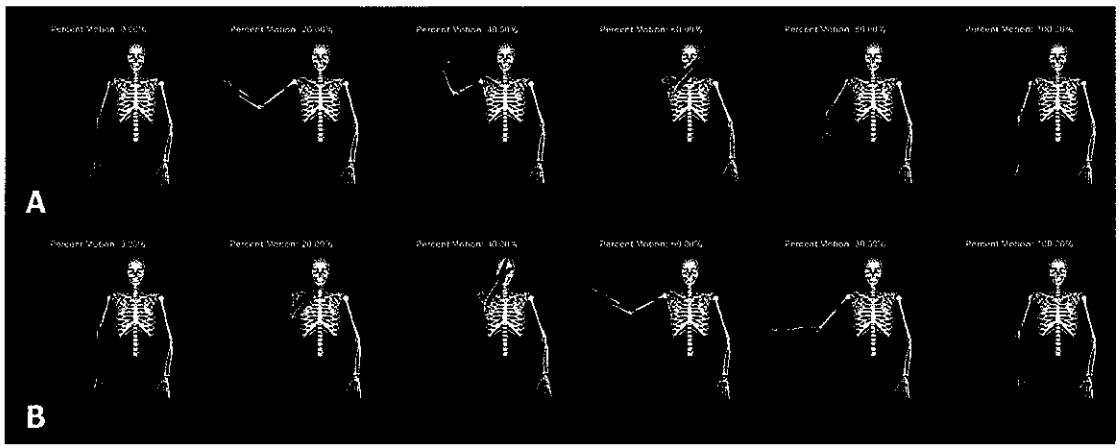

Figure 4.2: Reaching activities performed by study participants. Row: A) reaching from affected to unaffected side, B) from unaffected to affected side.

activities were performed with both an empty bottle and a bottle that had been filled with water. The limited one-pound loading was chosen in order not to exceed the functional capabilities of the total elbow recipients.

During each task, marker position data were captured using 10 Eagle series digital cameras (Motion Analysis Corporation, Santa Rosa, CA). Marker data were captured with a resolution of 1.3 million pixels per frame at a rate of 100 frames per second. The collected marker position data were converted into set of Euler angles (XYZ rotation order) using Visual3D (C-Motion, Inc., Germantown, MD). Euler angle data was imported into Matlab (Mathworks, Natick, MA) where each trial of each motion was visually identified and separated from surrounding kinematic data. Each trial was normalized with respect to time so that all tasks ran from 0 to 100 percent of each activity. Finally the Euler rotation sequence determined by Visual3D was converted into upper extremity joint angles as recommended by the International Society of Biomechanics (ISB)[81]. As named by the ISB, the seven joint angles obtained were shoulder plane of elevation, shoulder elevation, shoulder axial rotation, elbow flexion, forearm axial rotation, and wrist flexion and deviation.

4.2.3 Kinematic Analysis

A bootstrapping technique was used to determine whether there were significant differences between the kinematics of normal subjects and those of total elbow replacement patients. This bootstrapping technique was used to create 95% simultaneous prediction bands for the normal subject data [46]. As described by Lenhoff, these prediction bands were created by regarding each of the curves as a perturbation of a mean curve that can be described by the finite Fourier sum

$$f(t) = \mu + \sum_{k=1}^{K}\left(\alpha_k \cos\left(\frac{2\pi kt}{T}\right) + \beta_k \sin\left(\frac{2\pi kt}{T}\right)\right)$$

where K is chosen. In this case, μ is the overall mean value of the curve. This equation requires that each joint angle curve have the same starting and ending value; the joint curves as measured do not possess this property. To incorporate our curves into this framework, additional points were added to the extremities of the curve to satisfy this condition. Each individual joint angle curve was therefore represented as

$$f_i(t) = \mu_i + \sum_{k=1}^{K}\left(\alpha_{i,k} \cos\left(\frac{2\pi kt}{T}\right) + \beta_{i,k} \sin\left(\frac{2\pi kt}{T}\right)\right)$$

where $\mu_{i,1}\ldots\ \mu_{i,K}$, $\alpha_{i,1}\ldots\alpha_{i,K}$, and $\beta_{i,1}\ldots\ \beta_{i,K}$ were curve-specific coefficients. These coefficients, which were unknown for individual curves, were estimated by performing a least-squares fit of the above equation to each curve. A vector of the fitted components $\boldsymbol{W}_i = \left(\hat{\mu}_i, \hat{\alpha}_{i,1}, \hat{\beta}_{i,1}, \ldots, \hat{\beta}_{i,K}\right)^T$ was then assembled and used to create an estimate of both the mean and variance-covariance matrix of $\boldsymbol{W}_i$. The sample mean was determined as

$$\overline{\boldsymbol{W}} = \frac{1}{n}\sum_{i=1}^{n}\boldsymbol{W}_i$$

and the variance-covariance matrix was estimated as

$$\hat{\Sigma}_W = \frac{1}{n}\sum_{i=1}^{n}\left(\boldsymbol{W}_i - \overline{\boldsymbol{W}}\right)^T\left(\boldsymbol{W}_i - \overline{\boldsymbol{W}}\right)$$

An estimate of the mean curve was defined as

$$\hat{f}(t) = \overline{W}^T l(t)$$

where

$$l(t) = (1, \cos(2\pi t/T), \sin(2\pi t/T), ..., \cos(2\pi Kt/T), \sin(2\pi Kt/T))$$

and variability was defined as

$$\hat{\sigma}_{\hat{f}(t)} = \sqrt{l(t)^T \hat{\Sigma}_W l(t)}\,.$$

Prediction bands were then calculated by choosing a constant C_p so that

$$P\left\{\max_t\left(\frac{\hat{f}_{n+1}(t) - \hat{f}(t)}{\hat{\sigma}_{\hat{f}(t)}}\right) \le C_p\right\} = 0.95$$

where $\hat{f}_{n+1}(t)$ is a future draw from the mean curve and 95% is the desired prediction level. The 95% prediction band was then calculated as $\hat{f}(t) \pm C_p \times \hat{\sigma}_{\hat{f}(t)}$.

The joint angle curves for each total elbow patient were compared to the 95% prediction bands established using the normal subject data. If at any point throughout the activity, the total elbow patient's joint angle curve was found to fall outside of the normal subject prediction band, that curve was considered to be significantly different from the normal data and was categorized as abnormal, which means simply that the curve could not be considered to arise from the population of normal subjects. Any individual total elbow patient trial in which any of the joint angle curves characterizing that trial fell outside of its respective normal subject prediction band was also categorized as abnormal. The overall percentages of total elbow recipients' trials that were not explained by the normal subjects' prediction bands were then calculated. In order to determine how each joint angle contributed to the variability

between the normal subjects and the total elbow recipients, the percentage of joint angle curves over all patients that did not fall within the normal prediction bands for those curves was also calculated.

4.2.4 Force Analysis

The kinematic data from the remaining total elbow recipients were input into the computational model described in Chapter 3 to determine the muscle and joint reaction loads across the elbow and wrist joints throughout the collected motions. The joint reaction load consisted of three components of force in the anterior, proximal, and lateral directions. Moments at the elbow about the anterior and proximal axes of the ulna were also calculated. Joint reaction moments about the flexion axis of the elbow were zero. For this analysis, any total elbow patient who could visually be determined to be following a motion strategy that was fundamentally different from those used by the normal patients was excluded. Table 4.3 lists the excluded total elbow patients and the reason for their exclusion.

Table 4.3: Exclusion of Total Elbow Patients

Patient Number	Reason for Exclusion
2	Patient was only able to perform tasks while sitting rather than standing as indicated
3	Shelf level was above shoulder height when performing the reaching activities
7	Shelf level was below shoulder height when performing the reaching activities. Patient was permitted to perform tasks with excessive forward torso tilt

Joint loading from the observed tasks were evaluated similarly to the kinematic data analysis described above. Force and moment curves from the normal subjects were used to create 95% simultaneous prediction bands in the manner previously described.

Total elbow recipient load curves were then compared to these normal subject prediction bands. Any total elbow curve that violated the normal subject prediction bands was significantly different from the normal population and was categorized as abnormal.

4.3 Results

4.3.1 Kinematic Analysis

The prediction bands established from the joint angle curves of the normal subjects were unable to explain completely most of the kinematics of the total elbow patients (Table 4.4). Both when performing the feeding motion unloaded with the arm not elevated and when feeding loaded with the arm elevated to 90 degrees, none of the total elbow patients' trials were completely explained by the normal subjects. At best, only 25% of the total elbow patient's movements could be considered to arise from the normal population.

Table 4.4: Total Percentage of Total Elbow Patient Trials that Exhibit Joint Angle Curves Not Explained by the Normal Subject Prediction Bands

Activity	Feeding						Reaching			
Weighted	No			Yes			No		Yes	
Motion	0°	45°	90°	0°	45°	90°	Aff.→ Unaff	Unaff. →Aff	Aff.→ Unaff	Unaff →Aff
% Abnormal Subjects	100.0	81.2	90.0	87.5	97.9	100.0	83.3	95.8	79.2	75

Over all the tasks studied, the joint angles describing the wrist motion of the total elbow patients most often deviated from the normal subject's prediction bands (Table 4.5). However, for the feeding tasks it was wrist flexion in which a difference was

Table 4.5: Percentage of Total Elbow Patient Joint Angle Curves Not Explained by the Normal Subject Prediction Bands

Activity	*Weighted*	*Motion*	*Elevation Plane*	*Elevation Angle*	*Shoulder Rotation*	*Elbow Flexion*	*Pronation*	*Wrist Deviation*	*Wrist Flexion*
Feeding	No	0° Elevation	66.7	27.1	39.6	62.5	10.4	70.8	70.8
		45° Elevation	35.4	50.0	10.4	31.2	12.5	45.8	41.7
		90° Elevation	52.1	31.3	43.8	39.6	27.1	37.5	47.9
	Yes	0° Elevation	0.0	37.5	4.2	56.3	29.2	43.8	72.9
		45° Elevation	29.2	39.6	18.8	20.8	20.8	35.4	41.7
		90° Elevation	52.1	43.8	56.3	66.7	20.8	41.7	52.1
Reaching	No	Aff.→ Unaff.	54.2	16.7	4.2	16.7	29.2	62.5	41.7
		Unaff. →Aff.	70.8	20.8	4.2	33.3	29.2	66.7	25.0
	Yes	Aff.→ Unaff	37.5	20.8	20.8	29.2	41.7	41.7	12.5
		Unaff. →Aff.	45.8	20.8	8.3	25.0	29.2	62.5	12.5
Across all Trials			42.4	33.6	24.0	41.1	23.2	49.0	46.6

most often seen, while the reaching tasks had more variation in wrist deviation. Although the majority of the total elbow patients' joint angle curves are not completely explained by the normal subjects, the overall patterns of motion are similar between the normal subject and total elbow patient groups (Figures 4.3-8, 4.10, 4.12, 4.14, and 4.16). Thus, while many of the total elbow patients' joint angle curves are significantly different than the normal subject population, the magnitude of the difference is often small. Noticeable exceptions to this are the kinematics of TEA

Patient 7 during unloaded feeding with the arm at the side (Figure 4.3)

4.3.2 Force Analysis

As with the upper extremity kinematics, the prediction bands generated from the normal subjects for each of the components of the reaction load on the elbow could rarely explain the full mechanical loading environment present on the elbows on the total elbow replacement patients (Table 4.6). At best, 33% of the total elbow patient's loading environments could be considered to arise from the population of normal loading.

Table 4.6: Total Percentage of Total Elbow Patient trials that Exhibit Loading Curves Not Explained by the Normal Subject Prediction Bands

Activity	Feeding			Reaching	
Motion	0°	45°	90°	Aff.→ Unaff	Unaff→Aff
% Abnormal Trials	90.0	76.7	80.0	80	66.7

The internal/external moment on the elbow of the total elbow patients most often fell outside of the established normal subject boundaries (Table 4.7). Generally, the joint loading during the tasks of the total elbow patients was better explained by the normal subject data than were the kinematics. Also, though a substantial percentage of loads calculated from the total elbow patients' kinematic data cannot be explained by the normal data, it should be noted that the magnitude of the discrepancy between the total elbow patients loading curves and the normal subjects' prediction bands is always small (Figures 4.9, 4.11, 4.13, 4.15, and 4.17).

Table 4.7: Percentage of Total Elbow Patient Loading Curves Unexplained by the Normal Subject Prediction Bands

Activity	*Motion*	*Anterior/ Posterior Force*	*Proximal/ Distal Force*	*Lateral/ Medial Force*	*Varus/ Valgus Moment*	*Internal/ External Moment*
Feeding	0° Elevation	30.0	40.0	23.3	20.0	80.0
	45° Elevation	40.0	40.0	20.0	26.7	43.3
	90° Elevation	0.0	23.3	20.0	76.7	40.0
Reaching	Aff.→ Unaff	13.3	20.0	46.7	20.0	46.7
	Unaff.→Aff.	0.0	6.7	26.7	0.0	60.0
Across all Trials		19.2	29.2	25.0	33.4	54.2

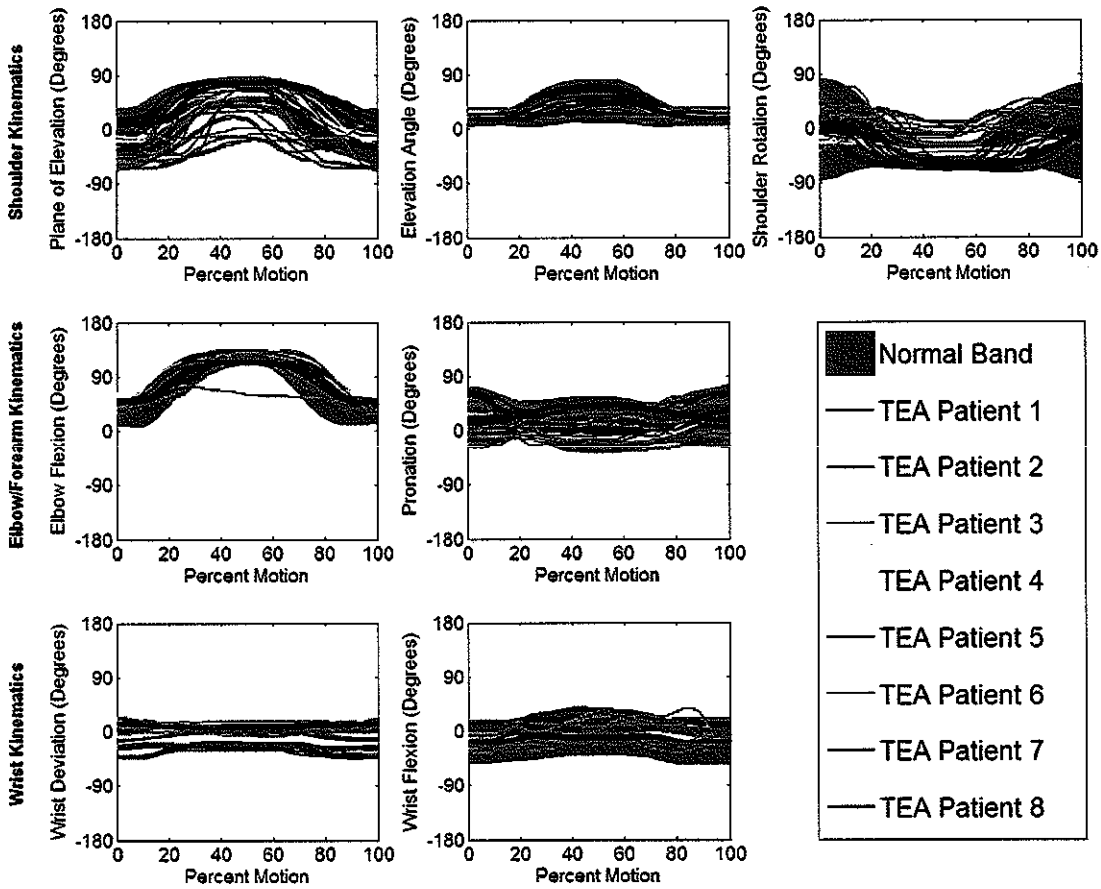

Figure 4.3: Joint angle curves during feeding with the humerus elevated 0 degrees and no hand load.

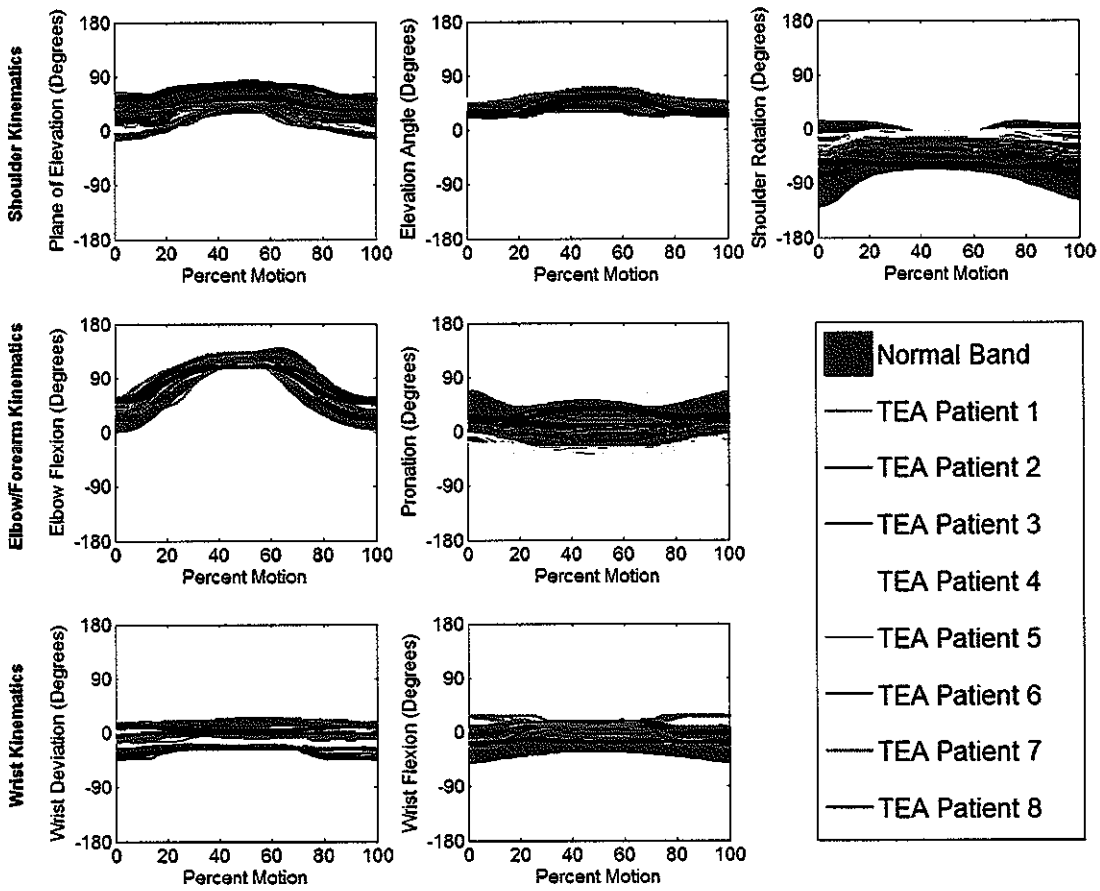

Figure 4.4: Joint angle curves during feeding with the humerus elevated 45 degrees and no hand load.

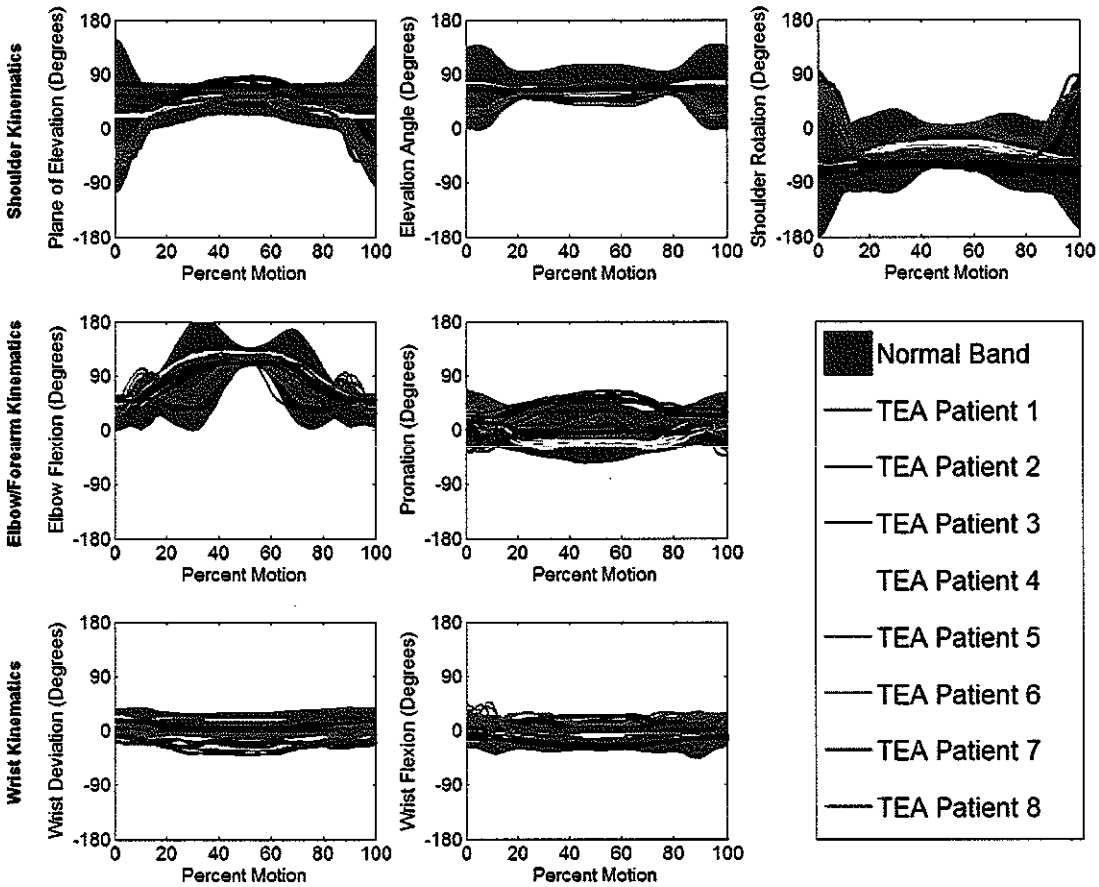

Figure 4.5: Joint angle curves during feeding with the humerus elevated 90 degrees and no hand load.

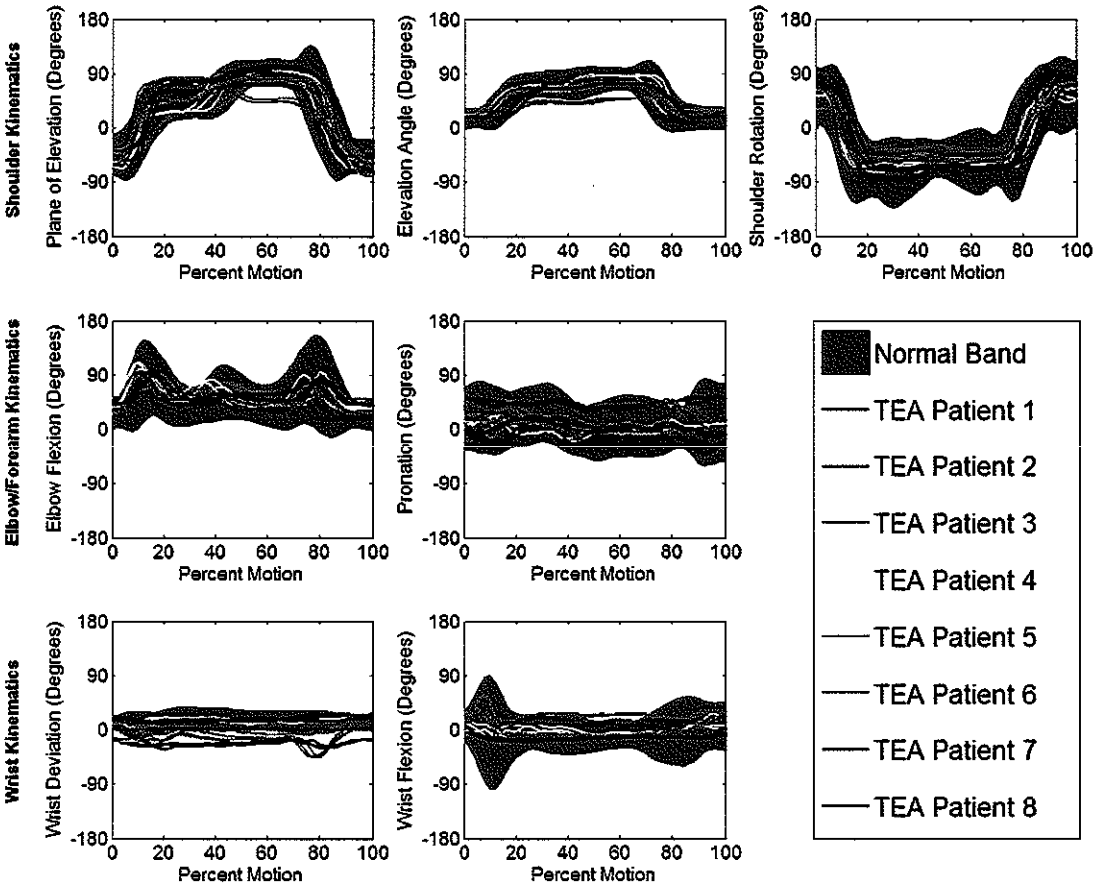

Figure 4.6: Joint angle curves while moving an object from a shelf on the subject's affected side to a shelf on their unaffected side with no hand load.

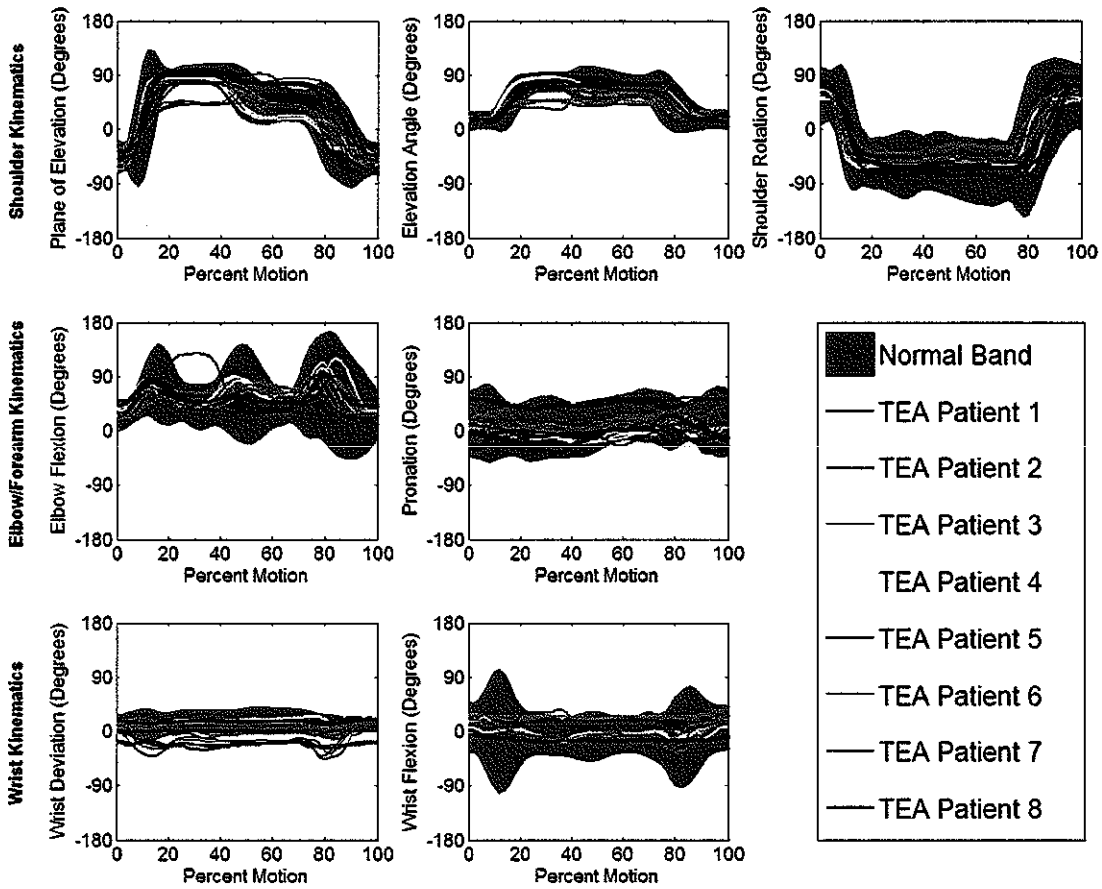

Figure 4.7: Joint angle curves while moving an object from a shelf on the subject's unaffected side to a shelf on their affected side with no hand load.

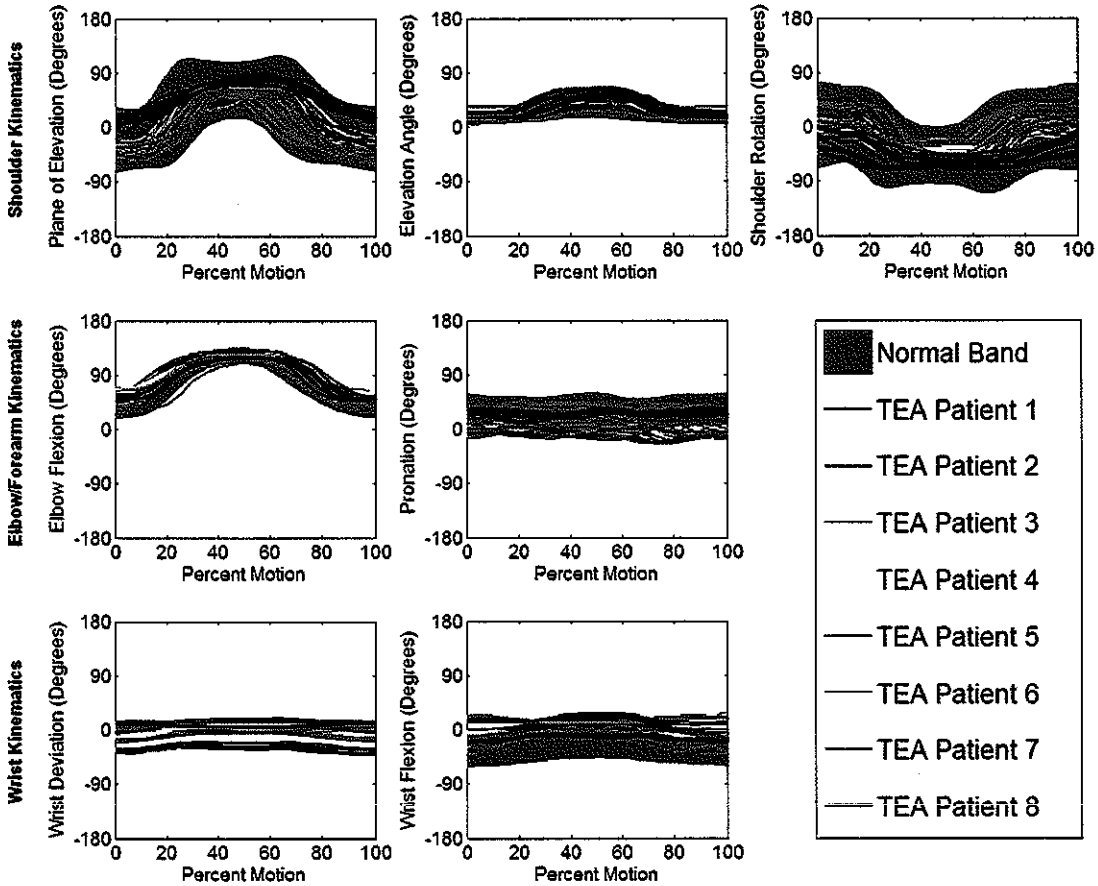

Figure 4.8: Joint angle curves during feeding with the humerus elevated 0 degrees and a 1 lb external hand load.

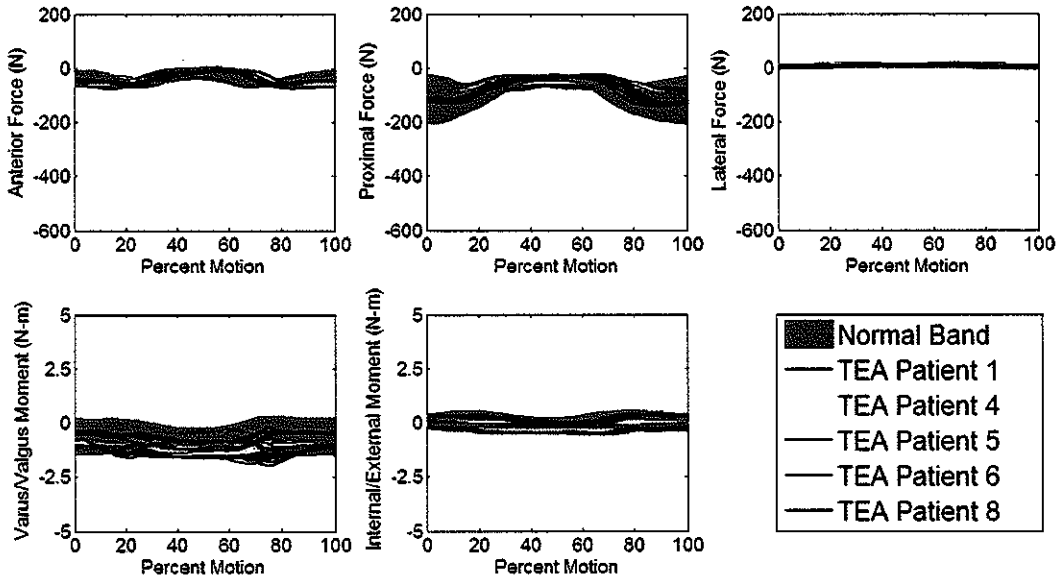

Figure 4.9: Reaction forces and moments on the elbow while feeding with the humerus elevated at 0 degrees with a 1 lb external hand load.

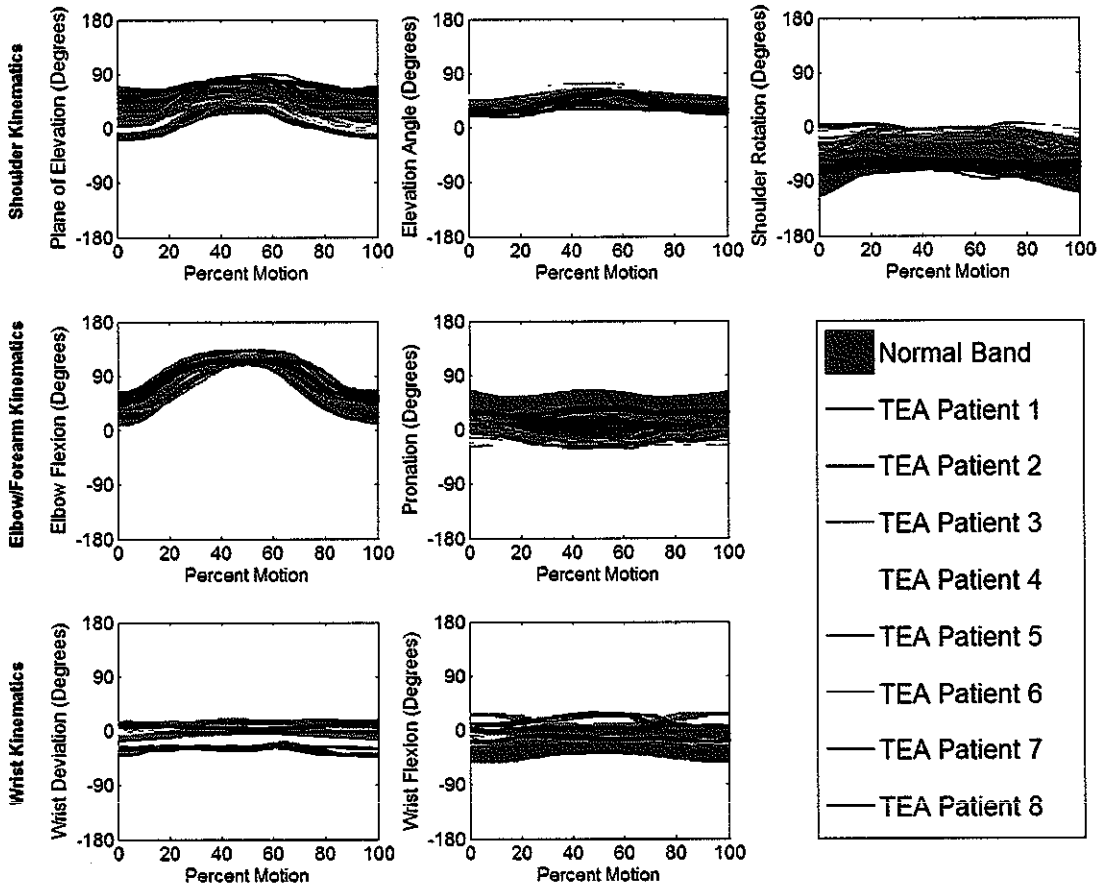

Figure 4.10: Joint angle curves during feeding with the humerus elevated 45 degrees and a 1 lb external hand load.

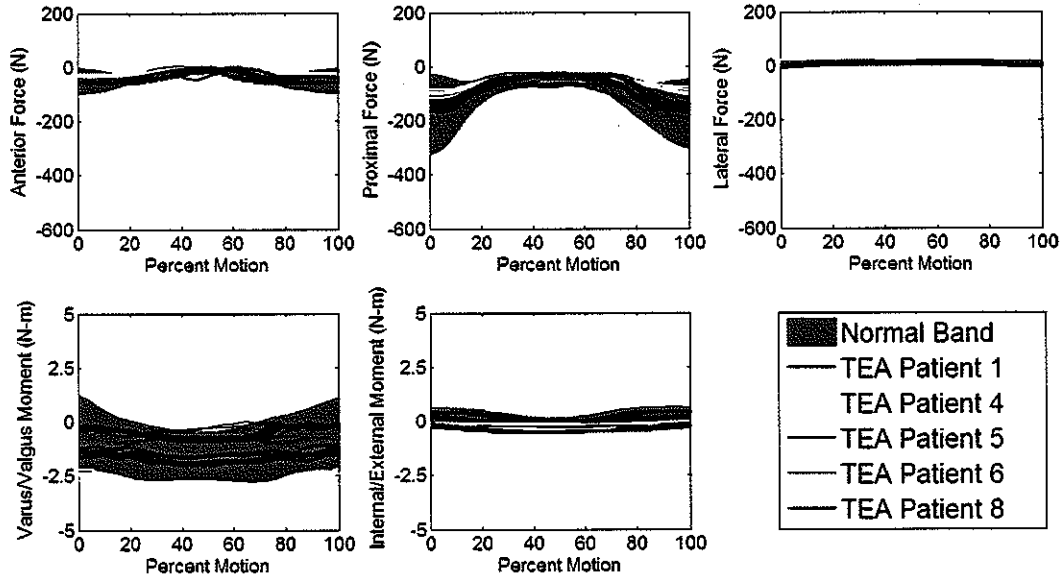

Figure 4.11: Reaction forces and moments on the elbow while feeding with the humerus elevated at 45 degrees with a 1 lb external hand load.

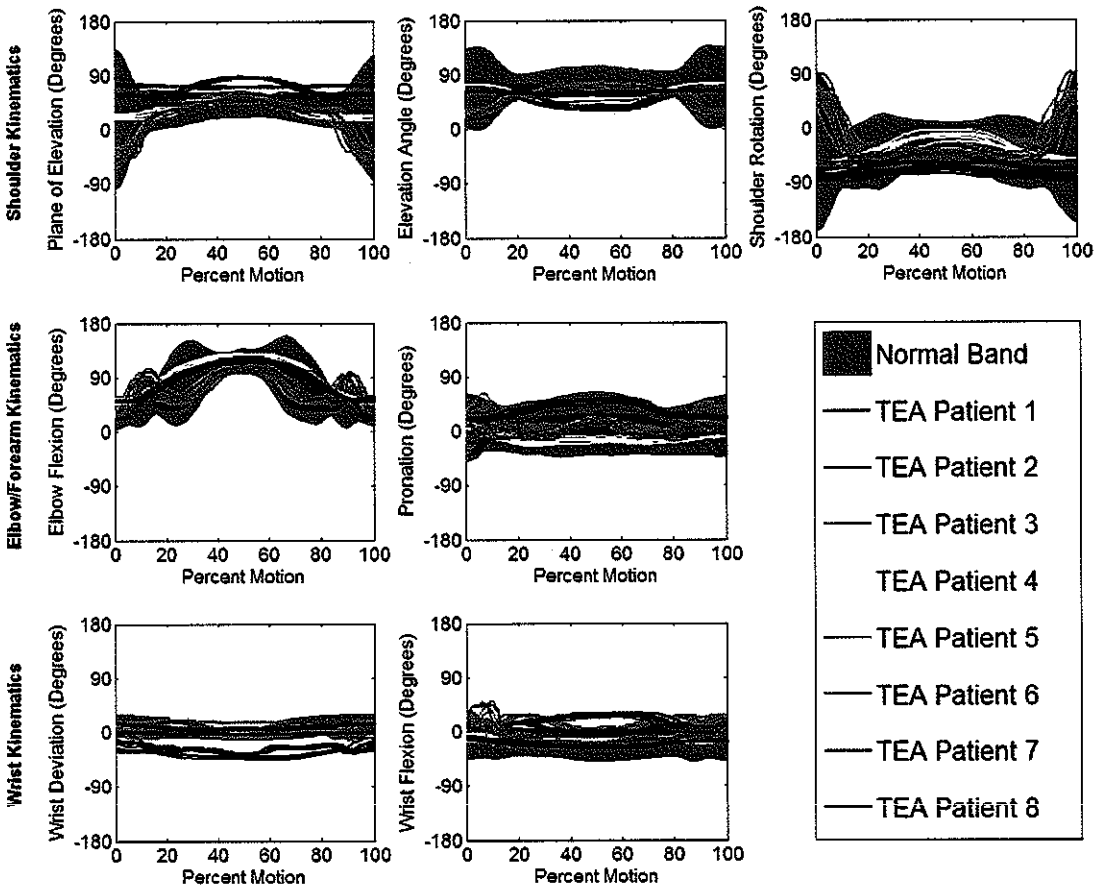

Figure 4.12: Joint angle curves during feeding with the humerus elevated 90 degrees and a 1 lb external hand load.

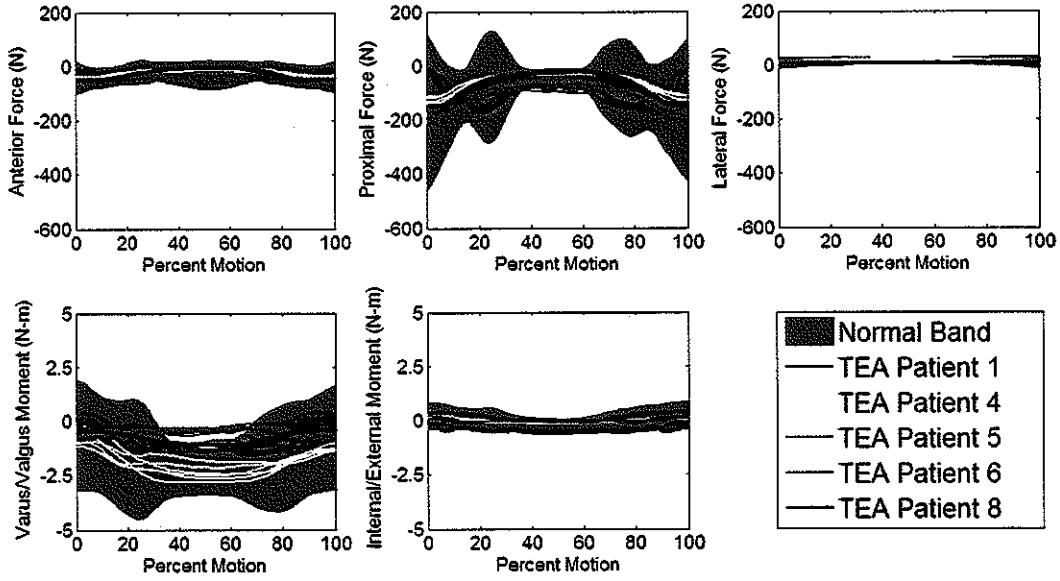

Figure 4.13: Reaction forces and moments on the elbow while feeding with the humerus elevated at 90 degrees with a 1 lb external hand load.

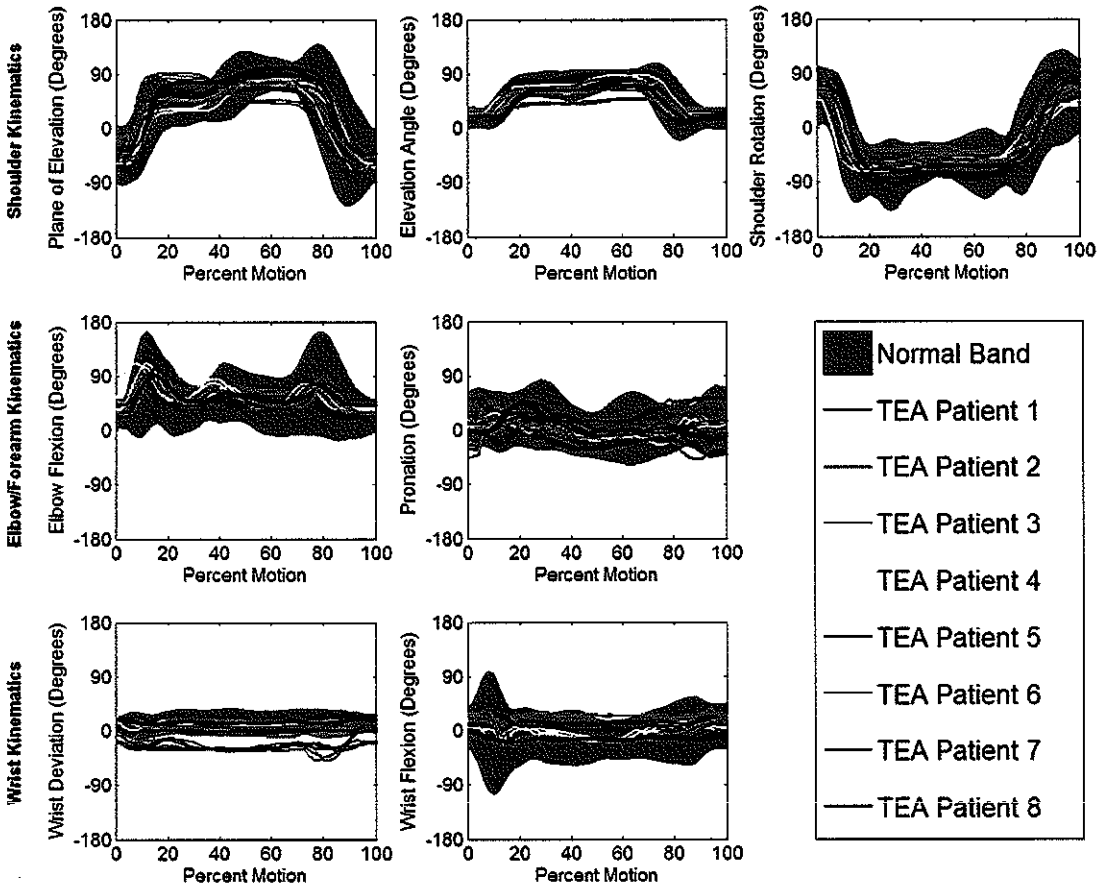

Figure 4.14: Joint angle curves while moving an object from a shelf on the subject's affected (or dominant) side to a shelf on their unaffected side (1 lb hand load)

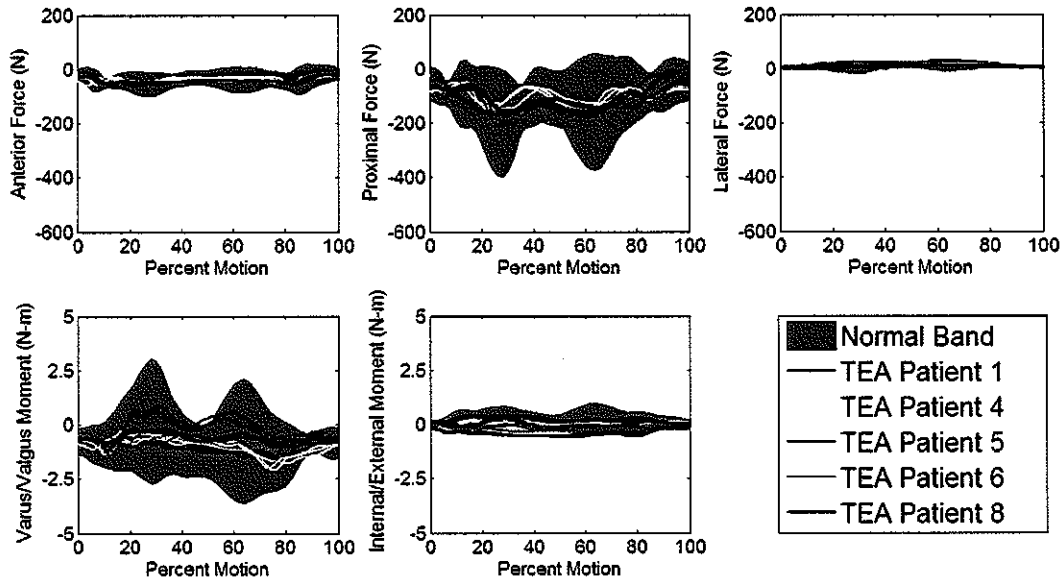

Figure 4.15: Reaction forces and moments on the elbow moving an object from a shelf on the subject's affected (or dominant) side to a shelf on their unaffected side (1 lb hand load)

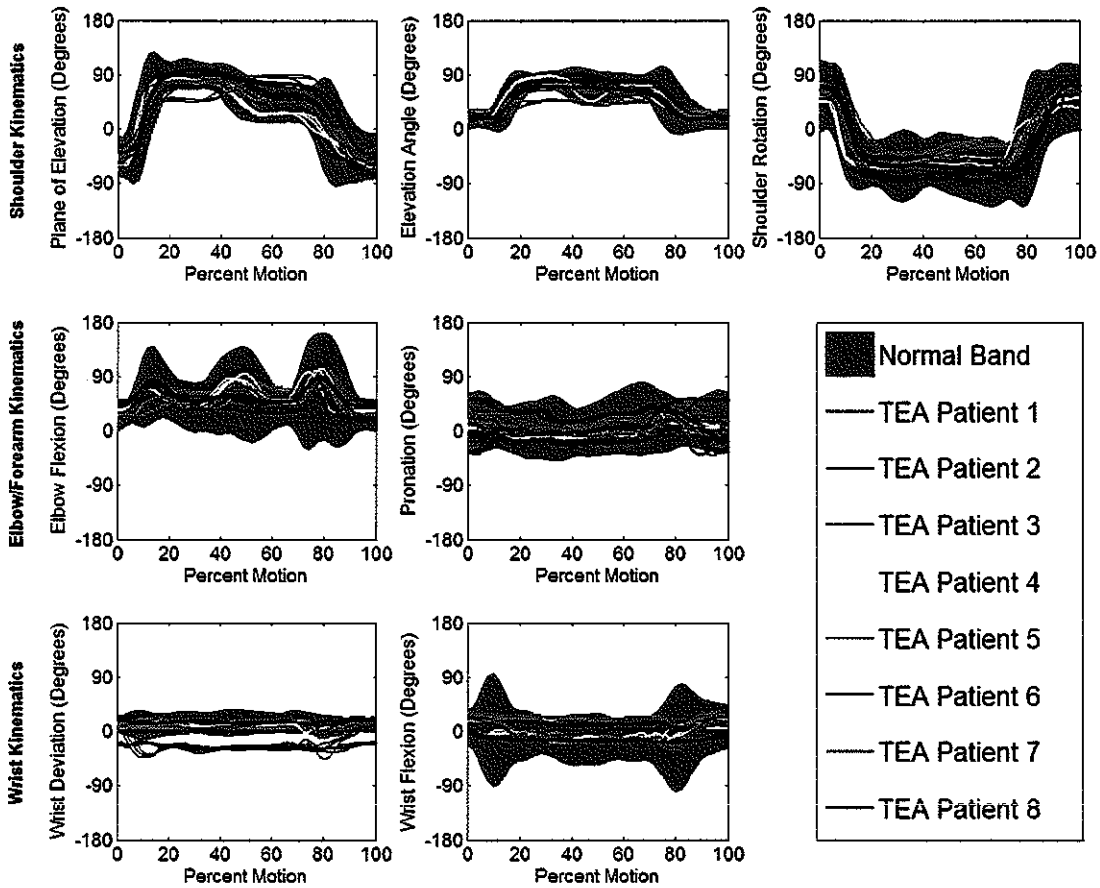

Figure 4.16: Joint angle curves while moving an object from a shelf on the subject's unaffected side to a shelf on their affected side (1 lb hand load)

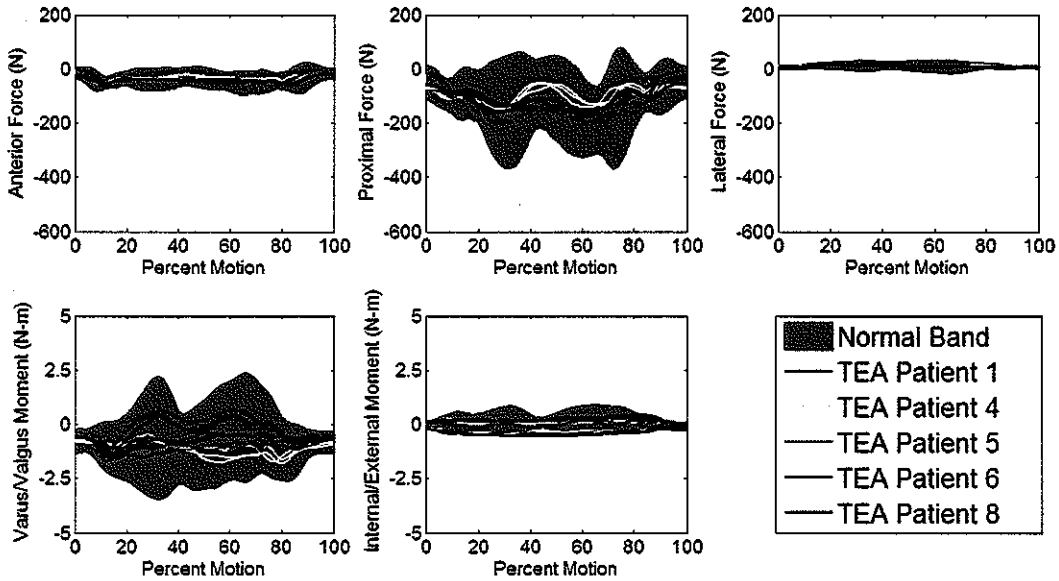

Figure 4.17: Reaction forces and moments on the elbow while moving an object from a shelf on the subject's unaffected side to a shelf on their affected side (1 lb hand load)

4.4 Discussion

In this study we determined the 95% prediction bands associated with both the kinematics and the joint loading of normal subjects performing multiple activities of daily living. We also investigated whether significant differences occur between the joint angle and loading curves demonstrated by normal subjects and those demonstrated by total elbow replacement patients.

From our data we were able to determine that, even among normal subjects, there is substantial variability in the kinematics of a particular motion. The large widths of the 95% prediction bands at many points during each of the tasks indicate that normal subjects may choose to perform tasks in such a way that the joint angles at a specific point throughout the motion may be highly dissimilar even for identical tasks.

However, although substantial variability does exist within the normal subjects, that variability is generally not sufficient to completely explain the kinematics of the total elbow patients. The task for which the total elbow patient data was most explainable using the normal subject population occurred when the participants were moving a weighted bottle from their unaffected side to their affected side, with 25% of the trials' kinematics and 33% of the trials' loading curves falling within the normal subject prediction bands. All other tasks showed less agreement between normal subjects and total elbow patients and some exhibited no agreement at all However, while the kinematics and joint loading during a trial performed by a total elbow patient could seldom be explained using the normal subject data, it is important to note that, in most cases, the discrepancy between the unexplained trials and the normal bands occurs only locally during the motion and, when a discrepancy does occur, the magnitude of the difference between the total elbow patient data and the normal subject band is

generally small. This is especially true of the difference between the joint loading during the normal subject and total elbow patient tasks. Thus, while the data gathered using normal subjects do not completely explain the total elbow patients' data, they do, in the case of the loading, offer a reasonable estimate of what the forces and moments across a replaced joint might be.

There are a few points that must be considered when interpreting the data in this study. First, the number of subjects tested for the both the normal subjects and the total elbow patients is relatively small with only eight of each group being tested. This is further magnified by the necessity to exclude three of the total elbow patients when analyzing the loading curves throughout each motion. With the addition of more subjects to either the normal or total elbow group, it is possible that some small changes in the explainable percentage of total elbow patient kinematic and kinematic data may occur. A somewhat related concern is that, within the limited set of instructions given, participants were permitted to perform the activities in whatever manner they felt most comfortable. Thus, some of the discrepancy between normal subjects and total elbow patients that was observed may be a function of personal preference rather than of the presence of an implant.

Also, the subset of upper extremity tasks we considered was limited. Other studies have examined assisted sitting, assisted sit-to-stand activities, lifting a suitcase, brushing the teeth, combing the hair and other, less conventional, tasks [8, 63, 68]. However, some of these tasks, such as assisted stand-to-sit, assisted sit-to-stand, and suitcase lifting place loads on the elbow that are many times the magnitude of the loads across the joint in the tasks we examined. These loads would substantially exceed levels corresponding to the restrictions generally placed on total elbow patients.

In addition, we consider it unlikely that anyone with a degenerative or traumatic condition severe enough to require total elbow replacement would naturally use their implanted upper extremity to assist in a sit-to-stand or stand-to-sit task or to lift a suitcase. Tasks requiring overhead motion, and shoulder elevation greater than 90 degrees, are also unlikely to be performed, because patients with degenerative elbows may also experience associated degenerative changes at the shoulder. Other activities, such a tooth brushing, are fundamentally similar to what has been has been examined here. Thus we believe that the set of activities we examined sufficiently fills the range of reasonable tasks that a total elbow patient would perform. Furthermore, Chapter 3 illustrates the importance of examining the tasks we have chosen, since it suggests that, even at the level of joint loading caused by these tasks, the risk of implant failure may be increased.

In summary, although normal subjects have been shown to perform activities in a different manner than total elbow patients, we see that the movements used by normal subjects to accomplish these activities induce forces at the elbow that are similar to the forces exerted on the elbows of total elbow replacement patients. Thus, while it is incorrect to think that the kinematics and joint loading resulting from the evaluation of a normal subject are a direct surrogate for the kinematics and joint loading of a total elbow replacement patient, the loading on the elbow joint is likely similar enough in most cases that the normal subject data may be used as an acceptable approximation to describe the mechanical environment of a total elbow replacement.

Chapter 5

Effects of Implant Position, Fixation, and Bone Modulus on the Structural Behavior of the Humeral Component of the Coonrad-Morrey Total Elbow Replacement

5.1 Introduction

Our previous studies have demonstrated that increases in articular contact forces may be responsible for increased wear of the bushings at the humeral component of a contemporary Coonrad-Morrey total elbow replacement. We have argued that this increased wear may be responsible for the generation of polyethylene wear debris which has, in other joints, been shown to contribute to aseptic loosening of the implant component. We concluded, therefore, that implanting the humeral component during surgery in positions that would minimize the contact forces across the joint may be advantageous in limiting articular surface wear and improving the longevity of the implant.

Our previously analyses, however, did not take into account the structural response of the overall humerus-implant system to both the loads being applied to the implant and to changes in the position of the implant and cement mantle within the bone itself. While polyethylene wear debris may be a contributor to aseptic loosening of the implant, it is certainly not the only factor that may contribute. Certain loading conditions or configurations of the humerus-implant system may engender stresses or strains in the cement mantle or bone that cause material failure of either and lead again to loosening of the implant through mechanisms different from the one we had previously considered. To gain insight into this mechanism of failure, it is necessary to examine not only the changes in the joint loading that occur during motion, but also the structural response of the system on a more detailed level.

Previous investigators have attempted to investigate the structural response of the bone-implant system through the use of finite element analysis. Goel et al. [22] examined the von Mises stress distributions arising in the humerus, cement mantle, and an early generation Coonrad elbow prosthesis under various loading regimes. Looking at a 1 N superior, 1 N posterior, and 1 N-cm axial torque, they determined that torsional loading of the implant increased the stresses in the trabecular bone the most over those present in the natural condition. Posterior loading of the joint, however, caused the largest magnitude trabecular and cortical stresses to appear in both the natural and implanted cases. Isotropic, homogeneous bone material properties were used in this study, however, and contact between all model components was displacement compatible and bonded.

Herren et al. [25] also used finite element analysis to investigate the effect of adding an anterior flange to a GSB III (Zimmer, Inc. Warsaw, IN) semiconstrained prosthesis

on the von Mises stresses in the implant. They examined the response of the implant under a 100 N posteriorly directed force, a 0.01 N-m axial moment, and under two cases in which forces applied were derived using a biomechanical model of the elbow to simulate the reaction forces at the joint at 90 and 120 degrees of elbow flexion. The presence of an anterior flange was found to lessen the stresses in the implant in the region of the implant stem thought to be adjacent to the area of clinically observed loosening. As in Goel et al., homogeneous trabecular, cortical, and cement material properties were applied. The interfaces between bone and cement and cement and implant were again modeled as being completely bonded. Both of these prior studies used linear finite element analysis only. However, while the linear solutions obtained using these simple loading cases are subject to superposition, the set of loads applied do not contain all components of load present during daily activities. In addition, linear finite element analysis ignores the effect of both geometric and contact nonlinearities on the solution.

Our objective in this study was to update and extend the work done by Goel, Herren, and their colleagues. We sought to determine the structural response of the humerus and cement mantle using a popular, current total elbow replacement, the Coonrad-Morrey, under loading conditions which could realistically be expected to occur in general activities of daily living. We investigated these responses as a function of humeral implant position, fixation of the implant, and the elastic moduli of the surrounding bone. Rather than looking at von Mises stress in the system, we were more concerned with minimum principal compressive strains in the bone and maximum principal tensile stresses in the cement, which are associated with the failure of these materials [41, 56]. We also sought to determine the manner in which loads were transferred from the implant to the surrounding bone under these loading

conditions.

5.2 Methods

We used finite element models to determine the effect of implant position, implant fixation, and surrounding bone modulus on the structural response of a humeral bone-cement-implant system. Bone geometry and density information were extracted from computed-tomography scans of the elbow. Implant geometry was constructed from surgical templates. Finite element models were created from these geometries and included 17,550 hexahedral elements and 22,448 nodes. Loads were calculated from the kinematic data of Chapter 4 using the computational model of Chapter 3. Ninety finite element analyses were run of the humeral bone-implant system. In total, ten humeral positions, three density-modulus relationships, and three interface conditions were studied

5.2.1 Geometry Creation

Humeral geometry was obtained from a single computed tomography (CT) scan of a healthy male elbow. Scans were taken at 0.4 mm intervals from approximately the mid-diaphysis of the forearm to approximately one-third of the length up the diaphysis of the humerus. The thickness of each scan was 0.4 mm. To increase the effective proximal coverage of the scans and provide adequate room for implant insertion, the axis of the existing humeral diaphysis was determined and the most proximal scan of the set was duplicated along this axis at intervals of 0.4 mm up to a total distance of 40 mm. A mask of the extended humerus was created by thresholding the bone from the soft tissue using Mimics 12 (Materialise, Leuven, Belgium) (Figure 5.1). All pixels with Hounsfield Units (HU) greater than 226 and less than 2117 were considered to be bone. Humeral bone was separated from ulnar and radial bones through region

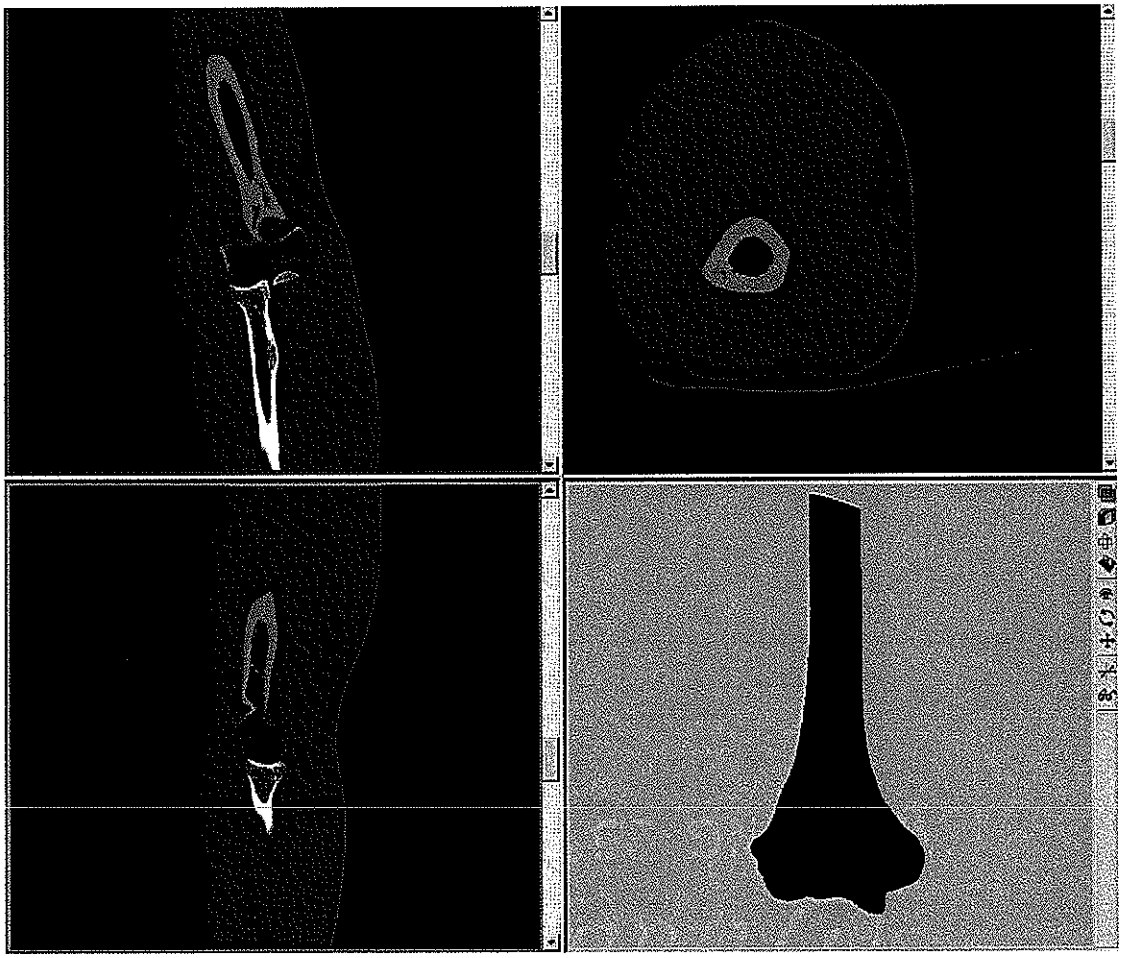

Figure 5.1: Masking and processing of humeral bone to create tessellated surface for later meshing

growing. Small inclusions in the exterior of the humeral bone mask were filled manually and boundary curves were created around the exterior surface of the bone in each scan. These boundary curves were then filled to create a mask of the entire humerus including the medullary canal. A tessellated surface representation of the exterior humerus was then imported into Studio 4.0 (Geomagic, Research Triangle Park, NC) where it was smoothed and refined to create the final non-uniform rational B-spline (NURB) surfaces used for finite element mesh projection.

Using Pro/Engineer Wildfire 3.0 (Parametric Technology Corporation, Needham, MA), a surface model of the humeral component of the Coonrad-Morrey was created

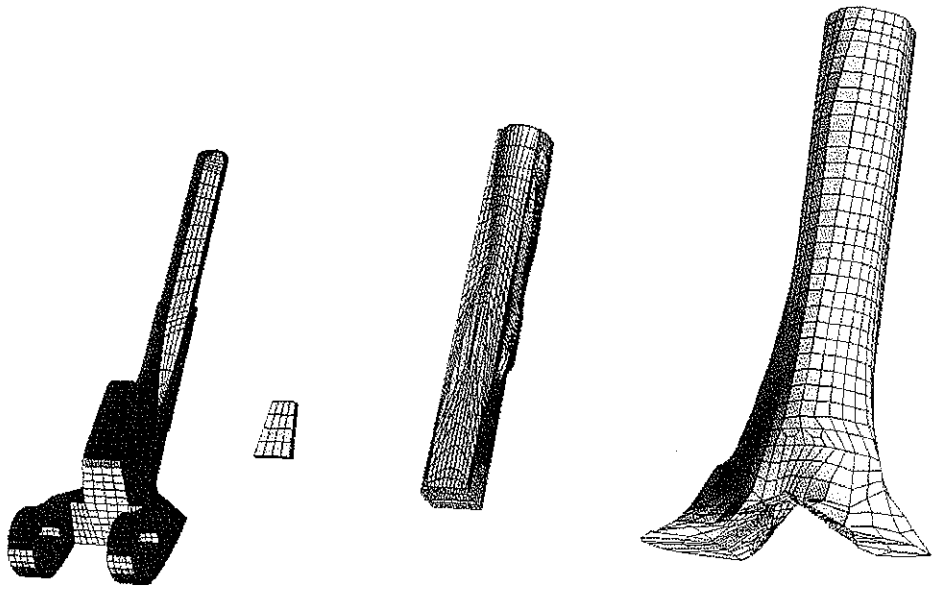

Figure 5.2: Exploded view of the finite element mesh showing the implant, graft, cement, and bone (from left to right)

from surgical templates, product brochures, and direct examination of the implant component. On the advice of clinical collaborators, the small humeral component size was chosen. The standard flange length was modeled. The shortest stem length (approximately 102 mm) was chosen to maximize the axial distance between the tip of the implant component and the fixed proximal boundary of the extended humeral bone.

5.2.2 Finite Element Mesh Creation

Finite element meshes of the humerus and the implant were created using Truegrid (XYZ Scientific Applications, Inc., Livermore, CA). Based upon published surgical techniques, cuts were made in the bone surface to accommodate the implant geometries. The distal medial and lateral humeral condyles were removed according to common surgical technique (Figure 5.2). To accommodate the implant stem a channel was made through the distal metaphyseal bone. The shape of this channel corresponded to the external geometry of the small humeral rasp used surgically. The exterior surfaces of humeral cement mantle were created from the internal surfaces of

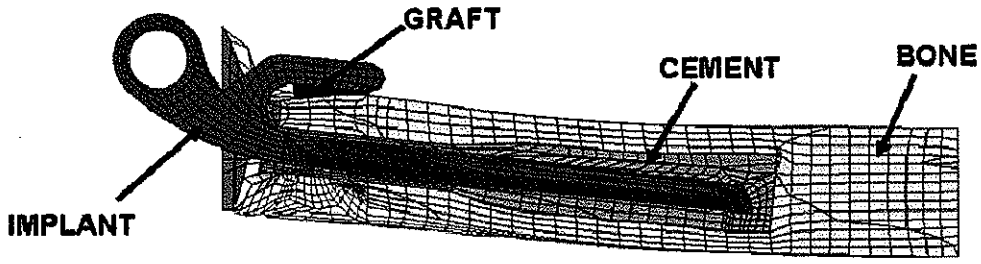

Figure 5.3: Sagittal cross-section showing the assembled finite element meshes of the humerus, implant, cement mantle, and graft material for a typical implant position

the rasp channel distally and the endosteal surface of the bone proximally. The implant stem was positioned in the distal channel such that a minimum cement thickness of 1 mm was guaranteed. To model the bone graft that is inserted underneath the flange of the implant, additional elements were created in the space between the anterior cortex of the humerus and the interior surface of the implant flange (Figure 5.3).

5.2.3 Finite Element Analyses

Material Property Assignment

Each element of the finite element mesh was assigned linear elastic, isotropic material properties with a Poisson's ratio of 0.3. The elastic moduli of the elements comprising the titanium implant were 110 GPa. The elastic moduli of all elements of the cement mantle were 2 GPa. In preliminary studies, the total load transfer through the graft was always small and varying the moduli of the graft elements from 1 MPa to 10 GPa had little effect on the load transfer or cement stresses in the humeral bone-implant system. The graft element moduli in further analyses were therefore set to 1 GPa.

To assign moduli to each element of bone, the bone finite element mesh was imported into Mimics. At each element integration point, interpolation of the Hounsfield units

of surrounding voxels that lay within the previously defined humeral mask was performed in order to determine a single Hounsfield value at that integration point. A volume weighted averaging of the integration points of an element was then performed to determine a single Hounsfield value for each element. Hounsfield units in a region of bone have been shown to be linearly related to the density of the bone in that region. Furthermore, many relationships have been proposed to relate bone density to elastic modulus. Due to the scarcity of published data on both wet and dry apparent densities and elastic modulus distribution in the distal humerus, it was necessary to first determine a linear relationship between Hounsfield units and quantitative computed tomography (QCT) humeral density (BMD) on which data do exist. Two data points were needed to create this relationship. The first datum point was taken in the cancellous bone of the distal humeral metaphysis. To correlate cancellous density with Hounsfield number in this region, the scan slice with the largest bone cross-sectional area was identified. The trabecular region 2.5 mm around this slice in both the proximal and distal directions was isolated and the Hounsfield units in the inner 50% of this region were averaged to determine a representative value for the distal humerus. This value was then correlated to the mean pQCT density of 0.317 g/cm^3 for the same region as determined by Diederichs [19]. Peripheral QCT density was converted to QCT density using the relationship of Jiang [32]. The second datum point was taken in the cortical bone of the humeral diaphysis. The average Hounsfield number in a representative region of the humeral shaft was correlated to a mean QCT density of 1169 mg/cm^3 as determined by Kaneko [34]. A linear regression was fit to these two points and the relationship between HU and QCT was determined. The QCT density of each element was converted into an elemental ash density using the relationships of Keyak and Taneko [34, 39]:

Cancellous bone: $\rho_{ash} = 0.00106*\rho_{QCT} + 0.0389$

Cortical bone: $\rho_{ash} = 0.000290*\rho_{QCT} + 0.806$

Since no data exist describing the relationship between modulus and density specifically at the site of the human distal humerus, a relationship derived by Morgan [55] using data from multiple regions of cancellous bone (0-0.38 g/cm^3) was used. This relationship was expressed in terms of ash density again by using the work of Keyak [39]. For cortical bone (0.38-1.2 g/cm^3), a linear relation was assumed between ash density and modulus. The elastic modulus of cortical bone was taken from Kaneko [34]. In order to account for the error associated with these relationships (or values), the 95% published confidence intervals (or 2*standard deviations) were used to determine upper and lower bound curves for the density-modulus relationship. Thus, the upper bound curve was described by the equation:

$$E_{UB} = \begin{cases} 10.55*(1.79*\rho_{ash}+0.0019)^{1.72} & 0.0\ g/cm^3 \leq \rho_{ash} \leq 0.38\ g/cm^3 \\ 26.1489*\rho_{ash}-3.4644 & 0.38\ g/cm^3 < \rho_{ash} \leq 1.2\ g/cm^3 \end{cases}$$

and the lower bound curve was described by:

$$E_{LB} = \begin{cases} 7.54*(1.79*\rho_{ash}+0.0019)^{1.94} & 0.0\ g/cm^3 \leq \rho_{ash} \leq 0.38\ g/cm^3 \\ 20.0164*\rho_{ash}-3.2605 & 0.38\ g/cm^3 < \rho_{ash} \leq 1.2\ g/cm^3 \end{cases}$$

For each finite element analysis run in this study, the specific relationship between density and modulus was taken as a weighted average of the upper and lower elastic modulus bounds, such that:

$$E = \alpha * E_{LB} + (1-\alpha) * E_{UB}$$

In this study, α values of 0, 0.5, and 1 were used (Figure 5.4). This resulted in bone modulus distributions as seen in Figure 5.5. While these distributions may not completely encompass the range of bone moduli possible in diseased or degenerating bone, they do allow us to assess the sensitivity of each of out output measures to variations in modulus.

Interface Modeling

The cement-bone interface was always modeled as bonded (displacement compatible). Direct interactions between the implant and either the bone or the graft were modeled as non-tension interfaces with a coefficient of friction of 0.8. All of these interactions occurred at locations at which the implant was beaded. The interface between the non-beaded, smooth surfaces of the humeral component and the cement layer were

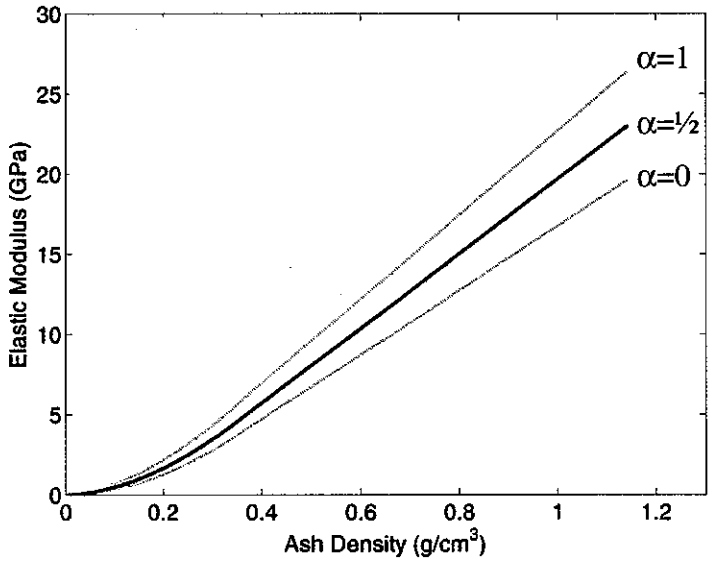

Figure 5.4: Upper (α=1), middle (α=0.5), and lower (α=0) bound modulus relationships used to assign elastic moduli to elements of humeral mesh

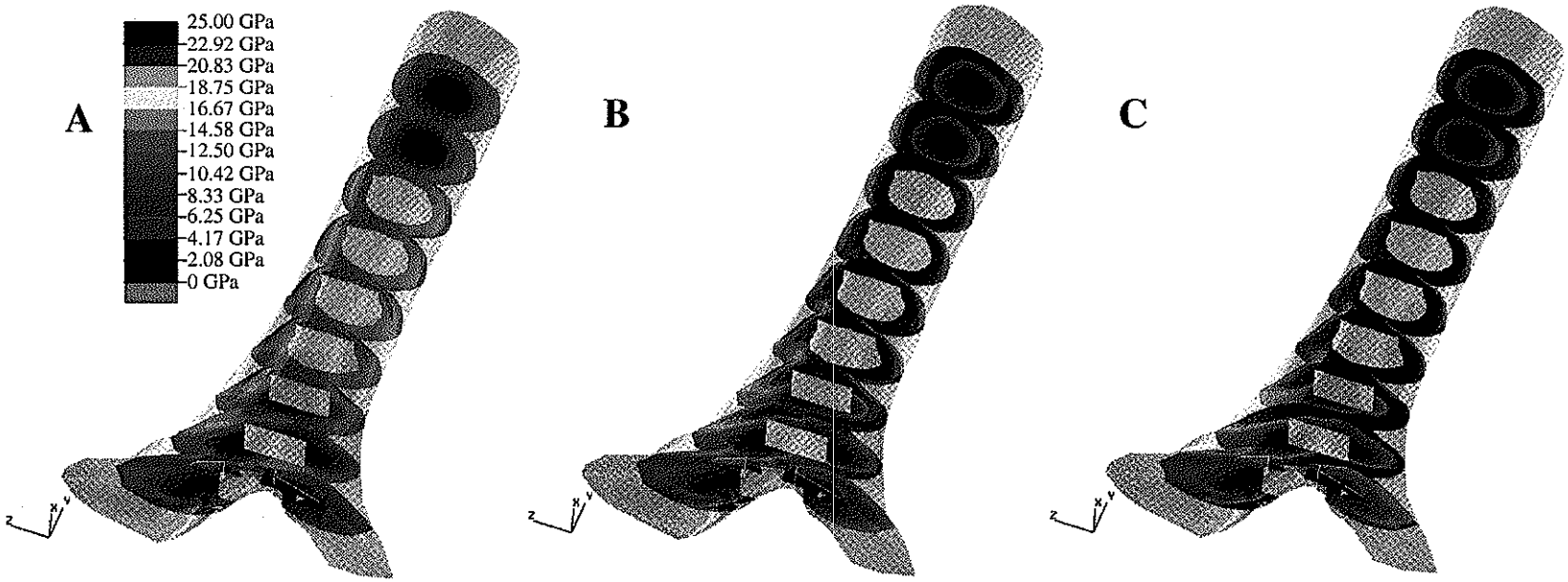

Figure 5.5: Elastic modulus distributions in the humerus for the case of A) α=0, B) α=0.5, and C) α=1

Table 5.1: Summary of Analysis Boundary Conditions

BC	Boundary Condition	Description
0	Unsupported	Cement/bead interface: friction, μ=0.8 No chevron/bone contact No flange base/bone contact No posterior distal implant/cement contact No flange/graft contact
0.5	Frictional	Cement/bead interface: friction, μ=0.8
1	Bonded	Cement/bead interface: Displacement compatible

modeled as a non-tension interface with a friction coefficient of 0.3 [52]. The interface between the beaded implant surface and the cement layer was varied as specified in Table 5.1.

In the first case (BC=0) examined, the implant had substantially less support distally. There was no contact between the undersurface of the flange and the graft, essentially removing the flange from the model. Also, no contact existed between the flared distal implant chevron and the remnants of distal humeral condyles. The base of the flange also did not contact bone in these analyses. The distal, posterior contact between the implant and cement layer was additionally removed. The interaction between the beaded surface of the implant and the cement was modeled as a non-tension interface with a coefficient of friction of 0.8. In the second case (BC=0.5), contact between all opposing surfaces was restored. Again, the interaction between the beaded surface of the implant and the cement was modeled as a non-tension interface with a coefficient of friction of 0.8. The third interface case (BC=1) also retained contact of all opposing surfaces but in this case the interaction between the beaded surface of the implant and the cement was modeled as bonded (displacement compatible).

Implant Positioning

Ten humeral implant positions were examined. Humeral positions were defined by a set of four parameters: proximal-distal (PD) and anterior-proximal (AP) displacements of the component from the natural joint center, and internal-external (IE) and varus-valgus (VV) rotations of the implant from the natural axis orientation (Figure 3.1). The natural joint center in these models was taken as the center of the cylinder fit to the smallest diameter of the trochlear sulcus of the natural elbow. Humeral positions were chosen to best fill the parameter space in which each parameter was permitted to vary from -5 to +5. The extent of the space was further limited by only choosing feasible positions in which the proximal tip of the implant did not violate the endosteal surface of the midshaft humerus and in which the interior surface of the implant flange did not violate the anterior surface of the humeral cortex. Each implant position and the associated implant translation and rotation is described in Table 5.2

Table 5.2: Implant Displacement from Natural Axis

Humeral Implant Position	Varus(+)/ Valgus(-) Rotation (°)	Internal(+)/ External(-) Rotation (°)	Anterior(+)/ Posterior(-) Translation (mm)	Proximal(+)/ Distal(-) Translation (mm)
1	1.5	0	4.8	2.5
2	2.3	-2.5	4.5	0.6
3	1.9	-3.8	4.1	-0.6
4	1.7	-0.6	3.9	-4.2
5	1.3	0.6	4.7	-3
6	2.2	-1.6	4.3	3.4
7	2.5	-2.8	4.8	-2.8
8	2.7	-3.3	3.8	1.3
9	2.1	-3.9	4.6	-3.6
10	2	-1.1	5	0.5

Boundary Conditions

To determine the loads applied to the finite element models, kinematic motion analysis

data were collected from eight total elbow patients performing various activities of daily living as described in Chapter 4. As in the previous chapter, patient data were screened to eliminate total elbow patients who were not able to perform the motions as directed. For the remaining set of patients, the kinematic data were input into the computational model of Chapter 2 to calculate the reaction forces and moments at the elbow by minimizing the sum of the muscle stresses cubed. Using known implant geometries, contact forces on the implant were calculated. Subject 4 was identified as producing the maximum contact forces on the implant while performing the feeding activity with the humerus held at 90 degrees of abduction. At the fourth of six trials for this motion, we identified the point of maximum contact force throughout the trial and extracted the joint reaction forces and moments at that point. These joint forces and moments were identified and calculated for each humeral implant position and were applied to the finite element models (Table 5.3). Calculated moments about the lateral-medial axis were always less then 1 N-mm and thus were set to zero in all finite element analyses. Forces and moments were applied to a reference node at the center

Table 5.3: Input Joint Reaction Loads

Humeral Implant Position	Anterior(+)/ Posterior(-) Reaction Force (N)	Proximal(+)/ Distal(-) Reaction Force (N)	Lateral(+)/ Medial Reaction Force (N)	Varus(+)/ Valgus(-) Reaction Moment (Nmm)	Internal(+)/ External(-) Reaction Moment (Nmm)
1	-39	-16	-21	-1881	1954
2	-35	-18	-27	-1781	1835
3	-33	-20	-27	-1719	1777
4	-37	-18	-22	-1867	1914
5	-38	-17	-19	-1904	1970
6	-36	-16	-25	-1826	1890
7	-33	-18	-27	-1771	1807
8	-33	-17	-29	-1755	1810
9	-32	-20	-27	-1715	1752
10	-37	-17	-24	-1840	1897

of the implant articulation and were transmitted to the implant through the use of a rigid analytical cylindrical surface that was displacement compatible with the internal diameter on the humeral component into which the articular bushings insert. To fully constrain the finite element model and eliminate rigid body modes, the nodes on the proximal cross-section of the humeral diaphysis were fixed.

5.2.4 Data Analysis

Ninety finite element analyses were attempted of the humeral bone-implant system. In total, ten humeral positions, three density-modulus relationships, and three interface conditions were studied. As the objective of these analyses was to obtain enough data in order to determine an approximation to the overall behavior of the bone implant system, not every analysis that was run was required. While having every analysis successfully complete in order to gain as much data as possible on which to base conclusions is preferable, as long as the successful analyses covered the feasible parameter space well, the completion of every finite element analysis was not necessary. Thus, analyses which did not complete (did not converge) were not reattempted. Out of 90 total finite element analyses run, 70 were completed and used for further data analysis (Table 5.4).

The loads on each node of the contact surfaces of the humerus, cement, implant, and graft were calculated from the components of stress at each node, nodal displacement information, and knowledge of the shape functions for isoparametric, hexahedral elements. To analyze load transfer, surface loading was evaluated for five sections across the humeral component (Figure 5.6). The distal stem encompassed the entire stem that lie distal to the proximal tip of the flange. The proximal stem encompassed

Table 5.4 Parameter Space of Converged Finite Element Analysis

Humeral Position	α	BC		Humeral Position	α	BC
1	0	0		6	0	1
1	0	0.5		6	0.5	1
1	0	1		6	1	0
1	0.5	0		6	1	0.5
1	0.5	1		6	1	1
1	1	0		7	0	0
1	1	0.5		7	0	0.5
1	1	1		7	0	1
2	0	0.5		7	0.5	0.5
2	0	1		7	0.5	1
2	0.5	0		7	1	0
2	0.5	1		7	1	0.5
2	1	0		7	1	1
2	1	0.5		8	0	0
2	1	1		8	0	0.5
3	0	0		8	0	1
3	0.5	0		8	0.5	0
3	1	0		8	0.5	0.5
4	0	0.5		8	0.5	1
4	0	1		8	1	0.5
4	0.5	0		8	1	1
4	0.5	0.5		9	0	0.5
4	0.5	1		9	0	1
4	1	0		9	0.5	0.5
4	1	0.5		9	0.5	1
4	1	1		9	1	0
5	0	0		9	1	0.5
5	0	0.5		9	1	1
5	0	1		10	0	0.5
5	0.5	0		10	0	1
5	0.5	1		10	0.5	0
5	1	0		10	0.5	0.5
5	1	0.5		10	0.5	1
5	1	1		10	1	0.5
6	0	0		10	1	1

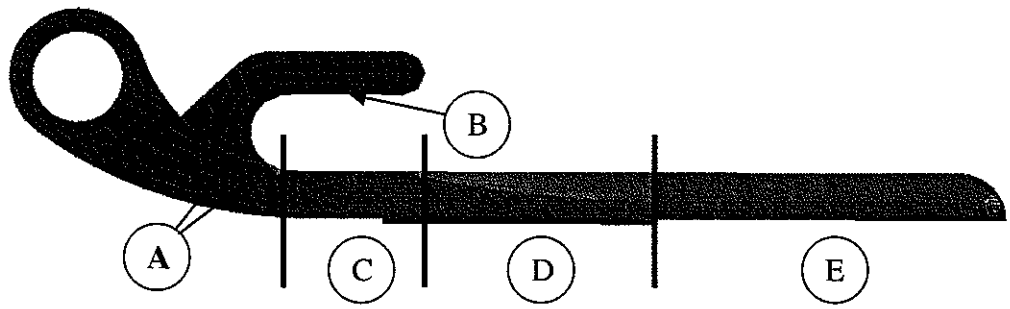

Figure 5.6: :Five sections across which load transfer was calculated: A) chevron and flange base, B) flange, C) distal stem, D) middle stem, E) proximal stem

the entire stem that was proximal to the most proximal extent of the beaded surfaces, and the middle stem was the section between the other two. Net load transfer in each section was calculated. In the natural joint, all load transfer to the bone occurs distally. To determine which parameters were most able to replicate the natural condition, multiple linear regression models were used to determine which parameters had the largest effect on load transfer across the proximal implant stem away from the joint. These regression models included only first order terms. After determining which parameters had the most effect on proximal load transfer, one-way analyses of variance were performed on each parameter to determine which of those parameters significantly affected load transfer. Cumulative and nodal load transfers were examined for parameters identified as significant. When examining the cumulative load transfer to the bone, each load transfer curve was smoothed using locally weighted least squares (lowess) smoothing with a span equal to 5% of the dataset. This smoothing was performed in order to remove local discontinuities in load transfer that resulted from mesh discretization and to aid visualization.

Stress in the cement layer was also examined. Similar to the load transfer analysis, the cement layer was separated into three sections that corresponded to the stem sections established when analyzing load transfer (Figure 5.7). Thus the distal cement layer

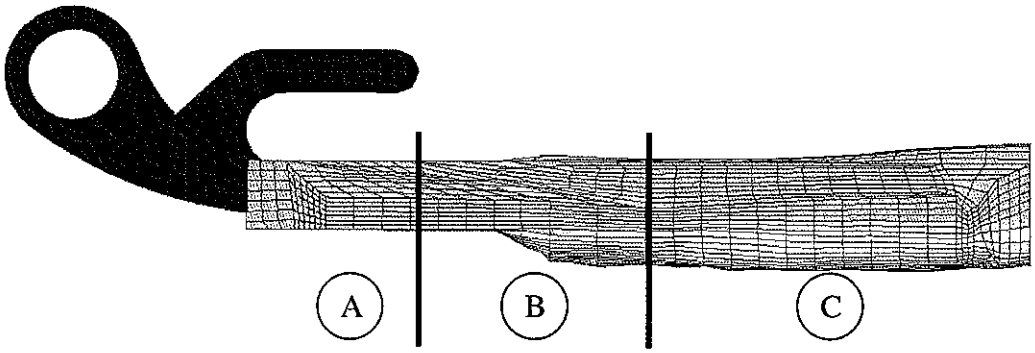

Figure 5.7: Three regions in which cement stresses were calculated: A) distal cement, B) middle cement, C) proximal cement

was comprised of all cement elements that lie solely to the outside of the distal stem. The proximal cement layer consisted of all cement elements that lie solely outside the proximal stem, and the middle cement layer consisted of the elements between the other two sections. For each section, the volume-averaged maximum principal stress in the mostly highly stressed 5% of that section's volume was calculated. This measure was chosen to minimize the effects that mesh discretization and suboptimal element shape may have on the values of peak stresses calculated in regions of complex geometry. As with load transfer, multiple linear regression models were used to determine which parameters had the largest effect on cement stresses. One-way analyses of variance were used to determine which of these effects were significant.

5.3 Results

5.3.1 Bone Strains

For all variations in humeral component position, boundary interface condition, and density-elastic modulus relationship, the minimum principal compressive strain in the bone never reached, 0.7%, the published yield value for trabecular bone [56]. Minimum principal strains in the distal bone had the greatest magnitudes for cases involving chevron and flange contact (BC=0.5, BC=1) (Figures 5.8-5.10)

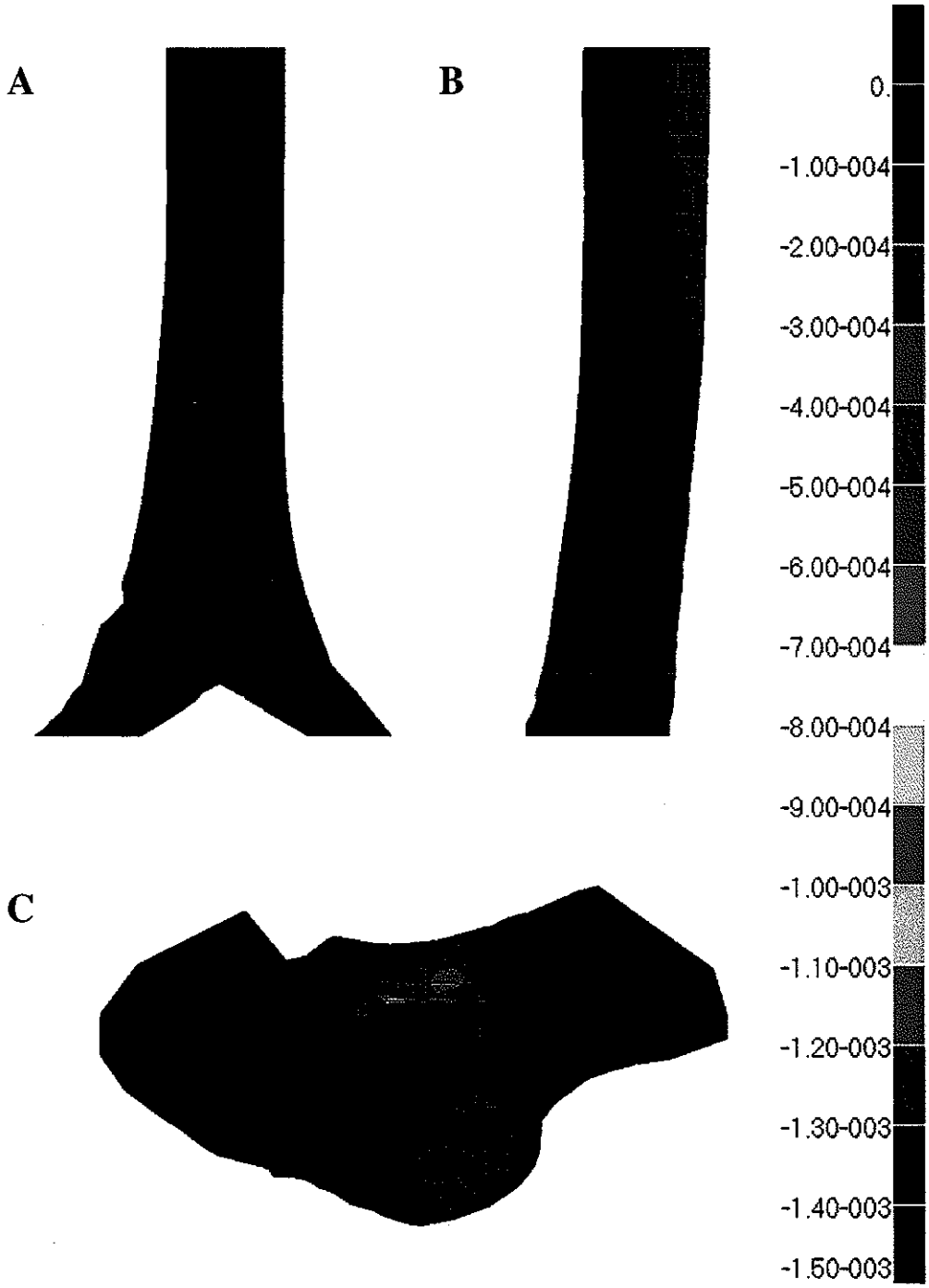

Figure 5.8: Minimum principal strains in the bone with the humerus in position 10, BC=0 and α=0.5. A) Anterior to posterior view, B) Medial to lateral view, C) Distal to proximal view

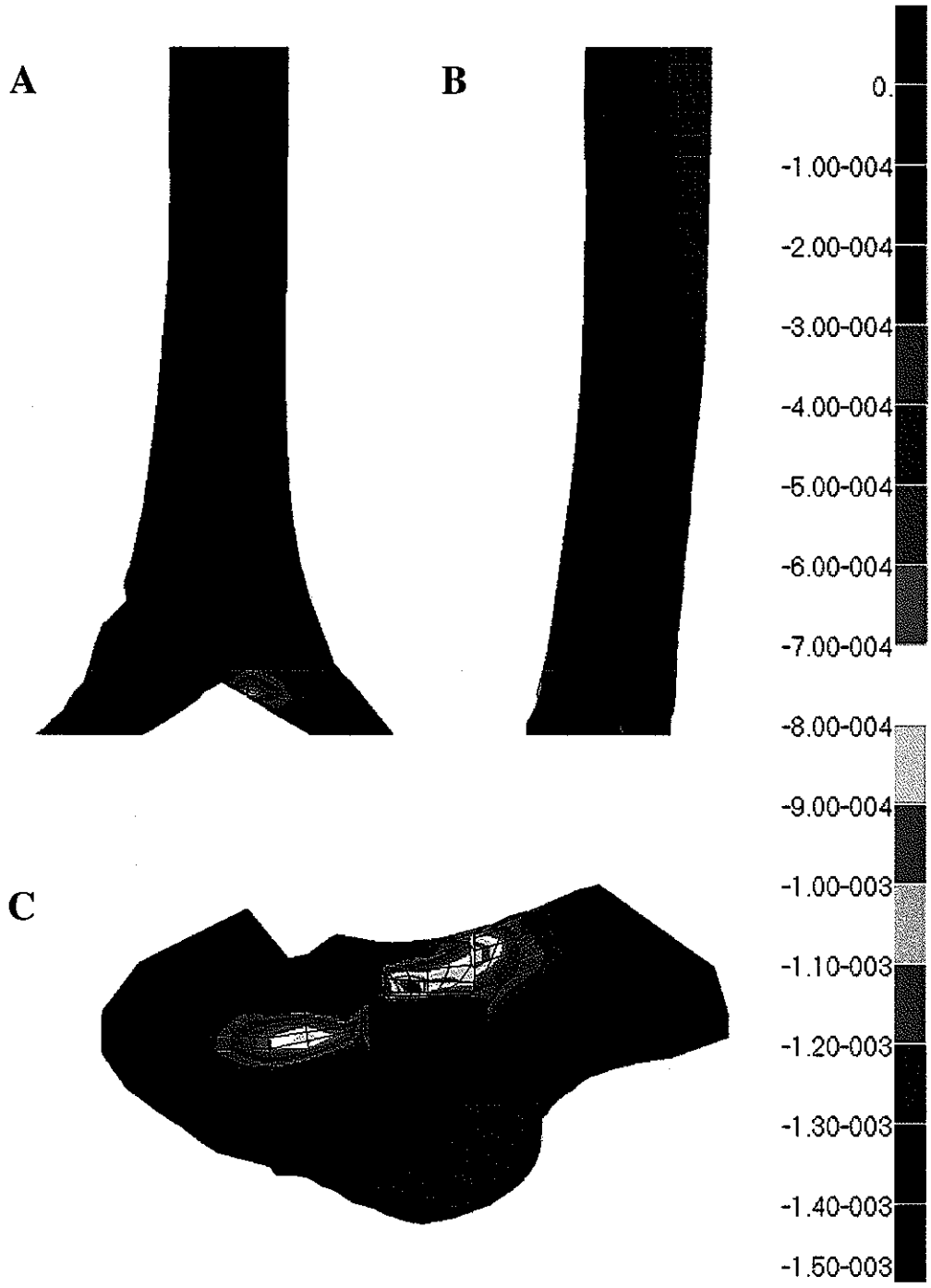

Figure 5.9: Minimum principal strains in the bone with the humerus in position 10, BC=0.5 and α=0.5. A) Anterior to posterior view, B) Medial to lateral view, C) Distal to proximal view

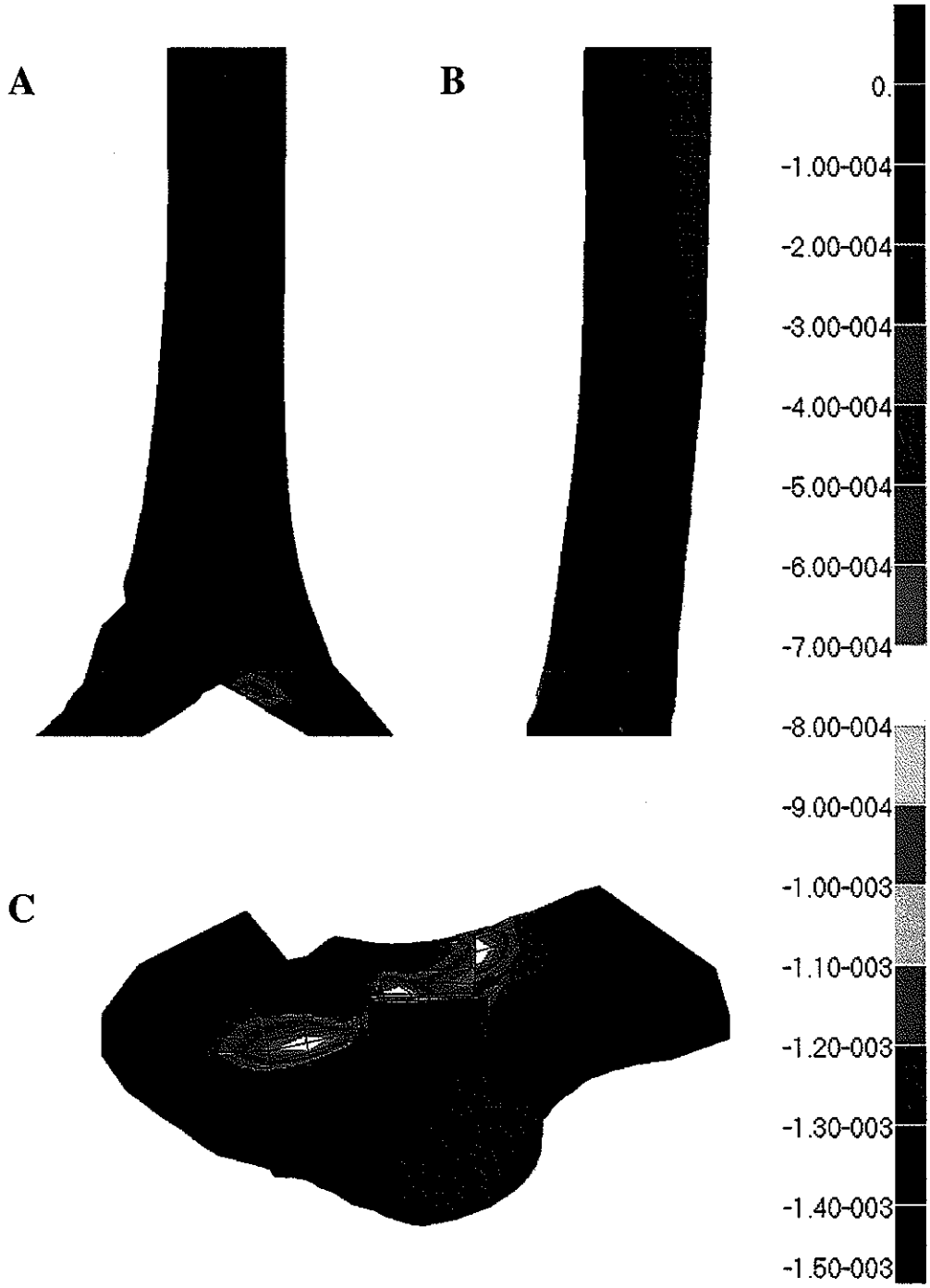

Figure 5.10: Minimum principal strains in the bone with the humerus in position 10, BC=1 and α=0.5. A) Anterior to posterior view, B) Medial to lateral view, C) Distal to proximal view

5.3.2 Load Transfer

The force transferred across the proximal stem of the implant was most sensitive to the interface boundary condition (BC) and density-modulus weighting factor (α) (Table 5.5). The coefficients of the response with respect to these two input parameters were -7.78 and -2.75, respectively.

Table 5.5: Coefficients of the Linear Regression of Proximal Stem Force

$F_{PROX\_STEM} = \beta_1*AP + \beta_2*PD + \beta_3 + VV + \beta_4*IE + \beta_5*\alpha + \beta_6*BC + \beta_7$.							
	β_1	β_2	β_3	β_4	β_5	β_6	β_7
Proximal Stem Force	1.82	-0.48	2.36	0.94	-2.75	-7.78	9.04

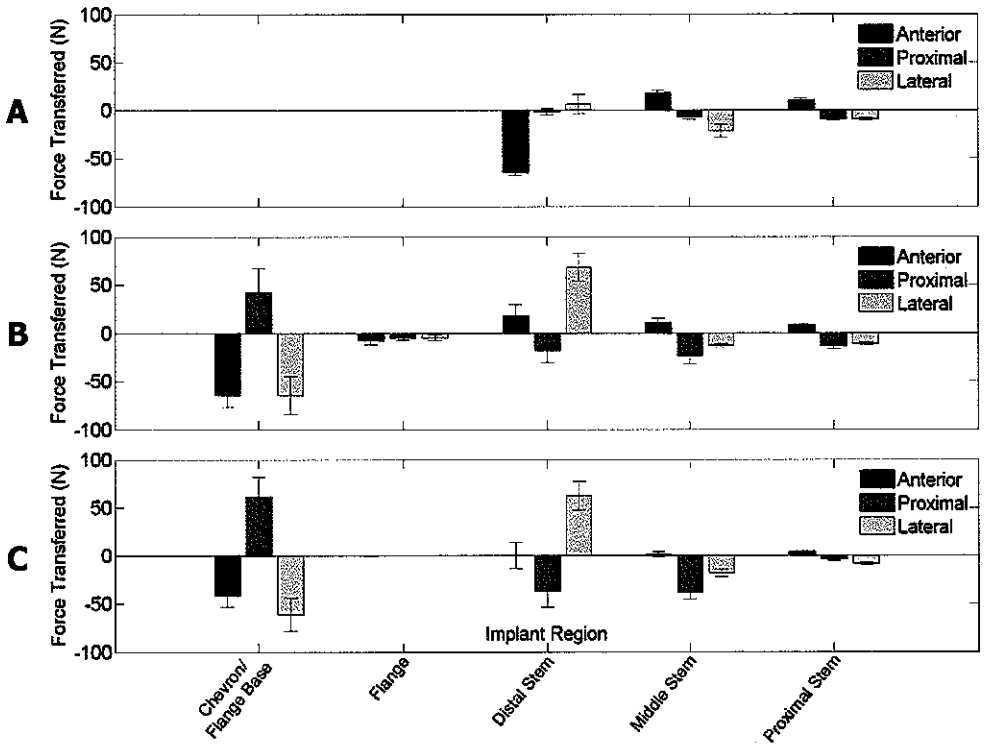

Figure 5.11: Net load transfer across five defined sections of the humeral component for the A) Unsupported (BC=0), B) Frictional (BC=0.5), and C) Bonded (BC=1) interface boundary conditions.

Of the two parameters to which the force transferred across the proximal stem was most sensitive, only the effect of interface boundary condition (BC) was found to be significant ($p<0.001$). The effect of density-modulus relationship weighting factor (α) was not ($p=0.07$).

The interior surface of the flange base as well as the proximal surface of the distal chevron of the implant were shown to be areas of increased load transfer in analyses (BC=0.5, 1) where contact between these areas and the underlying humeral bone was

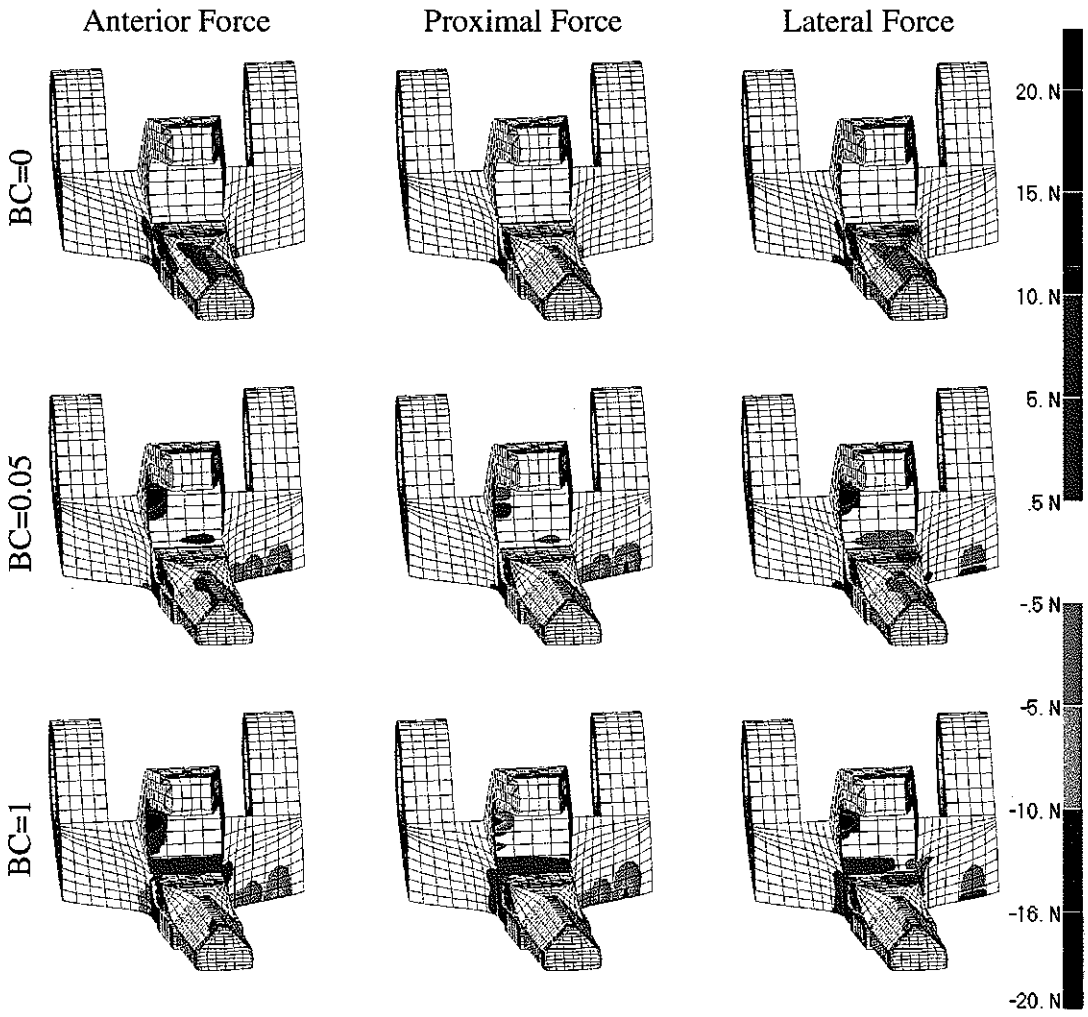

Figure 5.12: Anterior, proximal, and lateral forces (N) on the humeral component for the unsupported (BC=0), frictional (BC=0.5), and bonded (BC=1) interface conditions with the humerus in position 10 and $\alpha=0.5$.

included (Figure 5.11). For analysis in which these contact surfaces were removed (BC=0), load transfer from the implant to the bone occurred gradually along the stem. This can be seen in both the nodal loads applied to the exterior surface of the implant (Figure 5.12) and in the nodal loads applied to the exterior surface of the bone (Figure 5.13).

These areas of increased load transfer may be also be viewed by examining how the cumulative forces and the moments in the bone change as the distance from the

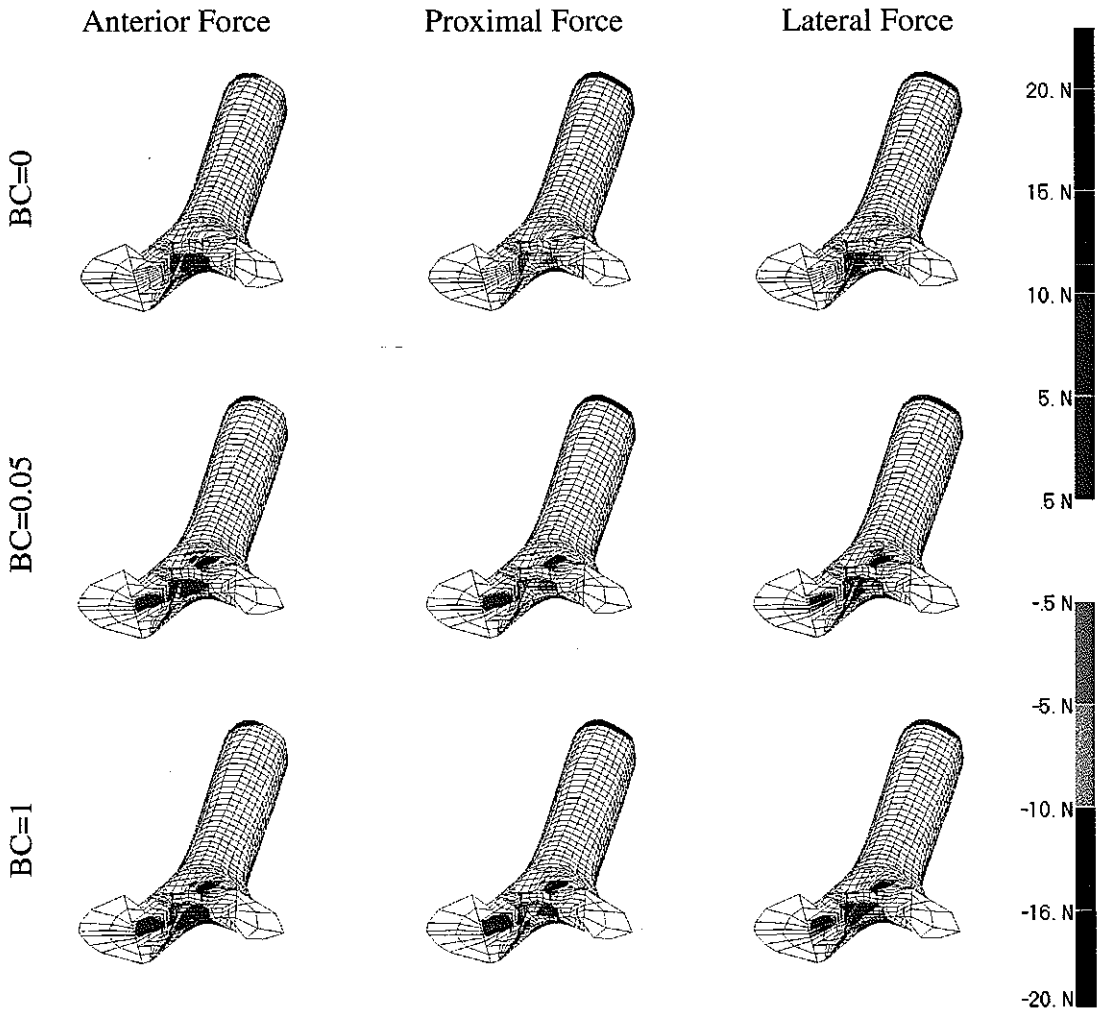

Figure 5.13: Anterior, proximal, and lateral forces (N) on the bone for the unsupported (BC=0), frictional (BC=0.5), and bonded (BC=1) interface conditions with the humerus in position 10 and α=0.5.

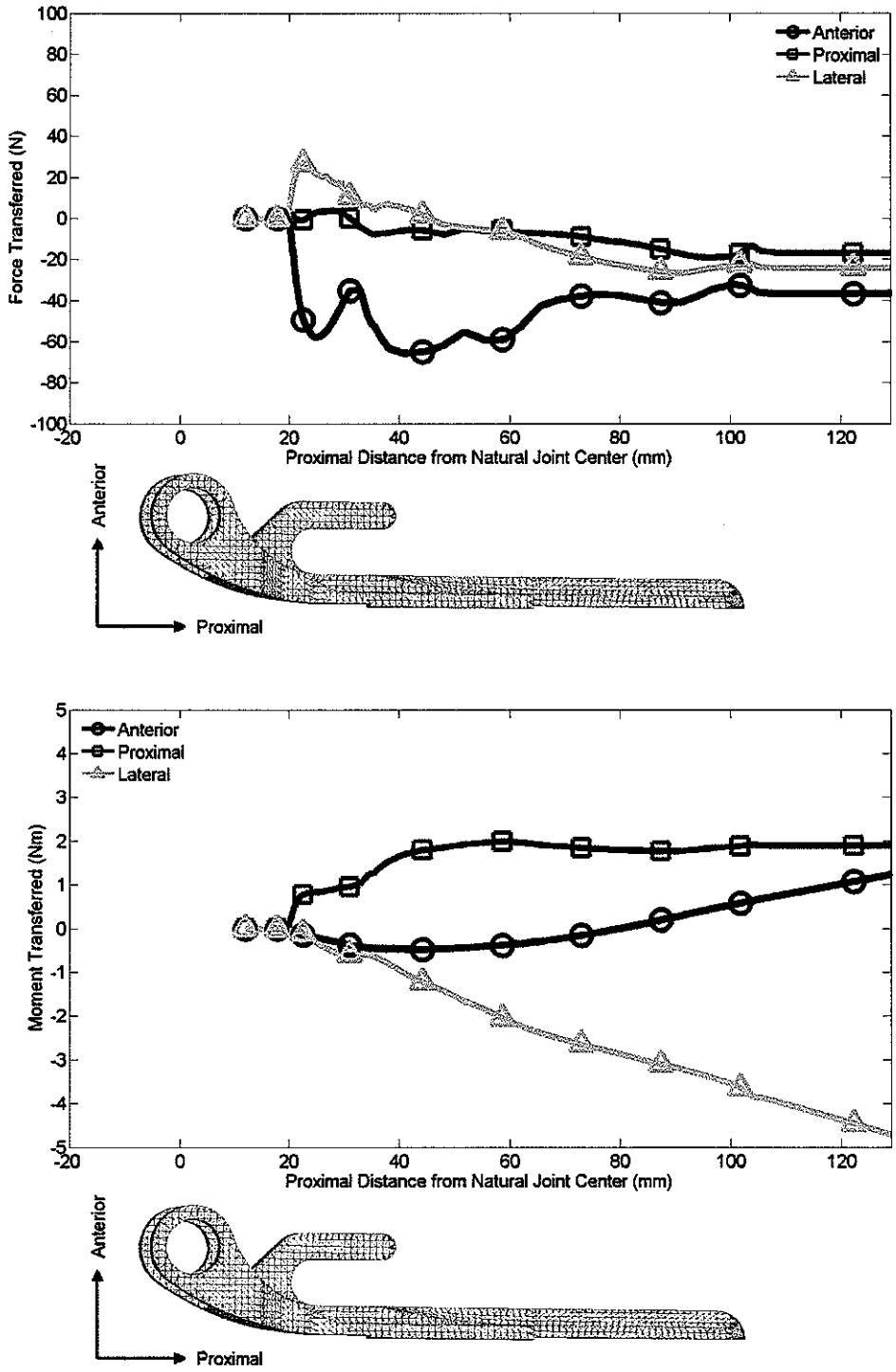

Figure 5.14: Forces and moments transferred into the bone for the unsupported (BC=0) interface conditions with the humerus in position 10 and α=0.5.

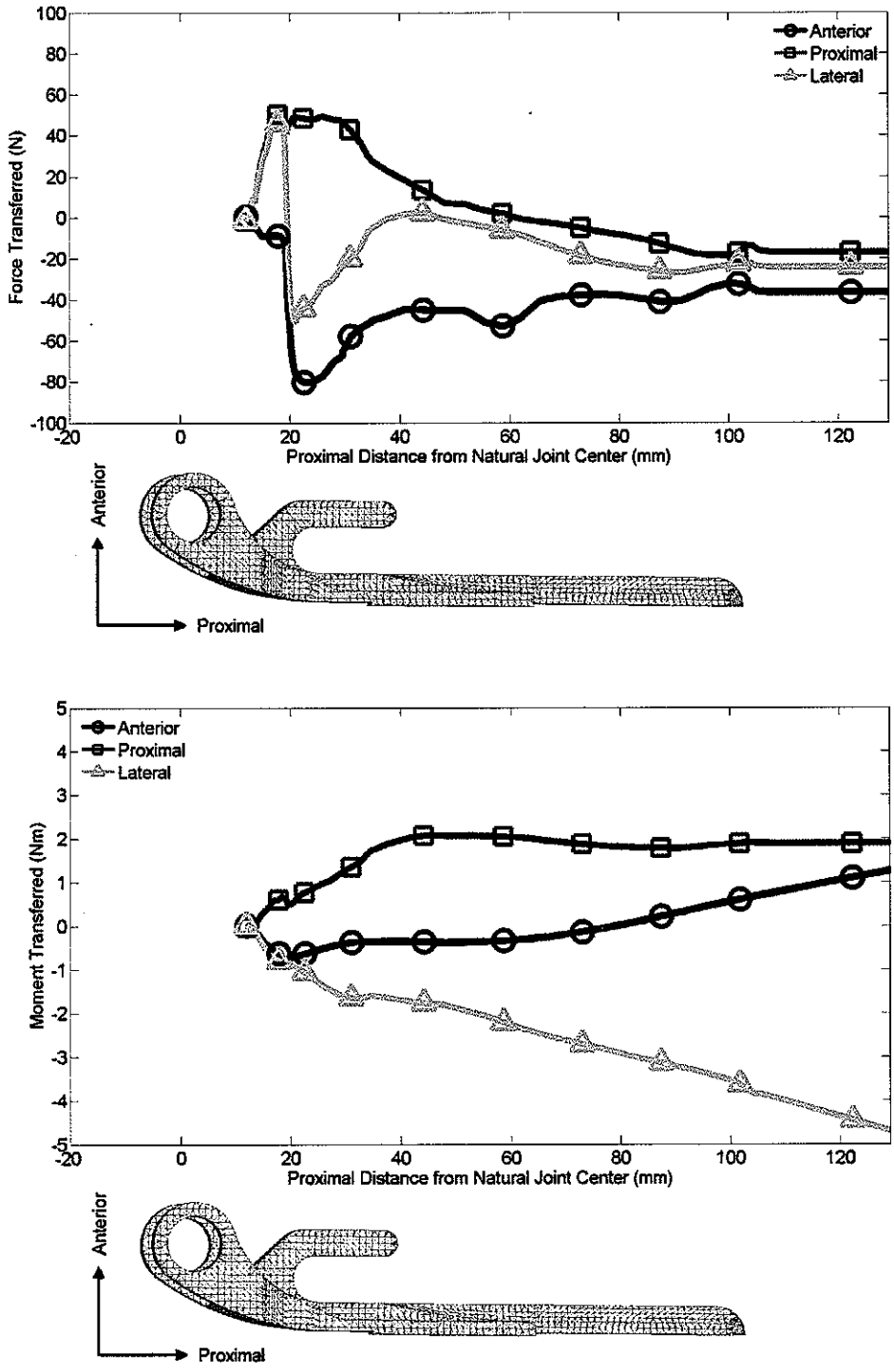

Figure 5.15: Forces and moments transferred into the bone for the frictional (BC=0.5) interface conditions with the humerus in position 10 and α=0.5.

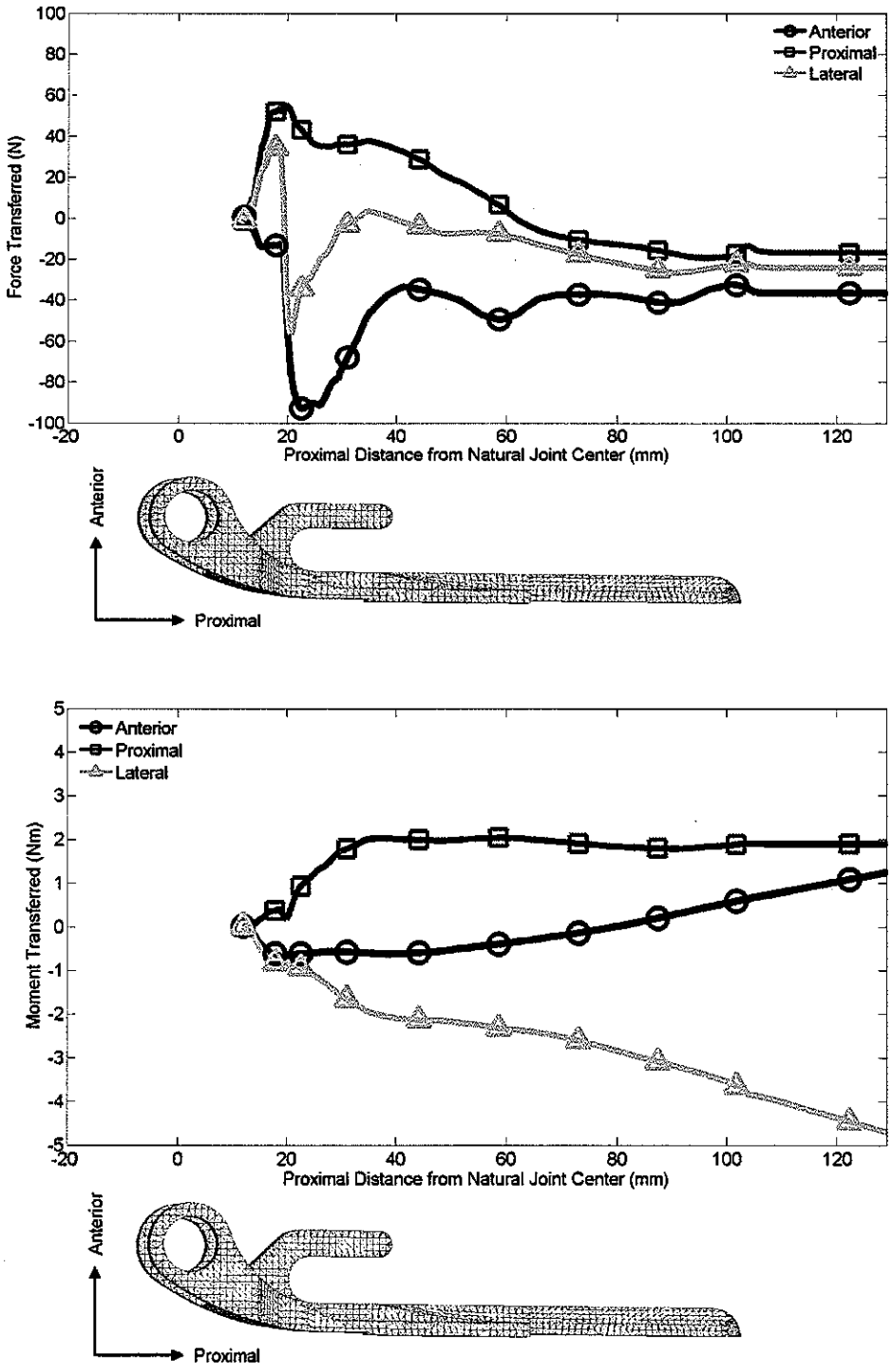

Figure 5.16: Forces and moments transferred into the bone for the bonded (BC=1) interface conditions with the humerus in position 10 and α=0.5.

humeral center of rotation increases. This can be seen for the case in which the humerus is in position 10 in figures 5.14-5.16. For the interface boundary conditions in which the distal humeral component comes into direct contact with bone (BC=0.5 – Figure 5.15, BC=1 – Figure 5.16), it can be seen that load transfer to the humerus begins roughly 10 mm from the natural center of joint rotation. However, for the case in which the distal humeral implant is largely unsupported (BC=0, Figure 5.14), load transfer to the humerus does not begin until roughly 20 mm from the natural joint center.

5.3.3 Cement Stresses

Maximum principal stresses in the cement mantle were only sensitive to interface boundary condition (Table 5.6). No other parameter caused a substantial change in the cement stresses observed. No parameter caused a substantial change in the cement stresses in the proximal region (Figure 5.17).

Table 5.6: Coefficients of the Linear Regression of Cement Stresses

$\sigma_{PROX\_CEMENT} = \gamma_1 * AP + \gamma_2 * PD + \gamma_3 + VV + \gamma_4 * IE + \gamma_5 * \alpha + \gamma_6 * BC + \gamma_7$.							
	γ_1	γ_2	γ_3	γ_4	γ_5	γ_6	γ_7
Distal Region	0.16	-0.09	-0.36	0.01	-0.05	-2.74	4.97
Middle Region	-0.01	-0.05	-0.10	-0.00	-0.08	-0.87	1.48
Proximal Region	0.01	0.00	-0.04	-0.01	-0.09	0.01	0.46

The observed changes in the magnitudes of the maximum principal cement stresses were found to be significant for both the distal cement ($p<0.001$) and middle cement ($p<0.001$) regions.

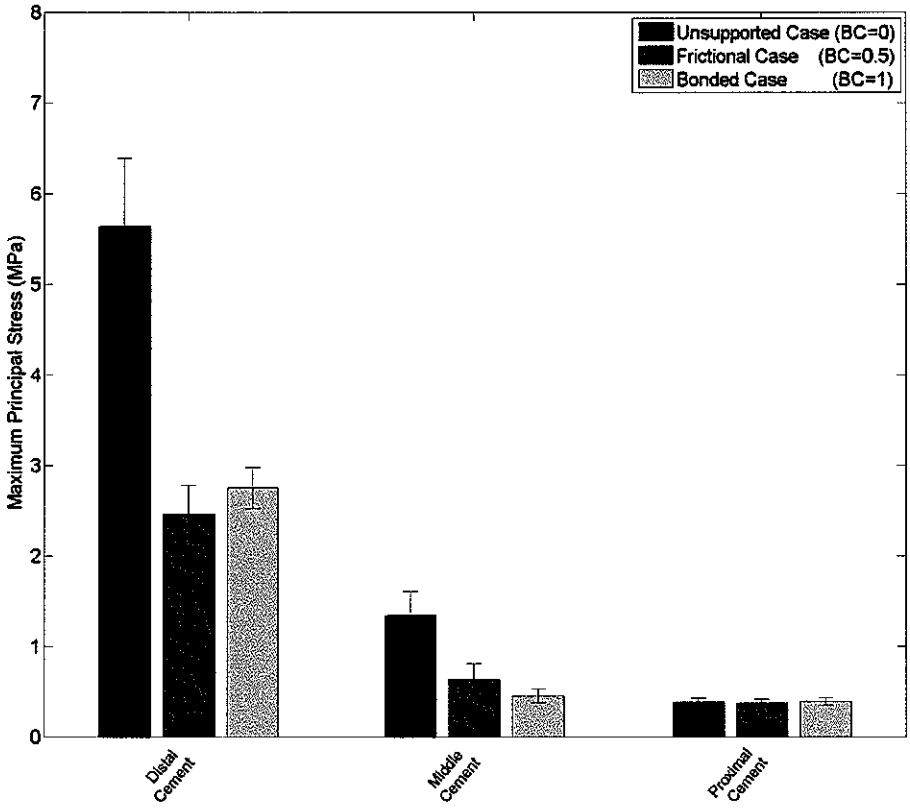

Figure 5.17: Volume-weighted maximum principal cement stress in 5% most highly stressed volume in three regions of the humeral cement mantle

5.4 Discussion

The objective of this study was to determine the structural response of the humeral-bone implant system under common activities of daily living. We sought to investigate the effects of both implant position and fixation characteristics on load transfer from the implant to the bone and on the strains arising in the bone and stresses arising in the cement mantle. To account for some of the variation in bone material properties that occurs naturally throughout a population, implant positions and fixation were evaluated for three density-to-modulus relationships for bone.

This study predicts that well-fixed and well-supported humeral implants both transfer load to the bone more distally and promote less stress in the distal region of the

cement mantle than implants in which load transfer is accomplished only through the implant stem. A complex mechanism of load transfer appears to be in place in the current Coonrad-Morrey total elbow replacement, in which the preferential load path seems to be through the chevron and the base of the flange. However in situations where contact between implant and bone has been compromised distally, load is transferred instead through the entirety of the stem. Thus, without knowing the specific position of the implant with respect to the surrounding bone for a particular patient, the manner of *in vivo* load transfer to the bone cannot be identified. Although the maximum principal stresses in the cement mantle never exceed an 8 MPa typical fatigue limit for polymethylmethacrylate (PMMA) bone cement [41], the values of cement stress do begin to approach this limit for the unsupported case and are significantly increased over the bonded and frictional boundary interface cases. Clinically, however, breakdown of the cement layer has been observed. Without knowing the precise implant position in those patients, however, it is difficult to say whether those clinical experiences agree with our predictions. It is also important to remember that the loading conditions applied to these finite element models were derived using a biomechanical model from motions in which the subject was only holding a single pound in their hand in order to comply with the suggested activity restrictions following total elbow arthroplasty [57]. It is not, however, unreasonable to assume that during the course of normal daily activities an unsupervised total elbow recipient may exceed the one-pound limitation enforced in this study. Of course, if that were to happen, the stress levels seen in this study, which are already near the fatigue limit of cement, would likely rise.

The dearth of existing finite element models of any type of total elbow replacement makes it difficult to directly compare our results with any previous computational

analyses. Only two three-dimensional finite element analyses have been published and the loading for those studies as well as the particular implant geometries used were substantially different from those in these analyses. Recently, however, an *in vitro* study was performed to assess the effect of the addition of an anterior flange and of variations in the graft modulus under the flange on the strains in the anterior cortex of the distal humerus [65]. Under the application of both axial and bending loading regimes, the authors determined that the presence of an anterior flange and changes in stiffness of the graft material have no effect on the strains in the underlying anterior cortex and therefore on load transfer to the bone. Furthermore they state that the presence of the collar, which in this current study corresponds to the chevron and flange base of the humeral component, does affect load transfer especially under axial loading conditions. Both of these phenomena can be seen in the results of the finite element analyses in the present study where load transfer through the flange is minimal for all cases (Figure 5.11-A, B, C) and the inclusion of contact at the chevron and flange base substantially alters the load transfer through the distal stem of the implant (Figure 5.11-A, B). Thus, while the entirety of the current finite element analyses may not be able to be directly validated, it is shown to correctly predict a limited set of load transfer phenomena at the distal humerus.

Our study must be interpreted within the limits of the finite element methodology. Finite element modeling provides a means to investigate both the surface and internal response of a system. However, the specific values of the numerical results reported by a finite element analysis are dependent upon mesh and material discretizations as well as other, more general assumptions made when creating a model of the system to be investigated. For example, it is unlikely that any of the interface conditions investigated in this study accurately portray the physical, implanted system as it

behaves *in vivo*. However, the three interface boundary interface conditions studied are likely to bracket the spectrum of conditions that will exist, and thus provide insight into how greater or lesser degrees of stability and fixation will affect the structural responses in which we are interested. Also, because the specific values of the responses in which we are interested are dependent upon the numerical and theoretical approximations that are made when constructing these models, it is difficult to directly relate the quantities observed to critical values that may be obtained through external experimental testing. Instead these finite element analyses allow us to answer whether the perturbations we make to our models bring the responses closer to or further from these established critical values.

In summary, humeral position has been shown to have little effect on load transfer from the implant to the bone, maximum principal tensile stresses in the cement mantle, or the minimum principal compressive strains in the bone itself. Thus, humeral implant position may be chosen in order to minimize contact forces on the articular surface of the implant as discussed previously without negatively impacting the structural response of the humeral bone-implant system. However, although the position of the humerus with respect to the natural axis of bone has little effect on structural responses, the humerus should always, if possible, be implanted in such a way that the proximal surface of the implant chevron be in contact with the remaining extent of the distal humeral condyles to preserve the primary load transfer pathway.

Chapter 6

Effects of Humeral Implant Position, Fixation, and Bone Modulus on the Structural Behavior of the Ulnar Component of the Coonrad-Morrey Total Elbow Replacement

6.1 Introduction

In previous chapters, we have investigated the effects of both surgical and environmental factors on the performance of a contemporary semiconstrained total elbow replacement, the Coonrad-Morrey. We determined that the contact forces on the articular surfaces of the implant would be increased with internal rotation of the humeral component. We have also investigated the effect of humeral component position, fixation and surrounding bone moduli on the stresses, strains, and load transfer in the humeral bone-implant system. We found that only fixation had a

significant effect on cement stresses and load transfer. From the results of these two prior analyses, we suggested that humeral implant position need not be considered when contemplating the structural response of the bone-implant system, and therefore the humeral component could be implanted in such a way as to minimize articular contact force. However, since humeral position affects the forces at the joint, and since these forces are applied to both the humeral and ulnar components of the implant, it is necessary to examine the structural response of the ulnar bone-implant system as well.

Historically, the ulnar aspect of the Coonrad-Morrey total elbow replacement was implicated in implant loosening less often than the humeral component. However, with the improvements made to the humeral component to address these early implant failures, ulnar component loosening has become a more common reason for implant revision [1, 21, 26]. Unfortunately, since the humeral aspect was traditionally responsible for implant failure, even less attention has been devoted to the structural response of the ulnar bone-implant system than was devoted to the humeral system.

Only one study on the mechanical behavior of the implant ulnar component of the Coonrad-Morrey has been published. To accompany their humeral finite element study, Goel at el. [23] examined the von Mises stress response of the implant, bone, and cement about an early-generation Coonrad ulnar component. Cortical bone in this study was modeled as transversely isotropic with homogeneous material properties and cancellous bone was modeled as isotropic with homogeneous properties. Three load cases were used: a 1 N inferior load, a 1 N posterior load, and a 1 N-cm axial torque. As with their humeral analysis, they determined that axial torque caused the largest percentage increase in von Mises stresses over the maximum stress present in

the natural elbow and that posterior loading engendered the largest magnitude stresses in both the cortical and cancellous bone in both the natural and implanted ulnae. Similar to the humerus, the implant-cement and cement-bone interfaces were modeled as bonded, no examination of altered interface conditions was performed, and the analysis was fully linear.

Our aim in this study of the ulnar system was much the same as our previous study of the humeral bone-implant system. We sought to investigate the structural response of the bone and cement mantle under loading conditions that could arise during a typical activity of daily living. We wanted to investigate the effect of the changes in ulnar component position, implant degree of fixation, and changes in the surrounding bone moduli on the maximum principal stresses in the cement and minimum principal strains in the bone. Finally, we wanted to examine the effect of these parameters on the load transfer from the ulnar component of the implant and to the surrounding bone.

6.2 Methods

Finite element analyses were used to investigate the relationship between ulnar implant fixation, ulnar bone modulus, and humeral component position on the structural response of the ulnar bone-cement-implant system incorporating a contemporary Coonrad-Morrey total elbow replacement. Three-dimensional surface geometry of the ulna and bone material properties were extracted from computed-tomography scans of the elbow. Ulnar component geometry was constructed from surgical templates. Finite element models were created from these geometries and included 20,580 linear hexahedral elements and 23,587 nodes. Loads from the previous humeral analyses were transformed into an ulnar coordinate system and applied to our models. Sixty finite element analyses were run of the ulnar bone-

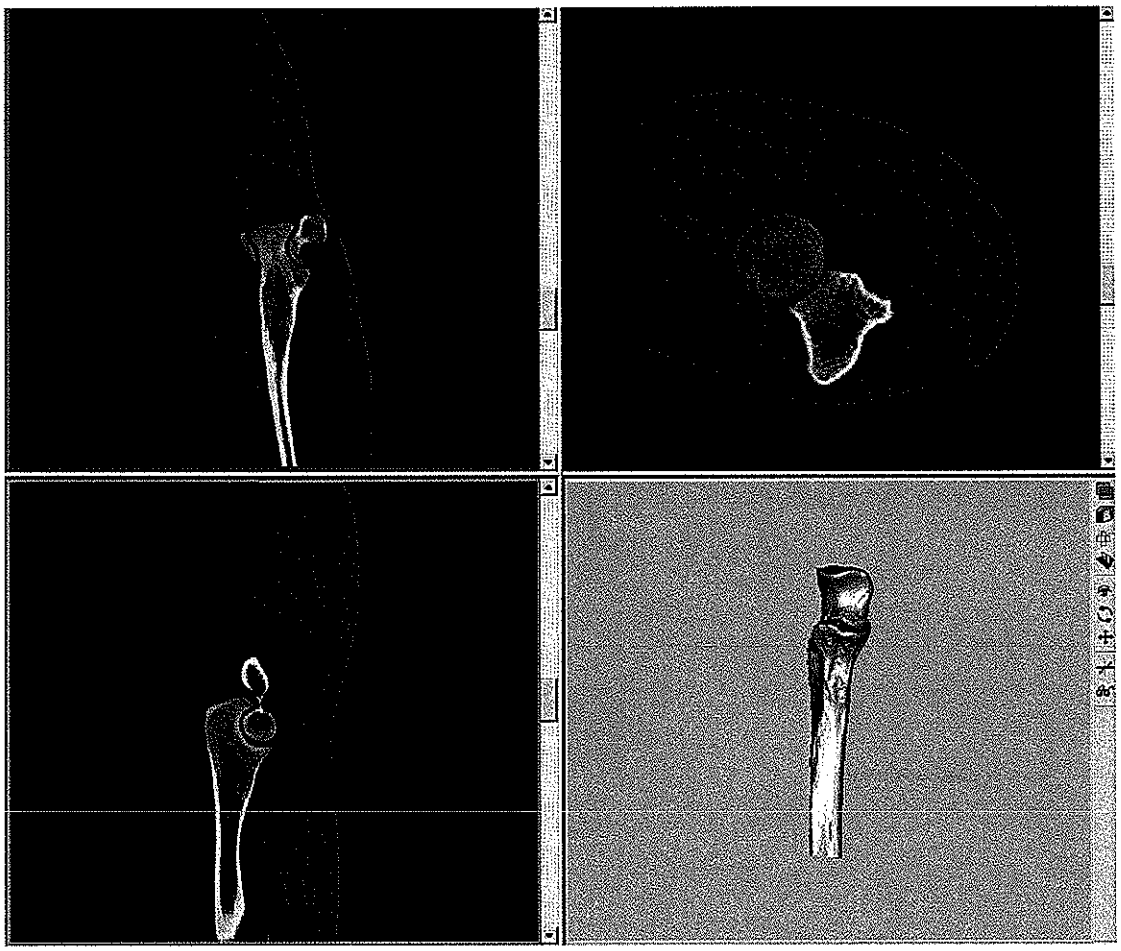

Figure 6.1: Masking and processing of ulnar bone to create surfaces for later finite element meshing

implant system. In total, ten humeral positions, three density-modulus relationships, and two interface conditions were studied.

6.2.1 Geometry Creation

Ulnar geometry was obtained from a single computed tomography (CT) scan of a healthy male elbow that was previously used to create the humeral models of Chapter 5. A mask of the ulna was created by thresholding the bone from the soft tissue using Mimics 12 (Materialise, Leuven, Belgium) (Figure 6.1). All pixels with Hounsfield Units (HU) greater than 226 and less than 2117 were considered to be bone. Ulnar bone was separated from the bones of the radius and the humerus though region

growing. Small inclusions in the exterior of the ulnar bone mask were filled manually and boundary curves were created around the exterior surface of the bone in each scan. These boundary curves were then filled to create a mask of the entire ulna including the medullary canal. A surface representation of the exterior ulna was then imported into Studio 4.0 (Geomagic, Research Triangle Park, NC) where it was smoothed and refined to create the final non-uniform rational B-spline (NURB) surfaces used for finite element mesh projection.

Using Pro/Engineer Wildfire 3.0 (Parametric Technology Corporation, Needham, MA), a surface model of the ulnar component of the Coonrad-Morrey was created from surgical templates and product brochures. As with our previous humeral analyses, the small ulnar component size was chosen on the advice of our clinical collaborators. The shortest stem length (approximately 76 mm) was chosen to insure adequate distance between the tip of the implant component and the fixed distal boundary of the ulna.

6.2.2 Finite Element Mesh Creation

Finite element meshes of the ulna and the implant were created using Truegrid (XYZ Scientific Applications, Inc., Livermore, CA). Based upon published surgical techniques, the bone surface was altered to accommodate the implant geometry. The anconeal process of the ulna was removed according to common surgical technique (Figure 6.2). A 1 mm cement mantle was created around the implant stem. The implant was positioned such that the tip of its distal stem was centered in the distal medullary canal. The proximal articulation of the implant was positioned in order to not violate the proximal cortical surfaces while aligning the implant as well as possible with the natural center of the articulation. Final implant positioning was verified by

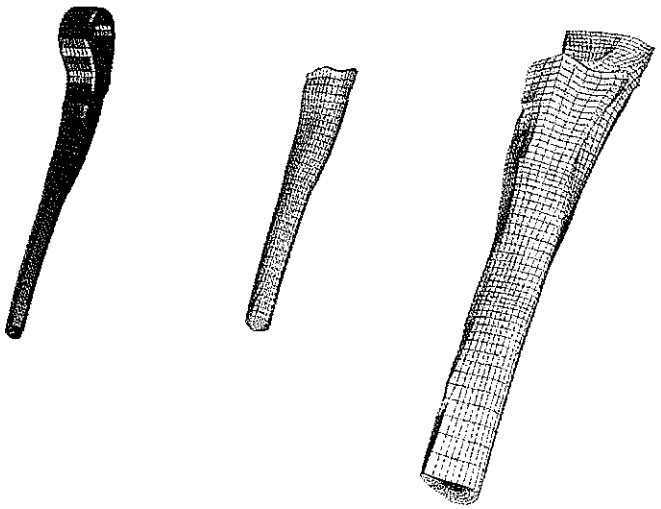

Figure 6.2: Exploded view of the finite element mesh showing the implant, cement, and bone (from left to right)

surgeon collaborators (Figure 6.3).

6.2.3 Finite Element Analyses

Material Property Assignment

Each element of the finite element mesh was assigned linear elastic, isotropic material properties with a Poisson's ratio of 0.3. The elastic moduli of the elements comprising the titanium implant were 110 GPa. The elastic moduli of all elements of the cement mantle were 2 GPa.

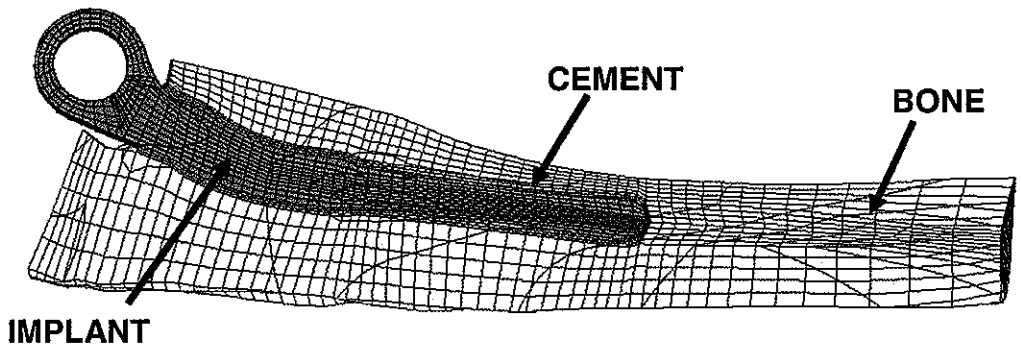

Figure 6.3: Sagittal cross-section showing the finite element meshes of the ulna, implant, and cement mantle

To assign moduli to each element of bone, the bone finite element mesh was imported into Mimics. At each element integration point, interpolation of the Hounsfield units of surrounding voxels that lay within the previously defined ulnar mask was performed in order to determine a single Hounsfield value at that integration point. A volume weighted averaging of the integration points of an element was then performed to determine a single Hounsfield value for each element. Since the ulna was from the same scan as the humerus investigated previously, the calibration points between Hounsfield unit and density and between density and modulus that were determined for the humerus were also used for the ulnar analyses. As in Chapter 5, the relationship between density and bone modulus was found by taking the weighted average:

$$\bar{E} = \alpha * \bar{E}_{LB} + (1-\alpha) * \bar{E}_{UB}$$

of the upper and lower bound curves:

$$E_{UB} = \begin{cases} 10.55*(1.79*\rho_{ash}+0.0019)^{1.72} & 0.0\ g/cm^3 \leq \rho_{ash} \leq 0.38\ g/cm^3 \\ 26.1489*\rho_{ash}-3.4644 & 0.38\ g/cm^3 < \rho_{ash} \leq 1.2\ g/cm^3 \end{cases}$$

and

$$E_{LB} = \begin{cases} 7.54*(1.79*\rho_{ash}+0.0019)^{1.94} & 0.0\ g/cm^3 \leq \rho_{ash} \leq 0.38\ g/cm^3 \\ 20.0164*\rho_{ash}-3.2605 & 0.38\ g/cm^3 < \rho_{ash} \leq 1.2\ g/cm^3 \end{cases}$$

for values of α equal to 0, 0.5, and 1 (Figure 6.4), resulting in the distributions seen in Figure 6.5.

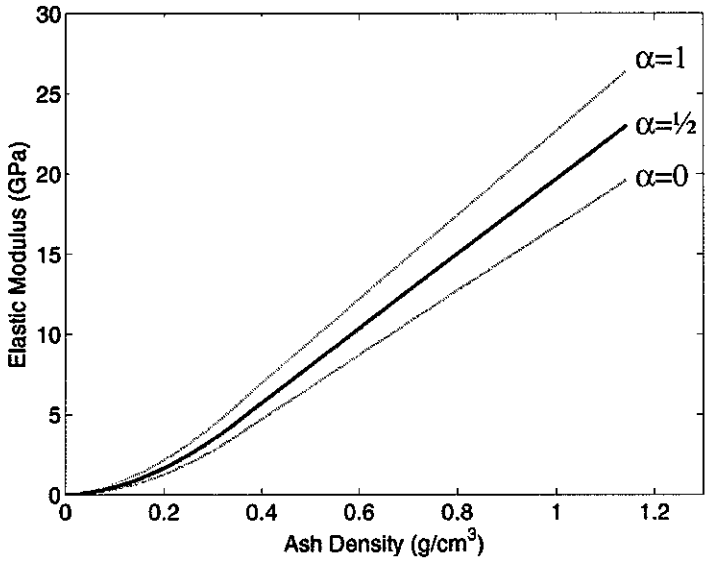

Figure 6.4: Upper (α=1), middle (α=0.5), and lower (α=0) bound modulus relationships used to assign elastic moduli to elements of ulnar mesh

Interface Modeling

The cement-bone interface was always modeled as bonded (displacement compatible). The interface between the non-beaded, smooth surfaces of the ulnar component and the cement layer was modeled as a non-tension interface with a friction coefficient of 0.3 [52]. The interface between the beaded implant surface and the cement layer was varied as specified in Table 6.1.

Table 6.1: Summary of Analysis Boundary Conditions

BC	Boundary Condition	Description
0.5	Frictional	Cement/bead interface: friction, μ=0.8
1	Bonded	Cement/bead interface: Displacement compatible

In the frictional case (BC=0.5), the interaction between the beaded surface of the implant and the cement was modeled as a non-tension interface with a coefficient of friction of 0.8. The interaction between the beaded implant surface and the cement in the bonded interface case (BC=1) was modeled as displacement compatible.

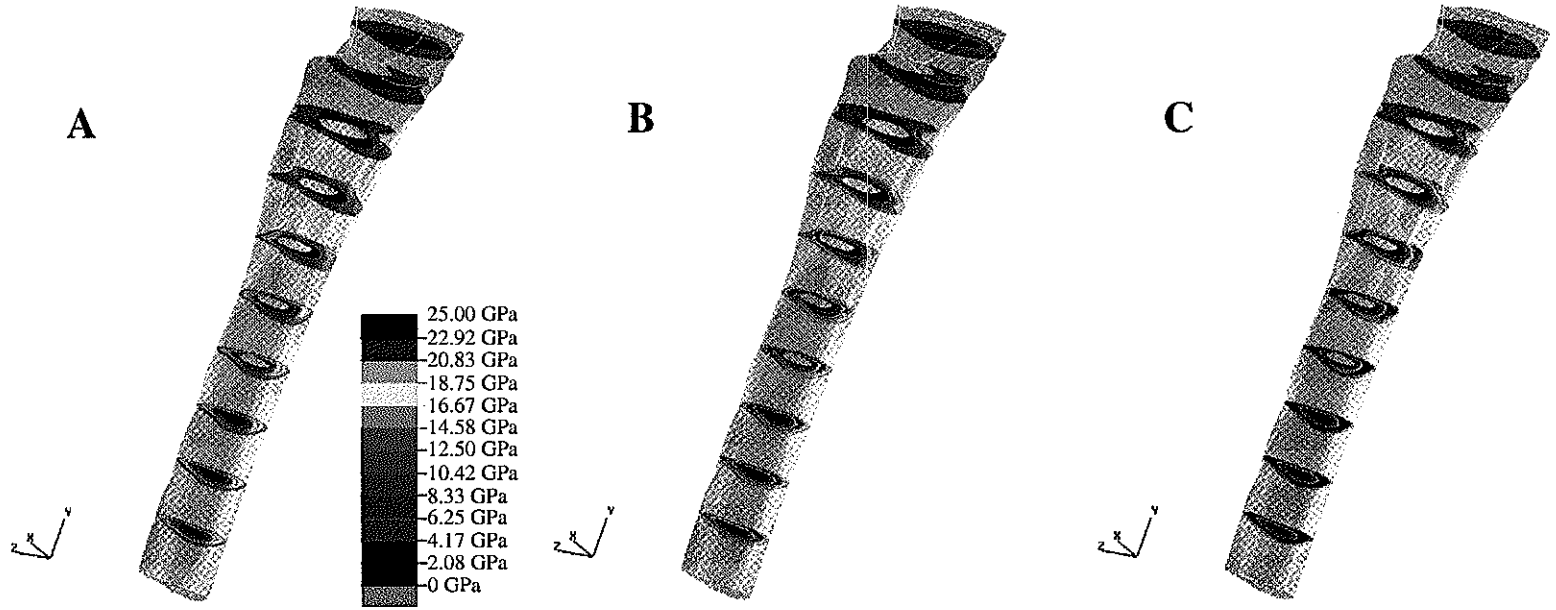

Figure 6.5: Elastic modulus distributions in the ulna for the case of A) α=0, B) α=0.5, and C) α=1

Boundary conditions were identified in this way to be consistent with the previous humeral analyses.

Implant Positioning

For these analyses, ulnar implant position was held constant, and the effects of varying the humeral implant position on the loading transmitted to the ulnar component were determined. The humeral positions examined in these analyses were the same as used for the humeral studies in Chapter 5. Humeral positions were defined by a set of four parameters: proximal-distal (PD) and anterior-posterior (AP) displacements of the component from the natural joint center, and internal-external (IE) and varus-valgus (VV) rotations of the implant from the natural axis orientation (Figure 3.1). The natural joint center of the humerus was taken as the center of the cylinder fit to the smallest diameter of the trochlear sulcus of the natural elbow. The humeral positions are summarized in Table 6.2.

Table 6.2: Humeral Implant Displacement from Natural Axis

Humeral Implant Position	Varus(+)/ Valgus(-) Rotation (°)	Internal(+)/ External(-) Rotation (°)	Anterior(+)/ Posterior(-) Translation (mm)	Proximal(+)/ Distal(-) Translation (mm)
1	1.5	0	4.8	2.5
2	2.3	-2.5	4.5	0.6
3	1.9	-3.8	4.1	-0.6
4	1.7	-0.6	3.9	-4.2
5	1.3	0.6	4.7	-3
6	2.2	-1.6	4.3	3.4
7	2.5	-2.8	4.8	-2.8
8	2.7	-3.3	3.8	1.3
9	2.1	-3.9	4.6	-3.6
10	2	-1.1	5	0.5

Boundary Conditions

The loads used in Chapter 5 were converted to an equivalent loading in the coordinate system of the ulnar finite element model. The origin of the ulnar coordinate system was placed at the point of load application at the center of the ulnar component articulation. The x-axis was anteriorly directed, the y-axis was proximally directed parallel to the long axis of the ulna, and the z-axis was the laterally pointing cross-product of the anterior and proximal axes. At the points in the loading curves associated with the maximum contact force on the articular bushings, as discussed in Chapter 5, the joint reaction forces in the humeral coordinate system were determined and transformed into the ulnar coordinate system (Table 6.3) using knowledge of the upper extremity joint angles at the position of maximum contact force application and of an elbow carrying angle calculated from the CT data. Similar to the humeral case, forces and moments were applied to a reference node at the origin of the ulnar coordinate system and transmitted to the implant through the use of a rigid analytical cylindrical surface that was displacement compatible with the internal diameter on the ulnar component into which the articular bushings insert. To fully constrain the finite element model and eliminate rigid body displacement modes, nodes on the distal surface of the ulnar mesh were fixed.

6.2.4 Data Analysis

Nodal loads on the surface of the implant were calculated as in Chapter 5. Load transfer was separated into three sections across the ulnar component (Figure 6.6): the distal stem, the beaded stem, and the proximal stem. The distal stem encompassed the all of the stem that lies distal to the beaded portion of the stem. The beaded stem section consisted of the portion of the stem to which a beaded layer had been applied by the manufacturer to increase cement interlock. The proximal stem encompassed

Table 6.3: Input Joint Reaction Loads

Humeral Implant Position	Anterior(+)/ Posterior(-) Reaction Force (N)	Proximal(+)/ Distal(-) Reaction Force (N)	Lateral(+)/ Medial Reaction Force (N)	Varus(+)/ Valgus(-) Reaction Moment (Nmm)	Internal(+)/ External(-) Reaction Moment (Nmm)	Lateral(+)/ Medial(-) Reaction Moment (Nmm)
1	-9	-38	26	-2684	-276	291
2	-7	-38	27	-2542	-297	276
3	-6	-39	26	-2478	-299	269
4	-7	-38	26	-2645	-294	287
5	-8	-38	25	-2709	-283	294
6	-9	-38	27	-2605	-287	283
7	-6	-38	27	-2514	-313	273
8	-7	-38	28	-2512	-307	272
9	-5	-39	26	-2455	-316	266
10	-8	-38	26	-2617	-288	284

the stem proximal to the beaded surface. Net load transfer in each stem section was calculated.

In the native ulna, joint loads are transferred to the bone proximally. To determine which parameters were most able to replicate this natural condition, multiple linear regression models were used to determine which had the largest effect on load transfer

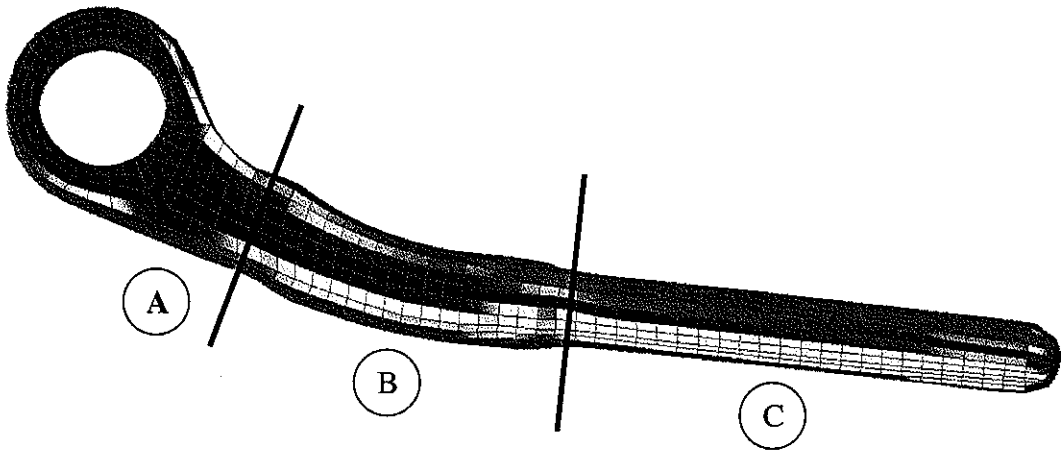

Figure 6.6: Three sections across which load transfer was calculated: A) proximal stem, B) beaded (middle) stem, and C) distal stem

across the distal implant stem away from the joint. These regression models included only first order terms. After determining which parameters had the most effect, one-way analyses of variance were performed on each parameter to determine which of those parameters significantly affected load transfer. Cumulative and nodal load transfer were examined for parameters identified as significant. Smoothing of the load transfer curves was performed as described in Chapter 5.

Stress in the cement layer was also studied. The cement layer was separated into three sections that corresponded to the stem sections used when analyzing load transfer (Figure 6.7). Thus the distal cement layer was comprised of all cement elements that lie solely to the outside of the distal stem. The proximal cement layer consisted of all cement elements that lie solely outside the proximal stem, and beaded or middle layer consisted of the elements surrounding the beaded interface. For each section, the volume-averaged maximum principal stress in the mostly highly stressed 5% of that section's volume was calculated. As in the humeral analyses, this measure was chosen to minimize the effects that mesh discretization and suboptimal element shape may have on the values of peak stresses calculated in regions of complex geometry. As

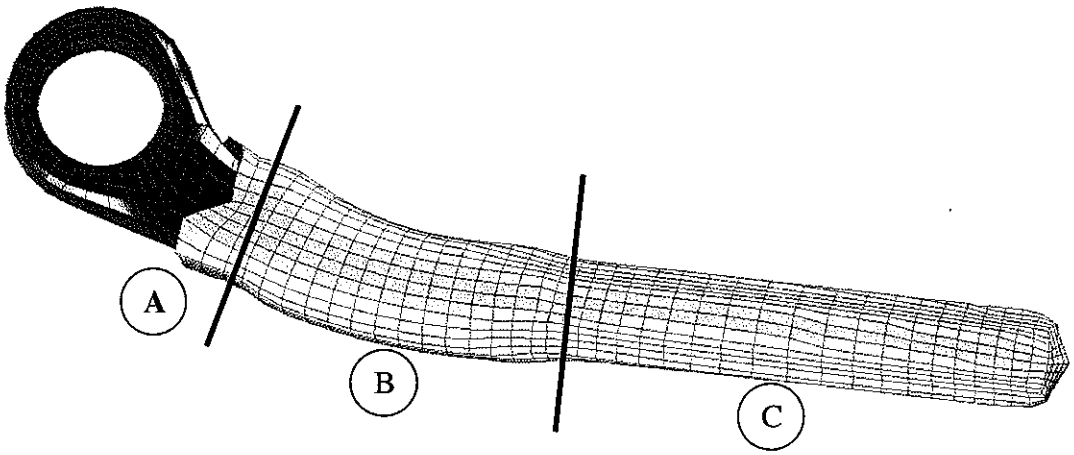

Figure 6.7: Three regions in which cement stresses were calculated: A) proximal cement, B) middle cement, C) distal cement

with load transfer, multiple linear regression models were used to determine which parameters had the largest effect on cement stresses. One-way analyses of variance were used to determine which of these effects were significant.

6.3 Results

63.1.1 Bone Strains

For all variations in humeral component position, boundary interface condition, and density-elastic modulus relationship, the minimum principal compressive strains in the ulna were always less than 0.7%, the published yield value for trabecular bone [56]. Minimum principal strains were greatest in the proximal bone for cases in which the cement-implant interface was unbonded (BC=0.5, no-tension, friction) (Figures 6.8 and 6.9).

6.3.2 Load Transfer

The force transferred across the distal section of the stem was most sensitive to the interface boundary condition (BC) and density-modulus weighting factor (α). The coefficients of the response with respect to these two input parameters were -23.72 and -2.70, respectively (Table 6.4).

Table 6.4: Coefficients of the Linear Regression of Distal Stem Force

$F_{DISTAL\_STEM} = \beta_1 * AP + \beta_2 * PD + \beta_3 + VV + \beta_4 * IE + \beta_5 * \alpha + \beta_6 * BC + \beta_7$.							
	β_1	β_2	β_3	β_4	β_5	β_6	β_7
Distal Stem Force	-0.05	-0.01	-0.29	0.27	-2.70	-23.72	39.29

Of the two parameters to which the force transferred across the distal stem was most

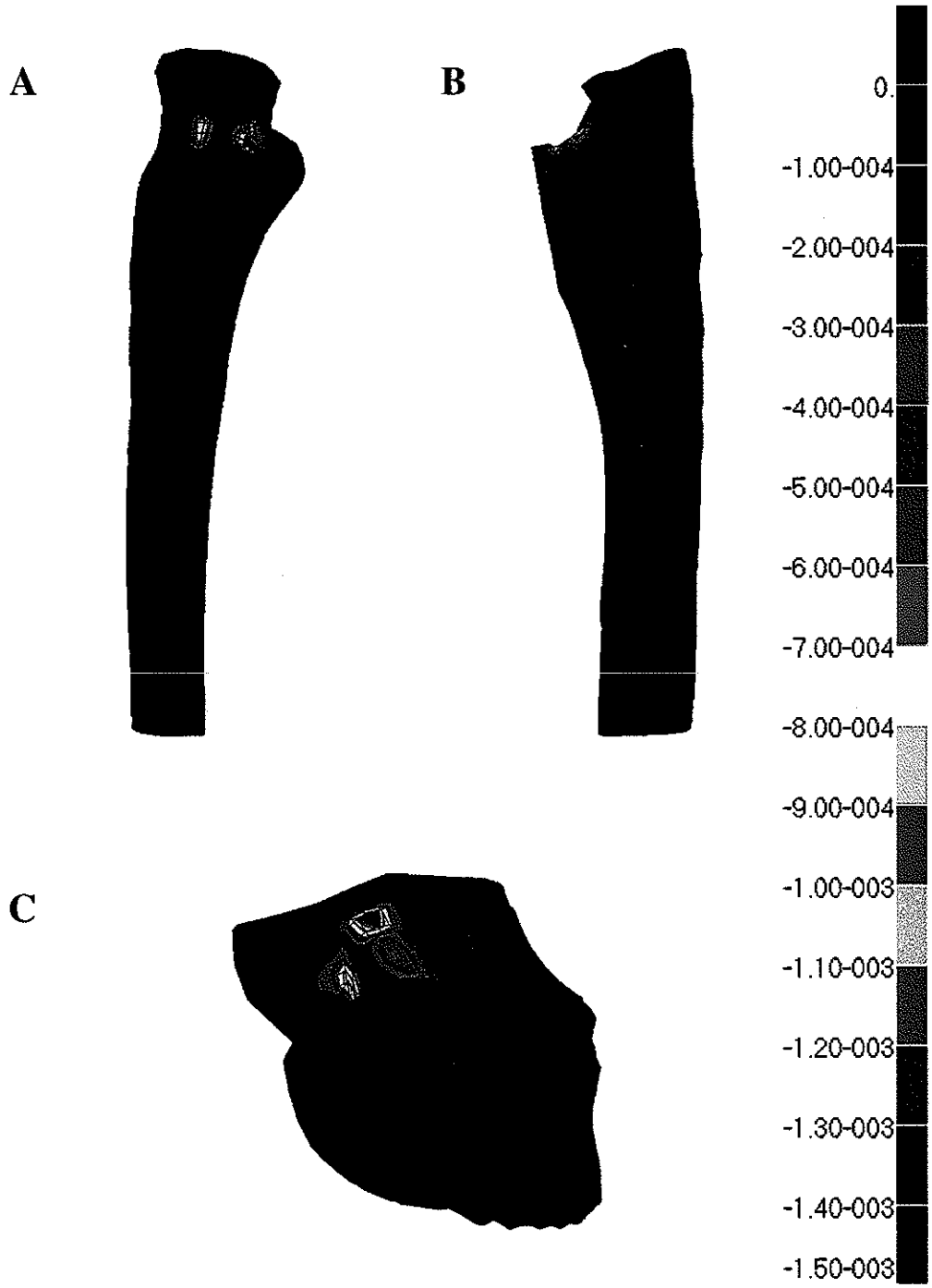

Figure 6.8: Minimum principal strains in the ulna with the humerus in position 10, BC=0.5 and α=0.5. A) Anterior to posterior view, B) Medial to lateral view, C) Distal to proximal view

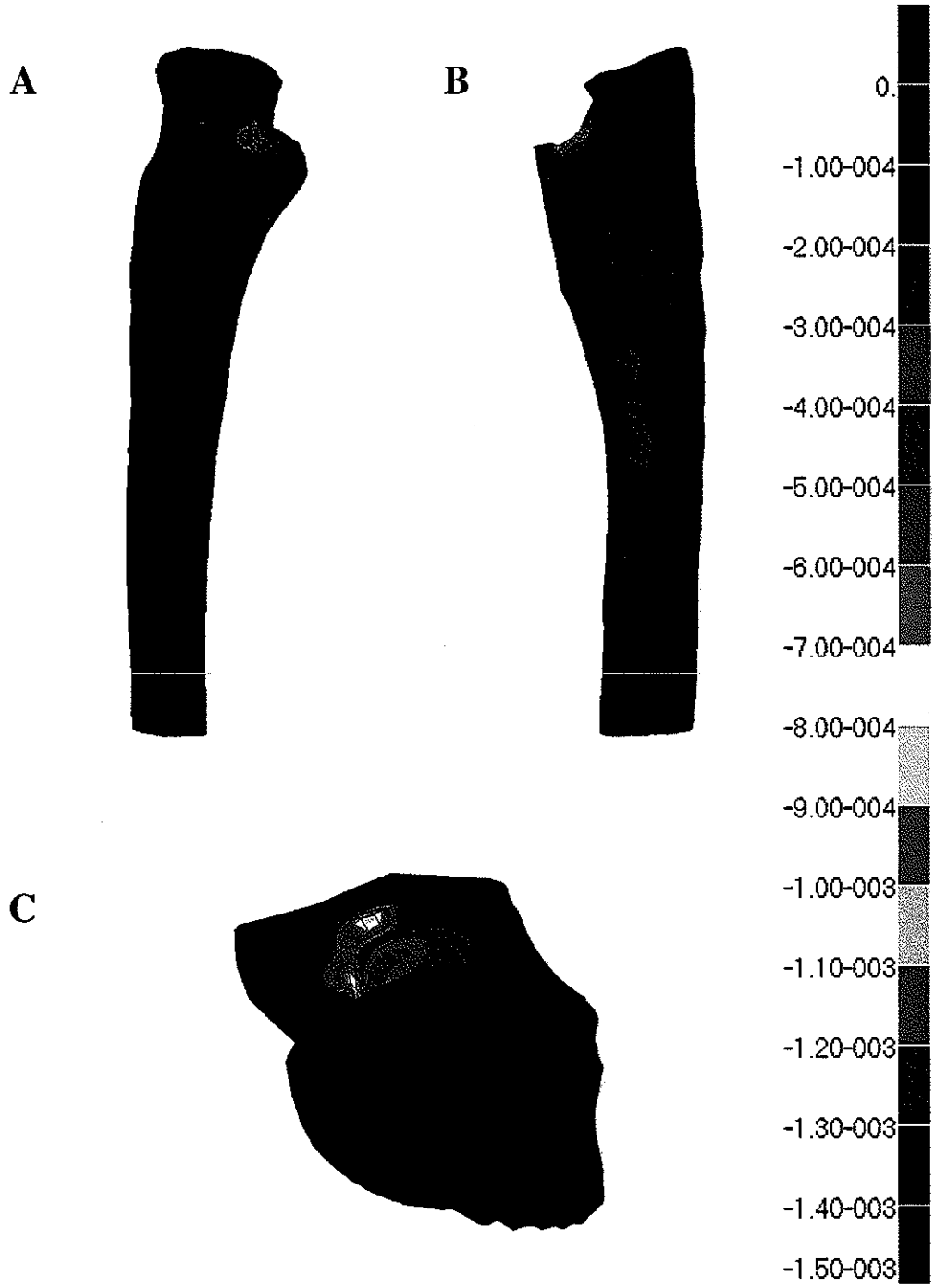

Figure 6.9: Minimum principal strains in the ulna with the humerus in position 10, BC=1 and α=0.5. A) Anterior to posterior view, B) Medial to lateral view, C) Distal to proximal view

sensitive, only the effect of interface boundary condition (BC) was found to be significant ($p<0.001$) (Figure 6.10); the effect of density-modulus relationship weighting factor (α) was not ($p=0.8$).

In analyses with a frictional interaction between the beaded implant surface and the cement (BC=0.05), increased load transfer from the implant can be seen closer to the articulation of the ulnar component (Figure 6.11). In analyses where these surfaces are completely bonded, load transfer diminishes at the proximal end of the implant but increases around the beaded section.

These areas of increased load transfer may be also be viewed by examining how the

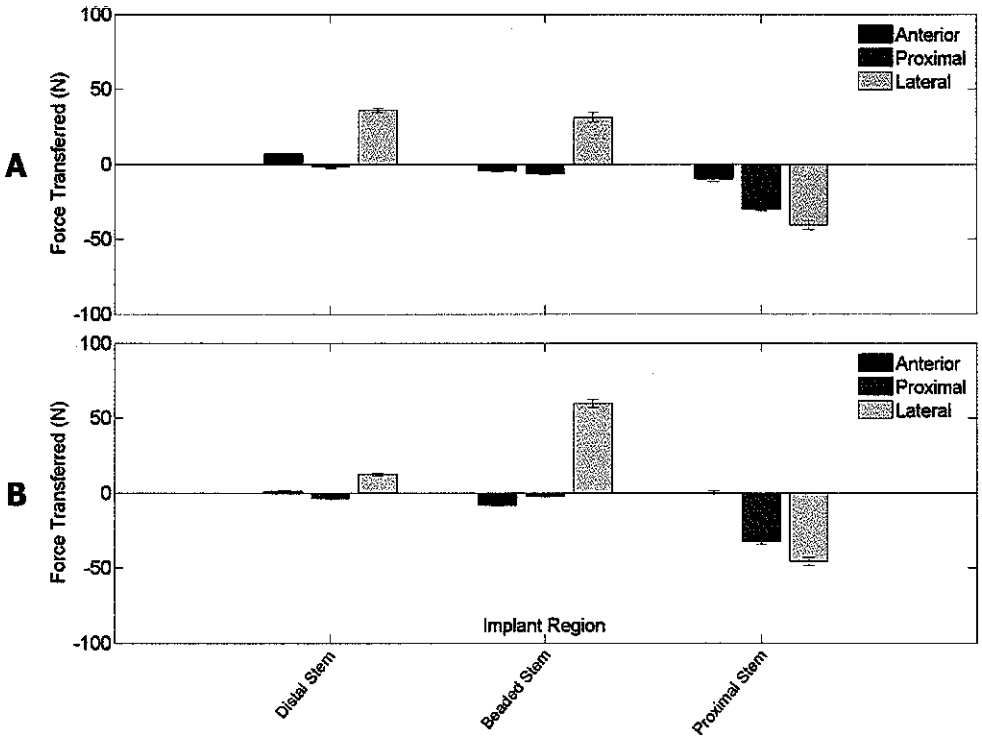

Figure 6.10: Net load transfer across three defined sections of the ulnar component for the A) Frictional (BC=0.5), and B) Bonded (BC=1) interface boundary conditions.

cumulative forces and the moments in the bone change as the distance from the ulnar center of rotation increases. These curves are shown for the case in which the humerus is in position 10 (Figures 6.12-6.13). For the interface boundary conditions in which there is only a frictional interaction between the cement and beaded implant surface (BC=0.5, Figure 6.12), a posteriorly directed load is transferred to the bone proximal to the beaded surface and a laterally directed load is transmitted to the bone distal to the beaded surface. In the case of a completely bonded cement-bead interface (BC=1, Figure 6.13), there is little posterior load transfer proximally and almost all

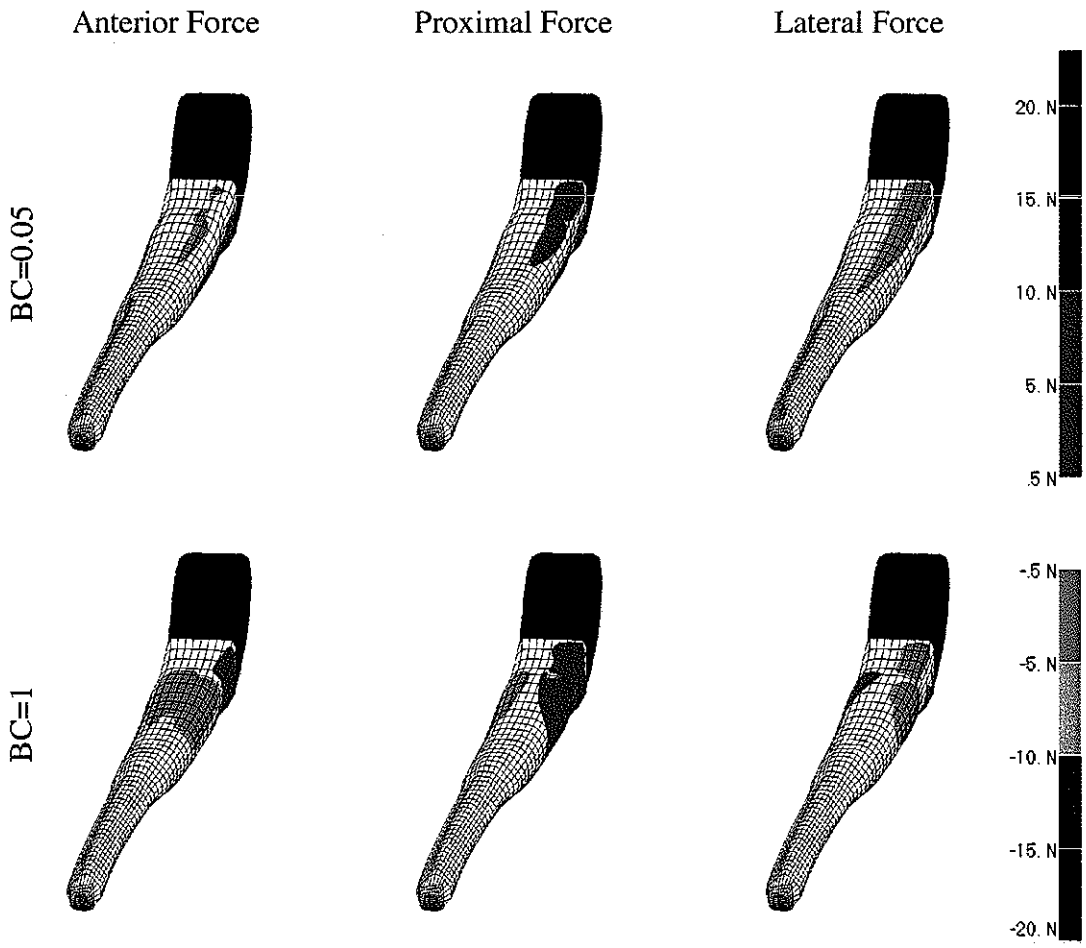

Figure 6.11: Anterior, proximal, and lateral forces (N) on the stem of the ulnar component for frictional (BC=0.5), and bonded (BC=1) interface conditions, the humerus in position 10 and α=0.5 (forces on proximal region (blue) not shown).

load is transferred to the bone around the proximal and beaded sections of the implant.

6.3.3 Cement Stresses

Maximum principal stresses in the cement mantle were only sensitive to interface boundary condition (Table 6.5). No other parameter caused a substantial change in the cement stresses observed.

Table 6.5: Coefficients of the Linear Regression of Cement Stresses

$\sigma_{DIST\_CEMENT} = \gamma_1 * AP + \gamma_2 * PD + \gamma_3 + VV + \gamma_4 * IE + \gamma_5 * \alpha + \gamma_6 * BC + \gamma_7$.							
	γ_1	γ_2	γ_3	γ_4	γ_5	γ_6	γ_7
Distal Region	-0.00	-0.00	0.00	0.00	-0.10	-0.49	0.75
Middle Region	-0.00	-0.00	0.00	0.02	-0.05	0.67	0.79
Proximal Region	-0.00	-0.00	0.00	0.02	-0.10	-2.35	3.33

The observed changes in the magnitudes of the maximum principal cement stresses were found to be significant for the proximal cement ($p<0.001$), middle cement ($p<0.001$), and distal cement ($p<0.001$) regions (Figure 6.14).

6.4 Discussion

The objective of this study was to determine the structural response of the ulnar-bone implant system under common activities of daily living. Similar to our humeral analyses, the effects of humeral implant position and type of fixation between the beaded implant and the cement mantle characteristics had on load transfer from the implant to the bone and on the strains arising in the bone and stresses arising in the cement mantle were investigated. Again, to account for variations in bone material

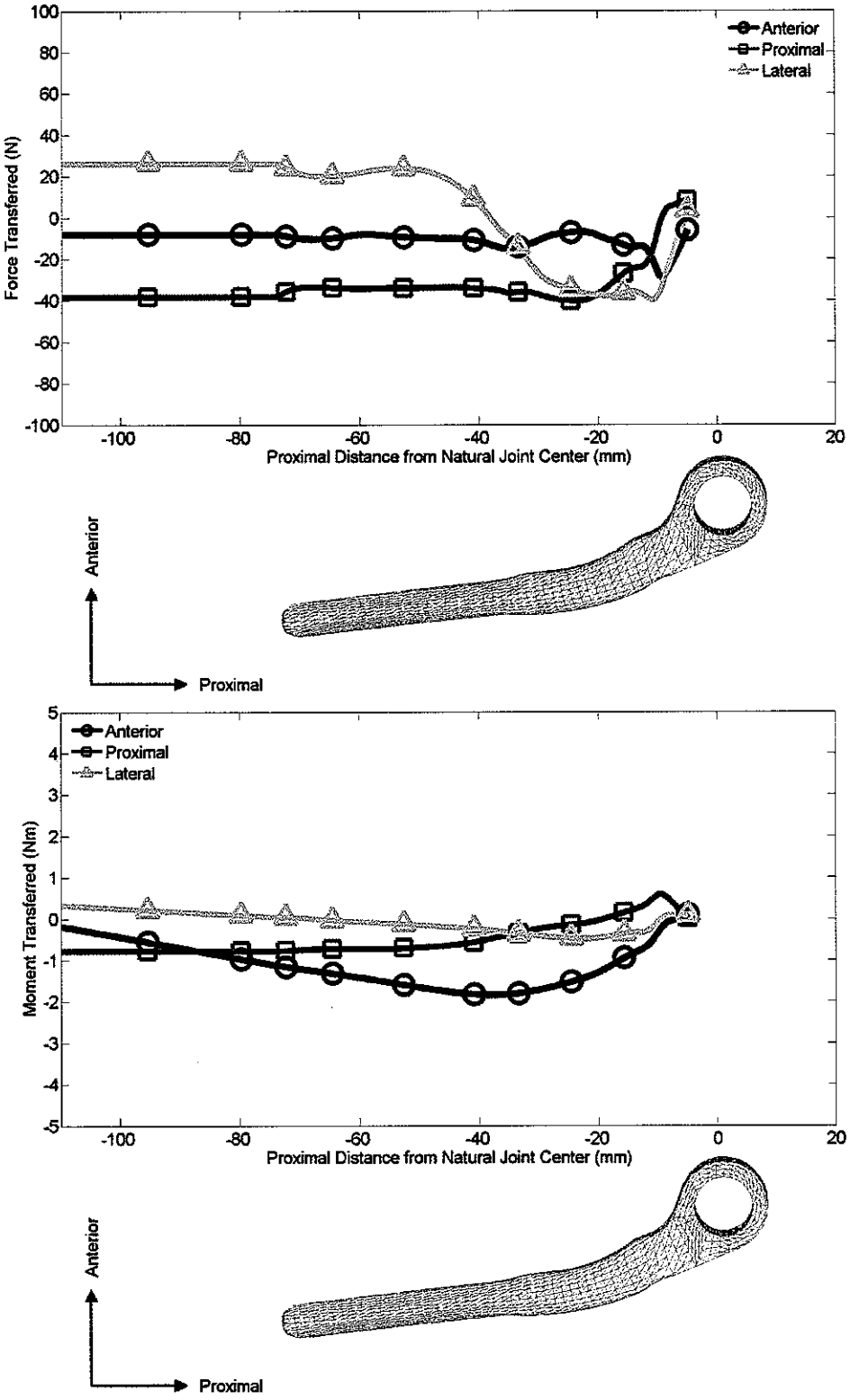

Figure 6.12: Forces and moments transferred into the ulna for the frictional (BC=0.5) interface conditions with the humerus in position 10 with α=0.5.

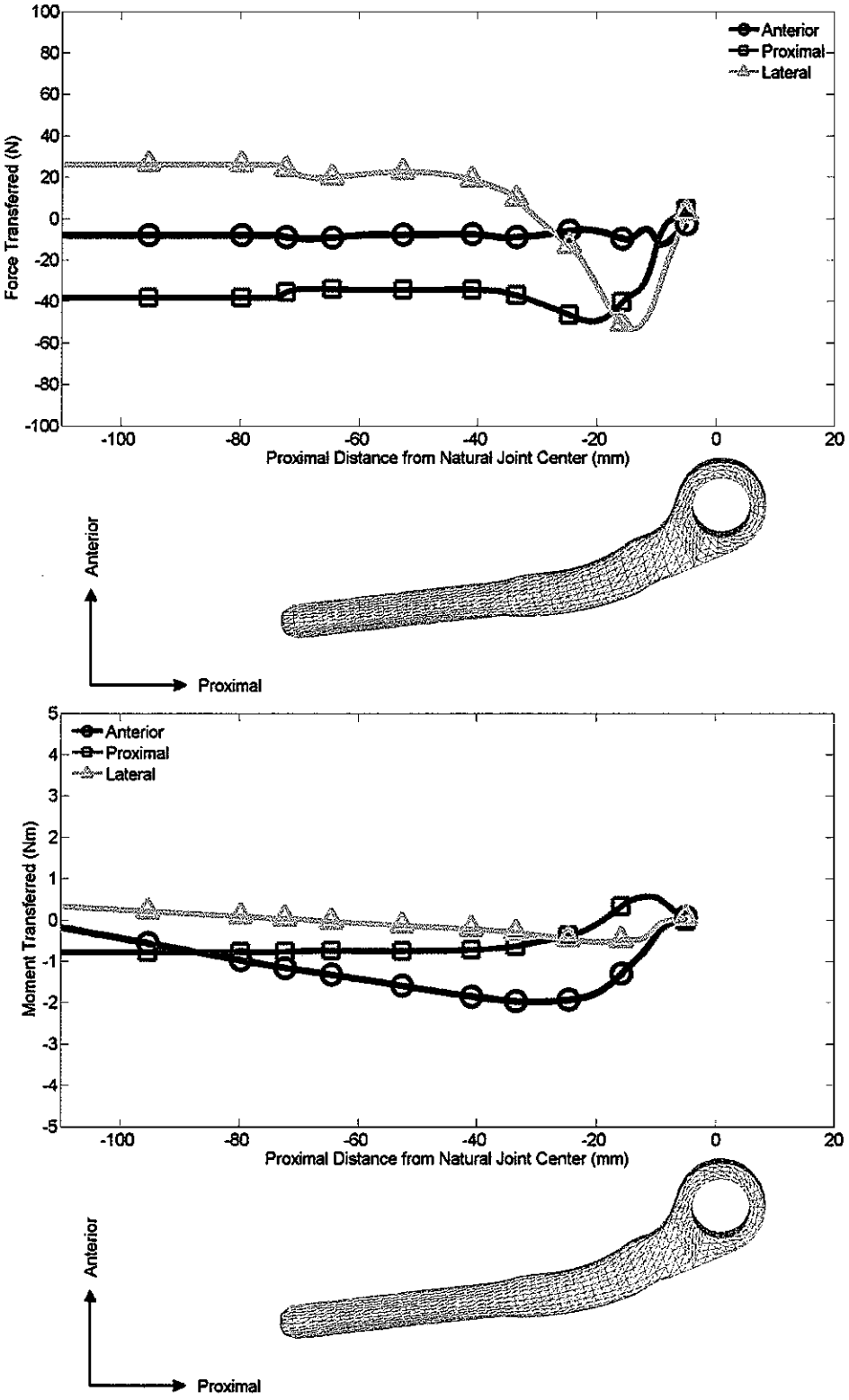

Figure 6.13: Forces and moments transferred into the ulna for the bonded (BC=1) interface conditions with the humerus in position 10 with α=0.5.

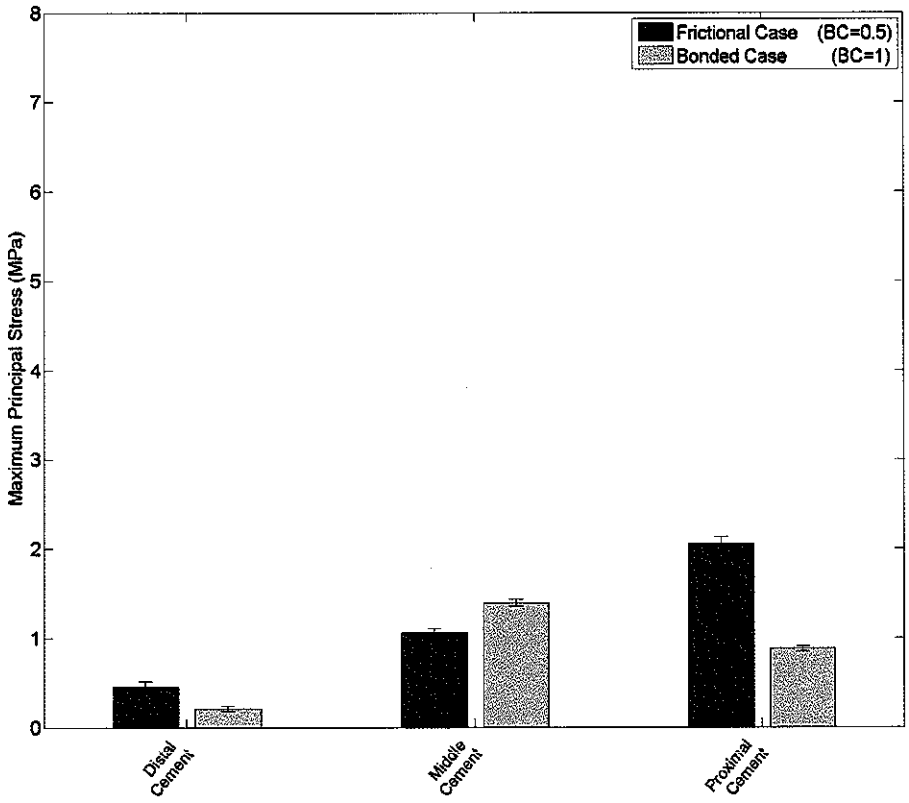

Figure 6.14: Volume-weighted maximum principal cement stress in 5% most highly stressed volume in three regions of the ulnar cement mantle

properties that occur naturally within a population, implant positions and fixation were evaluated using three different density-to-modulus relationships for bone.

As with the humeral component, ulnar components in which the coating has achieved complete interlock with the surrounding cement mantle transmit load nearer to the articulation of the elbow. Unlike the humeral component of the Coonrad-Morrey, a single pathway of load transfer is present in the ulnar bone-implant system, thereby making the structural response of the system more predictable.

While the stresses in the cement layer of the ulnar system approach neither the fatigue limit for PMMA [41] nor the magnitudes of the maximum principal stresses seen in

the cement mantle surrounding the humeral component of the Coonrad-Morrey, changes in the implant-cement interface do cause substantial changes in the cement mantle stresses. Changing from a bonded to a frictional interface increases the magnitude of the maximum principal stress over 100% in both the proximal and distal cement layer, while decreasing stress in the middle section of the cement mantle by less than 25%. Although at these loading levels even the increased stresses may not be sufficient to cause cement failure, as with the humeral component, it is possible that a noncompliant patient who is not following the recommended activity restrictions following a total elbow arthroplasty would exceed the stress magnitudes observed here.

As was the case with the humerus, few experimental studies exist to which our ulnar studies may be compared. Only a single three-dimensional finite element analysis [23] of the ulnar aspect of the Coonrad or Coonrad-Morrey implants has been published. Unfortunately, the differences between the loading conditions, material properties, and interface conditions used in that study and those used in our current study are too great to make any meaningful comparisons.

To validate this study, it then becomes necessary to evaluate the clinical experience surrounding the ulnar component of the Coonrad-Morrey and determine whether the behavior predicted in our study corresponds to that which has been observed *in vivo*. As stated previously, with the increased performance of the humeral component of the implant, radiolucencies around the ulnar component are becoming a more common reason for implant revision. Recent studies have suggested a link between the type of coating attached to the proximal aspect of the ulnar component, which corresponds to the surfaces in our model that were varied between the frictional and bonded cases, and the presence of radiolucencies and the development of osteolytic lesions [26, 33,

51]. As the design of the Coonrad-Morrey has evolved, the coating on this surface has changed from sintered titanium beads, to a polymethylmethacrylate (PMMA) precoating, to a plasma-sprayed titanium coating [33]. The PMMA precoating, specifically, seems more likely to develop the observed radiolucencies. Hildebrand et al. [26] noted two areas where these radiolucencies appeared. The first was near the distal stem tip and the second was at the proximal ulna. These are the two locations in our analyses where the stresses in the cement mantle can be seen to significantly increase as the strength of the bonding between the implant and the cement layer is decreased. Illustrating that the PMMA precoating is a weaker interface than the other applied coatings, Cheung et al. [14] have discussed an additional failure mechanism for ulnar components with PMMA precoating in which impingement of the humeral flange on the anterior coronoid process of the ulna during deep elbow flexion can lead to pistoning of the ulnar component with the canal. This failure mechanism does not occur with the beaded or plasma-sprayed surface coatings, indicating the PMMA precoat is able to transmit less force before interface failure. Thus the interfaces that are shown to be weaker *in vivo* cause radiolucencies around the distal and proximal portions of the implant. These are the same locations at which higher cement stresses are predicted when we change the implant-cement interface in our models from bonded to unbonded (no tension, friction).

In addition, when taken together, the humeral and the ulnar finite element analyses suggest why failure may be occurring more often at the ulnar component than the humeral component of the Coonrad-Morrey. Assuming adequate distal contact of the implant in the humeral system, when the degree of bonding between the implant and the cement is decreased in the humerus, cement stresses increase slightly around the midstem of the implant, but remain unchanged in the proximal and distal cement

regions. In the ulnar case, however, when bonding is decreased between the implant and cement, cement stresses increase considerably in both the proximal and the distal cement regions. Thus, the cement stresses in the ulnar bone-implant system are more likely to be negatively affected than those in the humeral bone-implant system when implant fixation is decreased, possibly placing the ulnar system at greater risk of failure.

This study is subject to the same limitations as those accompanying our humeral finite element analyses. As was discussed in Chapter 5, the stress and strain magnitudes, in addition to those of other structural responses, are dependent upon mesh discretizations, material approximations, and other modeling assumptions. Thus while finite element analyses are needed to understand the internal response of the system, they are most useful and applicable when evaluating changes in the structural response to changes in input parameters rather than predicting values that might occur *in vivo*.

In addition, the selection of the shortest implant length for the ulnar component may have been a more extreme case biased towards load transfer away from the joint as shorter stems will behave more rigidly than longer ones. However, the large increases in distal load transfer are unlikely to be due only to this fact. In addition, the humeral analyses were also performed using the shortest implants, making the comparisons between the too cases valid explorations of worst-case scenarios.

In this study, humeral position had almost no effect on the structural behavior of the ulna-implant system. The changes in applied loading over the range of humeral component locations examined were small and any effect of these changes was dwarfed by both the relationship between density and moduli, which in turn was

dwarfed by the implant-cement interface condition. Thus, the position of the humeral component may be chosen without considering its effect on the structural response of the ulna. Ulnar component position, however, may still have a strong effect on the structural response of the system and should be investigated in the future.

Chapter 7

Summary and Conclusions

The overarching goal of this research was to increase our understanding of how the kinematics of the upper extremity influence the biomechanical environments around the shoulder and elbow joints. We also wanted to determine how different surgical treatments may change the forces and loads across the joint as a person moves through various motions. We addressed our questions using different strategies for each joint. In the shoulder, we developed an *in vitro* physical simulator to determine the relationship between shoulder kinematics and loading for different movements of the arm. The simulator was tested using a simplified representation of the shoulder and was able to move through the motion we prescribed using an optimally derived set of forces. The purpose of the simulator is to examine the effects of different motions on the joint loading of both native and surgically treated shoulders.

For the elbow, we were more concerned with the outcome of a specific surgical procedure, total elbow arthroplasty. While there are certainly other surgical treatments

of the elbow on which we could have focused, the wide variation in survivorship for total elbow arthroplasty indicated that it was a prime candidate for analysis. In order to improve clinical outcomes for arthroplasty patients, it was first necessary to understand why current treatments fail as they do. Observing that aseptic loosening of both components of the elbow is a common complication for contemporary total elbow replacements, and that this loosening is often associated with wear of the articular bushings of the implant, we first investigated how implant positioning during surgery would affect the contact forces at the articular junction of the humeral and ulnar implant components. Using a computational model of the upper extremity along with the kinematics of two activities of daily living taken from the literature, we were able to determine that most variations in surgical humeral component positioning did not have a substantial effect on the forces across the articulation of the total elbow replacement. However, internal-external rotations of the component did significantly increase the contact force at the joint and also allowed the components to effectively rotate even further internally, potentially causing even greater increases in contact force.

Our analysis of the contact forces across the joint highlighted the absence in the literature of kinematic data taken from total elbow patients. The kinematic data that were used in that study were gathered from normal, unimpaired subjects and no data existed to suggest how varied the kinematics would be if they were collected from the recipients of total elbow replacements. To answer this question, we recorded motion analysis data from both normal subjects and total elbow replacement patients. The kinematic data, while indicating a large degree of variability in the motions of the normal subjects, also indicated that the range of kinematic data displayed by the normal subjects rarely explained the kinematics exhibited by the total elbow patients.

Joint reaction forces calculated using the kinematics indicated similar characteristics; normal subject joint loading rarely explained the joint loading in total elbow patients. However, our analyses also indicated that the differences between the loading of the normal and total elbow patients were small, making the normal data a useful approximation to the total elbow loads in most cases and demonstrating that the contact forces calculated when evaluating humeral component position using normal subject data would be similar if the kinematics of total elbow patients were used.

In evaluating total elbow replacement loosening, the contact forces across the joint were not the only measure about which we were concerned. While polyethylene wear may contribute to the aseptic loosening of implant components, structural failure of the surrounding trabecular bone and cement mantle will also lead to implant loosening. To address these concerns, finite element analyses of the bone-implant systems for both the humeral and the ulnar components of a total elbow replacement were performed. The sensitivity of the maximum principal stress in the cement and the minimum principal strain in the bone to variations in humeral component position, in the fixation between the implant and the cement, and in the stiffness of the surrounding bone was evaluated for each bone-implant system.

When the strength of bonding between the implant and cement in the humeral system was reduced, loads were transferred into the bone more proximally (away from the joint). However, cement stresses did not increase in the proximal mantle or the distal mantle for this condition. When the extent of contact between the implant and the surrounding bone (including graft) was lessened, with no contact allowed distally or under the flange, all load was transmitted through the stem. In this case, cement stresses were unaffected proximally but increased significantly distally where the

implant entered the bone. In the ulnar bone-implant system, when bonding between the implant and cement was reduced, loads to the bone were transferred more distally (away from the joint). Unlike the humeral case, however, cement stresses increased in both the proximal and distal mantles when bonding between the implant and the cement was relaxed.

Taken together, the results of the analyses of the total elbow replacements offer some interesting insights into the behavior and failure of these implants. We see that there are two primary factors that could contribute to component loosening and lead ultimately to revision. The first of these factors is humeral component position. While humeral position has no effect on the structural responses of the implanted humerus or ulna, internally rotated humeral components do increase contact forces and may further increase wear and lead to particulate generation. The second factor is the fixation of the implant with respect to the cement and the bone. Our analyses demonstrate that humeral bone-implant systems that lack distal contact around the implant exhibit increased distal cement stresses. This type of situation would most likely be seen in patients with poor distal bone stock due to joint degeneration or missing condyles due to trauma. Interestingly, the implant survivorship for patients with rheumatoid arthritis, who would be the most likely group to show a consistent decrease in bone properties near the joint, has been suggested to be less than for other patient cohorts and thus may substantiate our findings. Also, as the bond between the implant and cement is weakened, cement stresses are only negatively affected in the ulnar bone-implant system and make it more prone to failure than the humeral component. Clinically, increased failure of the ulnar side of the prosthesis has also been observed.

These analyses of contemporary total elbow replacements have enabled us to make predictions as to what surgical factors will speed the failure of a current implant. Namely, internally rotated implants, with incomplete bonding at the implant-cement interface, and a lack of contact between the chevron of the humeral component and the distal humerus would be thought to perform particularly poorly. Knowledge of these factors implicated in total elbow failure will aid in both improving the performance of the current generation of implants as well as in designing future implants for the elbow.

The success of our finite element studies in explaining some of the reasons for the failures observed clinically in the elbow demonstrates the utility of the finite element technique. As such, in the future the technique could be coupled with any studies performed using the *in vitro* shoulder simulator. A computational finite element model run in parallel with the physical simulator would provide information not only about the loading at the joint and changes in the articular surface of the joint (such as articular cartilage damage or implant wear) but also about the structural response of the bone or bone-implant system under those applied loads for the motion being studied.

Future finite element analyses could also be performed to extend the studies of the elbow presented here. Variations in humeral position have been examined, but it is possible for the position of the ulnar component to vary as well, and the effects of ulnar variation on structural responses are unknown. In addition, the loading conditions for these studies were chosen as they are indicative of the types of loads to which the total elbow replacement of a compliant patient would be exposed. Patients, however, may certainly be noncompliant, whether intentionally or not, and the investigation of the structural response under higher, more extreme loading could also

offer insight into some of implant failures seen clinically.

Overall, we investigated methods of ascertaining the response at the shoulder and elbow joints to the biomechanical environments imposed by the varied activities of the upper extremity. We developed a novel *in vitro* simulator of shoulder motion to determine forces across the shoulder and enable the testing of new surgical techniques or devices. We also investigated the wear and structural response of current total elbow replacements subjected to these motions and determined factors that may contribute to the failure of these implants.

BIBLIOGRAPHY

[1] Aldridge JM, 3rd, Lightdale NR, Mallon WJ, et al. 2006. Total elbow arthroplasty with the Coonrad/Coonrad-Morrey prosthesis. A 10- to 31-year survival analysis. J Bone Joint Surg Br 88:509-14.

[2] Aldridge JM, 3rd, Lightdale NR, Mallon WJ, et al. 2006. Total elbow arthroplasty with the Coonrad/Coonrad-Morrey prosthesis: a 10- to 31-year survival analysis. J Bone Joint Surg Br 88:509-14.

[3] Alpert SW, Pink MM, Jobe FW, et al. 2000. Electromyographic analysis of deltoid and rotator cuff function under varying loads and speeds. J Shoulder Elbow Surg 9:47-58.

[4] Amis AA, Dowson D, Wright V. 1980. Elbow joint force predictions for some strenuous isometric actions. J Biomech 13:765-75.

[5] An KN, Hui FC, Morrey BF, et al. 1981. Muscles across the elbow joint: a biomechanical analysis. J Biomech 14:659-69.

[6] An KN, Kwak BM, Chao EY, et al. 1984. Determination of muscle and joint forces: a new technique to solve the indeterminate problem. J Biomech Eng 106:364-7.

[7] Anglin C. 1993. M.A.Sc. Thesis. Vancouver, Canada: The University of British Columbia.

[8] Anglin C, Wyss UP. 2000. Arm motion and load analysis of sit-to-stand, stand-to-sit, cane walking and lifting. Clin Biomech (Bristol, Avon) 15:441-8.

[9] Boileau P, Watkinson DJ, Hatzidakis AM, et al. 2005. Grammont reverse prosthesis: design, rationale, and biomechanics. J Shoulder Elbow Surg 14:147S-161S.

[10] Buchanan TS, Shreeve DA. 1996. An evaluation of optimization techniques for the prediction of muscle activation patterns during isometric tasks. J Biomech Eng 118:565-74.

[11] Buck FM, Jost B, Hodler J. 2008. Shoulder arthroplasty. Eur Radiol 18:2937-48.

[12] Chadwick EK, Nicol AC. 2000. Elbow and wrist joint contact forces during occupational pick and place activities. J Biomech 33:591-600.

[13] Challis JH. 1997. Producing physiologically realistic individual muscle force estimations by imposing constraints when using optimization techniques. Med Eng Phys 19:253-61.

[14] Cheung EV, O'Driscoll SW. 2007. Total elbow prosthesis loosening caused by ulnar component pistoning. J Bone Joint Surg Am 89:1269-74.

[15] Crowninshield RD, Brand RA. 1981. A physiologically based criterion of muscle force prediction in locomotion. J Biomech 14:793-801.

[16] de Groot JH, Brand R. 2001. A three-dimensional regression model of the shoulder rhythm. Clin Biomech (Bristol, Avon) 16:735-43.

[17] Debski RE, McMahon PJ, Thompson WO, et al. 1995. A new dynamic testing apparatus to study glenohumeral joint motion. J Biomech 28:869-74.

[18] Delp SL, Grierson AE, Buchanan TS. 1996. Maximum isometric moments generated by the wrist muscles in flexion-extension and radial-ulnar deviation. J Biomech 29:1371-5.

[19] Diederichs G, Korner J, Goldhahn J, et al. 2006. Assessment of bone quality in the proximal humerus by measurement of the contralateral site: a cadaveric analyze. Arch Orthop Trauma Surg 126:93-100.

[20] Figgie HE, 3rd, Inglis AE, Mow C. 1986. A critical analysis of alignment factors affecting functional outcome in total elbow arthroplasty. J Arthroplasty 1:169-73.

[21] Gill DR, Morrey BF. 1998. The Coonrad-Morrey total elbow arthroplasty in patients who have rheumatoid arthritis. A ten to fifteen-year follow-up study. J Bone Joint Surg Am 80:1327-35.

[22] Goel V, Lee I, Blair W. 1989. Effect of the Coonrad elbow prosthesis on stresses in the humerus. Clinical Biomechanics 4:11-16.

[23] Goel VK, Lee IK, Blair WF. 1989. Stress distribution in the ulna following a hinged elbow arthroplasty. A finite element analysis. J Arthroplasty 4:163-71.

[24] Goldberg SH, Urban RM, Jacobs JJ, et al. 2008. Modes of wear after semiconstrained total elbow arthroplasty. J Bone Joint Surg Am 90:609-19.

[25] Herren DB, Ploeg H, Hertig D, et al. 2004. Modeling and finite element analysis of a new revision implant for the elbow. Clin Orthop Relat Res:292-7.

[26] Hildebrand KA, Patterson SD, Regan WD, et al. 2000. Functional outcome of semiconstrained total elbow arthroplasty. J Bone Joint Surg Am 82-A:1379-86.

[27] Holzbaur KR, Murray WM, Delp SL. 2005. A model of the upper extremity for simulating musculoskeletal surgery and analyzing neuromuscular control. Ann Biomed Eng 33:829-40.

[28] Hughes RE, An KN. 1996. Force analysis of rotator cuff muscles. Clin Orthop Relat Res:75-83.

[29] Inman VT, Saunders JB, Abbot LC. 1944. Observations on the function of the shoulder joint. J Bone Joint Surg Am 26:1-30.

[30] Itoi E, Newman SR, Kuechle DK, et al. 1994. Dynamic anterior stabilisers of the shoulder with the arm in abduction. J Bone Joint Surg Br 76:834-6.

[31] Jacobson MD, Raab R, Fazeli BM, et al. 1992. Architectural design of the human intrinsic hand muscles. J Hand Surg [Am] 17:804-9.

[32] Jiang Y, Zhao J, Augat P, et al. 1998. Trabecular bone mineral and calculated structure of human bone specimens scanned by peripheral quantitative computed tomography: relation to biomechanical properties. J Bone Miner Res 13:1783-90.

[33] Kamineni S, Morrey BF. 2004. Distal humeral fractures treated with noncustom total elbow replacement. J Bone Joint Surg Am 86-A:940-7.

[34] Kaneko TS, Pejcic MR, Tehranzadeh J, et al. 2003. Relationships between material properties and CT scan data of cortical bone with and without metastatic lesions. Med Eng Phys 25:445-54.

[35] Karduna AR, Williams GR, Williams JL, et al. 1996. Kinematics of the glenohumeral joint: influences of muscle forces, ligamentous constraints, and articular geometry. J Orthop Res 14:986-93.

[36] Karlsson D, Peterson B. 1992. Towards a model for force predictions in the human shoulder. J Biomech 25:189-99.

[37] Kedgley AE, Mackenzie GA, Ferreira LM, et al. 2007. The effect of muscle loading on the kinematics of in vitro glenohumeral abduction. J Biomech 40:2953-60.

[38] Kelkar R, Wang VM, Flatow EL, et al. 2001. Glenohumeral mechanics: a study of articular geometry, contact, and kinematics. J Shoulder Elbow Surg 10:73-84.

[39] Keyak JH, Lee IY, Skinner HB. 1994. Correlations between orthogonal mechanical properties and density of trabecular bone: use of different densitometric measures. J Biomed Mater Res 28:1329-36.

[40] Kraay MJ, Figgie MP, Inglis AE, et al. 1994. Primary semiconstrained total elbow arthroplasty. Survival analysis of 113 consecutive cases. J Bone Joint Surg Br 76:636-40.

[41] Krause W, Mathis RS, Grimes LW. 1988. Fatigue properties of acrylic bone cement: S-N, P-N, and P-S-N data. J Biomed Mater Res 22:221-44.

[42] Kuechle DK, Newman SR, Itoi E, et al. 1997. Shoulder muscle moment arms during horizontal flexion and elevation. J Shoulder Elbow Surg 6:429-39.

[43] Langenderfer J, Jerabek SA, Thangamani VB, et al. 2004. Musculoskeletal parameters of muscles crossing the shoulder and elbow and the effect of sarcomere length sample size on estimation of optimal muscle length. Clin Biomech (Bristol, Avon) 19:664-70.

[44] Langenderfer JE, Patthanacharoenphon C, Carpenter JE, et al. 2006. Variation in external rotation moment arms among subregions of supraspinatus, infraspinatus, and teres minor muscles. J Orthop Res 24:1737-44.

[45] Laursen B, Jensen BR, Nemeth G, et al. 1998. A model predicting individual shoulder muscle forces based on relationship between electromyographic and 3D external forces in static position. J Biomech 31:731-9.

[46] Lenhoff MW, Santner TJ, Otis JC, et al. 1999. Bootstrap prediction and confidence bands: a superior statistical method for analysis of gait data. Gait Posture 9:10-7.

[47] Lieber RL, Fazeli BM, Botte MJ. 1990. Architecture of selected wrist flexor and extensor muscles. J Hand Surg [Am] 15:244-50.

[48] Lieber RL, Jacobson MD, Fazeli BM, et al. 1992. Architecture of selected muscles of the arm and forearm: anatomy and implications for tendon transfer. J Hand Surg [Am] 17:787-98.

[49] Linscheid RL, Stanley D, Trail IA, et al. 2000. Resurfacing elbow replacement arthroplasty. In: Morrey BF, editor. The elbow and its disorders, 3rd ed. Philadelphia: Saunders; p 602-616.

[50] Little CP, Carr AJ, Graham AJ. 2005. Total elbow arthroplasty. J Bone Joint Surg Br 87:437-44.

[51] Little CP, Graham AJ, Karatzas G, et al. 2005. Outcomes of total elbow arthroplasty for rheumatoid arthritis: comparative study of three implants. J Bone Joint Surg Am 87:2439-48.

[52] Mann KA, Bartel DL, Wright TM, et al. 1995. Coulomb frictional interfaces in modeling cemented total hip replacements: a more realistic model. J Biomech 28:1067-78.

[53] Mansat P, Cofield RH, Kersten TE, et al. 1997. Complications of rotator cuff repair. 28:205.

[54] McPherson EJ, Friedman RJ, An YH, et al. 1997. Anthropometric study of normal glenohumeral relationships. J Shoulder Elbow Surg 6:105-12.

[55] Morgan EF, Bayraktar HH, Keaveny TM. 2003. Trabecular bone modulus-density relationships depend on anatomic site. J Biomech 36:897-904.

[56] Morgan EF, Keaveny TM. 2001. Dependence of yield strain of human trabecular bone on anatomic site. J Biomech 34:569-77.

[57] Morrey BF. 2000. Complications of elbow replacement surgery. In: Morrey BF, editor. The elbow and its disorders, 3rd ed. Philadelphia: Saunders; p 671.

[58] Morrey BF. 2000. The elbow and its disorders, pp 671

[59] Murray IA, Johnson GR. 2004. A study of the external forces and moments at the shoulder and elbow while performing every day tasks. Clin Biomech (Bristol, Avon) 19:586-94.

[60] Murray WM, Buchanan TS, Delp SL. 2000. The isometric functional capacity of muscles that cross the elbow. J Biomech 33:943-52.

[61] Neer CS, 2nd, Craig EV, Fukuda H. 1983. Cuff-tear arthropathy. J Bone Joint Surg Am 65:1232-44.

[62] Otis JC, Jiang CC, Wickiewicz TL, et al. 1994. Changes in the moment arms of the rotator cuff and deltoid muscles with abduction and rotation. J Bone Joint Surg Am 76:667-76.

[63] Pearl ML, Harris SL, Lippitt SB, et al. 1992. A system for describing positions of the humerus relative to the thorax and its use in the presentation of several functionally important arm positions. 1:113.

[64] Poppen NK, Walker PS. 1978. Forces at the glenohumeral joint in abduction. Clin Orthop Relat Res:165-70.

[65] Quenneville CE, Austman RL, King GJ, et al. 2008. Role of an anterior flange on cortical strains through the distal humerus after total elbow arthroplasty with a latitude implant. J Hand Surg [Am] 33:927-31.

[66] Rab G, Petuskey K, Bagley A. 2002. A method for determination of upper extremity kinematics. Gait Posture 15:113-9.

[67] Radford M, Carr A. 2002. (i) Total elbow replacement. Current Orthopaedics 16:325-330.

[68] Romilly DP, Anglin C, Gosine RG, et al. 1994. A functional task analysis and motion simulation for the development of a powered upper-limb orthosis. IEEE Transactions on Rehabilitation Engineering 2:119.

[69] Schuind F, O'Driscoll S, Korinek S, et al. 1995. Loose-hinge total elbow arthroplasty. An experimental study of the effects of implant alignment on three-dimensional elbow kinematics. J Arthroplasty 10:670-8.

[70] Scibek JS, Mell AG, Downie BK, et al. 2008. Shoulder kinematics in patients with full-thickness rotator cuff tears after a subacromial injection. J Shoulder Elbow Surg 17:172-81.

[71] Soslowsky LJ, Flatow EL, Bigliani LU, et al. 1992. Quantitation of in situ contact areas at the glenohumeral joint: a biomechanical study. J Orthop Res 10:524-34.

[72] van der Helm FC. 1994. Analysis of the kinematic and dynamic behavior of the shoulder mechanism. J Biomech 27:527-50.

[73] van der Helm FC. 1994. A finite element musculoskeletal model of the shoulder mechanism. J Biomech 27:551-69.

[74] van der Helm FC, Veeger HE, Pronk GM, et al. 1992. Geometry parameters for musculoskeletal modelling of the shoulder system. J Biomech 25:129-44.

[75] Veeger HE, Van der Helm FC, Van der Woude LH, et al. 1991. Inertia and muscle contraction parameters for musculoskeletal modelling of the shoulder mechanism. J Biomech 24:615-29.

[76] Veeger HE, Yu B, An KN, et al. 1997. Parameters for modeling the upper extremity. J Biomech 30:647-52.

[77] Veeger HEJ, van der Helm FCT, Rozendal RH. 1993. Orientation of the scapula in a simulated wheelchair push. 8:81.

[78] Williams GR, Jr., Rockwood CA, Jr., Bigliani LU, et al. 2004. Rotator cuff tears: why do we repair them? J Bone Joint Surg Am 86-A:2764-76.

[79] Wolfe SW, Figgie MP, Inglis AE, et al. 1990. Management of infection about total elbow prostheses. J Bone Joint Surg Am 72:198-212.

[80] Wright TW, Hastings H. 2005. Total elbow arthroplasty failure due to overuse, C-ring failure, and/or bushing wear. J Shoulder Elbow Surg 14:65-72.

[81] Wu G, van der Helm FC, Veeger HE, et al. 2005. ISB recommendation on definitions of joint coordinate systems of various joints for the reporting of human joint motion--Part II: shoulder, elbow, wrist and hand. J Biomech 38:981-992.